MICROSTRUCTURAL INFLUENCE ON DEFORMATION, DEGRADATION AND FRACTURE OF DUCTILE MATERIALS

A Dissertation

by

XINZHU ZHENG

Submitted to the Graduate and Professional School of
Texas A&M University
in partial fulfillment of the requirements for the degree of

DOCTOR OF PHILOSOPHY

Chair of Committee,	Ankit Srivastava
Committee Members,	Homero Castaneda-Lopez
	Kelvin Xie
	Kan Wu
Head of Department,	Ibrahim Karaman

August 2021

Major Subject: Materials Science and Engineering

ABSTRACT

The overarching goal of this dissertation is to quantify the microstructural influence on deformation, degradation, and fracture of some of the most technologically sought after advanced structural materials. In the first part of this work, the mechanical response of a variety of advanced high strength steels with complex microstructure is characterized by *in-situ* mechanical tests. The experimental results show that even though the uniaxial tensile response of several of these steels is the same, their fracture response differs significantly. This contradicts classical analysis that predicts the same fracture response for materials with the same uniaxial tensile response. The high-resolution *in-situ* tests coupled with microscale digital image correlation (μDIC) and microstructure-based finite element analysis are then used to elucidate how the interlacing of imposed heterogeneous deformation field and the material microstructure affects the fracture response of these materials. The implications of these findings extend to both manufacturing issues and issues of materials development (or selection) based upon a specific need. The second part of this work focuses on understanding the influence of deformation-induced twinning on fracture response of single crystal specimens of an austenitic manganese steel. The crystallographic orientations of single crystal specimens are chosen to selectively activate crystallographic slip or twinning. The high-resolution *in-situ* tests coupled with μDIC and EBSD analysis are then used to elucidate how the interlacing of imposed heterogeneous deformation field and the evolving material microstructure affects the fracture response of the material. Finally, the synergistic effects of mechanical loading and corrosive environment on fracture response of an aluminum

alloy are investigated. In general, environmental assisted fracture of a material is analyzed by simply characterizing mechanical response in a corrosive environment, while the emerging electrochemical characteristics are ignored. To overcome this, a 3-electrode setup for electrochemical impedance spectroscopy is built to characterize the electrochemical response of the material while being subjected to mechanical loading and corrosive environment. The results of these experiments coupled with microscopic characterization provide an unprecedented view of the synergistic effects of mechanical loading and corrosive environment on the environmental assisted fracture process.

ACKNOWLEDGEMENTS

Although, a few words of thanks would not express my gratitude to people who have supported me throughout the course of my PhD, I would like to take a moment to at least acknowledge their support.

I would like to thank my advisor, Dr. Ankit Srivastava, for his support throughout my PhD. His professional guidance provided insight in formulating the research topics and methodology and inspired me to handle all challenges and complications during my research.

I would also like to thank my PhD committee members, Dr. Homero Castaneda-Lopez, Dr. Kelvin Xie and Dr. Kan Wu, for their time, invaluable feedback, and advice throughout this work.

I take this opportunity to acknowledge the mentorship that I received from Dr. Shmuel Osovski of Technion-Israel Institute of Technology, Dr. Huajian Gao of Brown University, Dr. José A. Rodríguez-Martínez of University Carlos III de Madrid, Dr. Hassan Ghassemi-Armaki of ArcelorMittal Global R&D, and Dr. Homero Castaneda-Lopez, Dr. Karl T. Hartwig and Dr. Ibrahim Karaman of Texas A&M University. Thank you for helping me with the research projects and for providing constructive criticism to the manuscripts.

A thank you to my groupmates, Abhilash Molkeri, Edwin Chiu, Hemant Rathod, Lara Draelos, Laura Moody, Umair Bin Asim, Yu Liu, Zahra Ghasemi and Zhiqiang Zhan, it has been a wonderful experience interacting with you. I would like to extend a special thanks to Yu Liu, for the days we spent together in the office next to each other.

A thank you to my friend, Tianyang Zhou, for being a perfect neighbor and infecting me with positive attitude towards life. Also, a thank you to my friend, Sisi Xiang, for the relaxing hot pot parties.

A special thanks to all the Materials Science and Engineering department faculty and staff for making me feel welcome.

Finally, many thanks to my parents and my husband, Xiyao, for their support and faith in me. To Xiyao, thank you for traveling across the Pacific Ocean to accompany me on my PhD journey. Your patience and love is indispensable to me.

CONTRIBUTORS AND FUNDING SOURCES

Contributors

This work was supervised by a dissertation committee consisting of Professors Ankit Srivastava, Homero Castaneda-Lopez and Kelvin Xie of the Department of Materials Science and Engineering and Professor Kan Wu of the Harold Vance Department of Petroleum Engineering.

All other work conducted for the dissertation was completed by the student independently.

Funding Sources

Financial support provided by the American Chemical Society – Petroleum Research Fund # 57643-DNI10; HEEP Graduate Fellowship from the Hagler Institute of Advanced Study (HIAS); and U.S. National Science Foundation grants CMMI – 1663130 and DMR – 1611380 are gratefully acknowledged. The advanced high strength steels used in this research were kindly provided by the ArcelorMittal Global R&D, East Chicago, IN, USA. The finite element calculations reported on were carried out using high performance research computing resources provided by the Texas A&M University.

TABLE OF CONTENTS

LIST OF FIGURES

Page

LIST OF TABLES

Page

1. INTRODUCTION

1.1. Motivation

Materials mechanics has always been a source of wonderfully challenging problems. It has stimulated the development of new mechanics theories, experimental methods and simulation techniques. These provide physical insights on the linkage between the material properties, applied boundary and loading conditions, and the mechanical performance. The mechanical performance especially final fracture of a material is also dictated by the spatial and temporal evolutions of defects and damages in the material microstructure. Fracture involves creation of new free surfaces through nucleation, growth and/or coalescence of microscopic cracks. This phenomenon is affected by the spatiotemporal interactions of geometry of deformation and the material microstructure. For example, the deformation field induced by the geometry or boundary conditions can produce substantial microstructural modifications resulting in often unknown and counterintuitive subsequent fractures processes. Schematically, as shown in Fig. 1.1(a), a standard dog-bone specimen under uniaxial tension has a homogeneous deformation field in the gauge section such that its fracture response is largely driven by the microstructure; however, the plastic deformation zone ahead of a crack tip is inherently heterogeneous. The heterogeneity induced by the geometry of deformation interacts with the local heterogeneous microstructure and micro-scale property distributions and affects the nucleation and evolution of damage and other microstructural changes such as phase transformation and twining. Furthermore, if the heterogenous material is exposed to a corrosive environment, it induces another set of complexities, Fig. 1.1(b). The final of

fracture of the material will now not only depend on the interaction of geometry of deformation and material microstructure but also on heterogeneous anodic dissolution and hydrogen adsorption. Thus, it is important to understand the synergistic effects of various heterogeneities or spatiotemporal length-scales induced by the material microstructure, geometry of deformation and loading conditions on the evolution of defects and damages leading to final fracture.

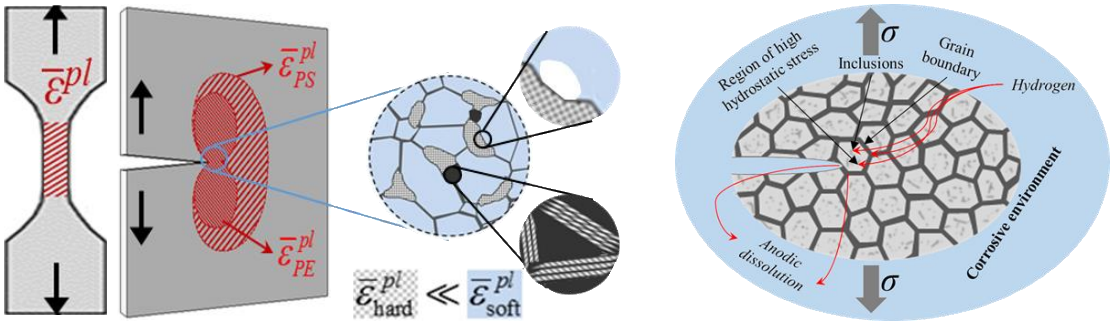

(a) (b)

Figure 1.1. Schematic showing the synergistic effects of various heterogeneities or spatiotemporal length-scales induced by the material microstructure, geometry of deformation and loading conditions on the fracture process (a) in a specimen with a notch (or crack) under mechanical loading and (b) in a specimen with a notch (or crack) under coupled mechanical-electrochemical loading.

A better understanding of the synergistic effects of various spatiotemporal length-scales induced by the material microstructure, geometry of deformation and loading conditions on the final fracture of a material underlies the development of new materials to meet the industrial need of lightweight yet durable structures. This will also pave the way to improve mechanistic theories and models needed for design and reliability analyses. Following this, the main aim of this dissertation is to understand the interactions of various spatiotemporal length-scales that dictate the final fracture of some of the most

technologically sought after advanced structural materials. The specific problems addressed in this dissertation are briefly summarized in the following paragraphs, while a detailed introduction and background of specific problems addressed herein are provided in the beginning of each chapter.

1.2. Brief overview

Intuitively a material's fracture resistance depends on its resistance to the creation of new free surfaces, as well as its deformation characteristics, which in turn are strongly influenced by the length-scales, arising from the material microstructure, geometry of deformation and loading conditions. Also, as noted in Fig. 1.1, these length-scales interact and evolve during the process of deformation and can greatly affect the deformation and fracture response of the material. The objective of the first part of this work is to demonstrate that the mechanical response of heterogeneous multiphase materials is fundamentally different in an imposed deformation field that is homogeneous, versus in an imposed deformation field that is heterogeneous, at a length-scale greater than the microstructural length-scale. To this end, the deformation and fracture of two low-carbon dual-phase advanced high strength steels, DF140T and DP980, with significantly different nominal composition and microstructure are characterized. The microstructures of both steels consist of hard martensite phase islands dispersed in a relatively soft ferrite phase matrix, but the amount of martensite in these two steels differ significantly, as can be seen in Fig. 1.2(a). However, the large difference in chemical composition and microstructure including phase composition and average phase size does not differentiate the mechanical response of these two materials under uniaxial tension as shown in Fig. 1.2(b). This

implies that any classical analysis will predict the same fracture response for these two materials based on their response under uniaxial tension.

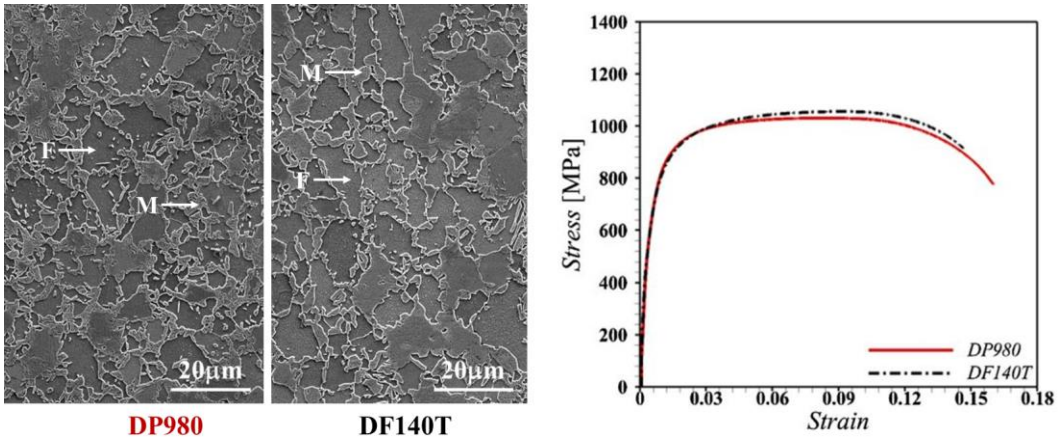

Figure 1.2. (a) SEM images showing the microstructures of the DP980 (left) and DF140T (right) dual-phase steels that are composed of ferrite (F) and martensite (M) phases. (b) Uniaxial tensile flow curves (engineering stress–strain) of the dual-phase steels with loading axis aligned parallel to the rolling direction. [1-3]

In this work, the mechanical response of these two steels is characterized by *in-situ* SEM (Scanning Electron Microscopy) tensile tests of flat dog-bone and single-edge notch specimens. The experimental results show that the dog-bone specimens of the two steels exhibit very similar mechanical response, but the mechanical response of their single-edge notch specimens differs significantly. As stated before, this contrasts with any classical analysis that will predict the same mechanical response in the presence of a notch for two materials that give the same mechanical response under uniaxial tension. The high-resolution *in-situ* tests coupled with microstructure-based digital image correlation and finite element analysis are then used to elucidate how the interlacing of imposed heterogeneous deformation field and material microstructure affects the mechanical

response of these steels. The results clearly highlight that a mechanistic analysis of multiphase materials under imposed heterogeneous deformation field must involve explicit consideration of the length-scales associated with the material microstructure.

Following the study on the effect of the interactions of geometry of deformation, loading condition and the material microstructure on fracture of dual-phase materials, the focus is confined to a single-phase ultra-high strength martensitic steel. The single-phase martensitic steel comprises of a complex hierarchical microstructure within the prior austenite grain (PAG) as shown in Fig. 1.3(a). The ultra-high strength martensitic steels with different PAG sizes also does not show significant difference in mechanical response under uniaxial tension as indicated in Fig. 1.3(b). However, the dependence of their ductility on the PAG size is rather ambiguous and it does not simply follow the typical strength-ductility trade-off associated with microstructure refinement. Specifically, one study [4] has reported that the ductility of low-carbon martensitic steels decreases with decreasing PAG size, and another study [5] has reported that it increases with decreasing PAG size, as shown in Figs. 1.3(c) and (d), respectively.

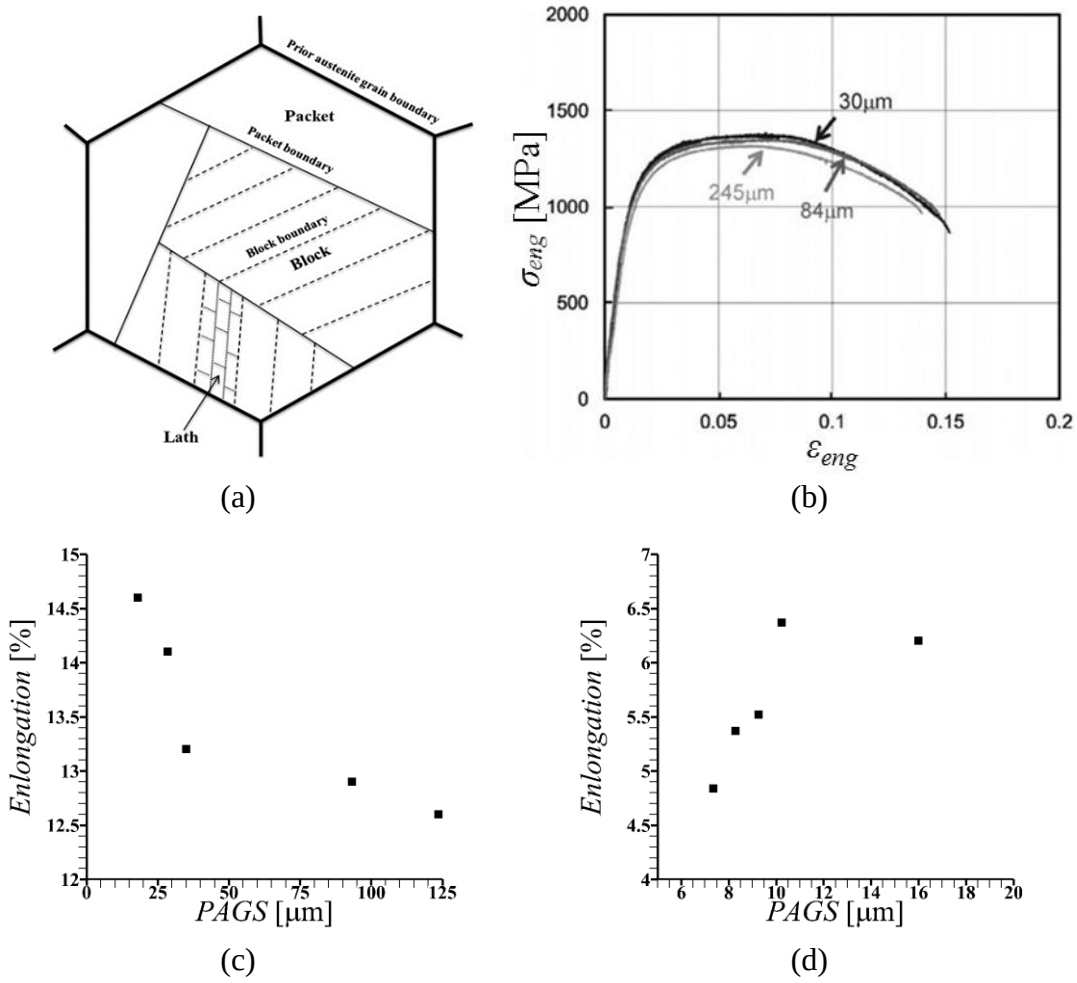

Figure 1.3. (a) Schematic showing the lath martensite microstructure typical of low carbon steels [6]; (b) Nominal stress-nominal strain curves for three martensite structures formed from prior austenite grain sizes of: 245 μm, 84 μm, and 30 μm [7]. (c) Positive and (d) negative correlation of ductility of low-carbon martensitic steels with increasing prior austenite grain size. Plotted with data from [4] and [5], respectively.

To study the effect of the PAG size on the ductility and fracture response of low-carbon martensitic steels, a low-carbon martensitic steel is subjected to five heat-treatments and the PAG microstructure in the material is reconstructed from the EBSD inverse pole figure maps of the martensitic microstructure. The deformation and fracture

response of all heat-treated materials are characterized by *in-situ* tension tests of dog-bone and single-edge notch specimens, to capture both the macroscopic mechanical response and the evolution of microscopic strains via microscale digital image correlation. The experimental results together with microstructure-based finite element analysis are then used to elucidate the effect of the PAG microstructure on the mechanical response of the material. The results show that the interaction of the heterogeneous deformation fields induced by the notch and the bimodal PAG size distribution leads to an increase in the propensity of shear strain localization and in turn degradation in the fracture response of the material with increasing heat-treatment temperature and time. The results also suggest that achieving a uniform distribution of fine grains is an effective way to enhance both the strength and fracture properties of this class of materials. Broader implications of these findings extend to both design and manufacturing analyses.

Next, the focus is on understanding the effects of the interactions of geometry of deformation, loading condition and evolving material microstructure due to deformation-induced twinning on fracture response of single crystals of a manganese rich austenitic steel. Austenitic manganese steels exhibit extremely high strain-hardening rate due to the activation of deformation-induced twinning. The deformation-induced twinning is readily observed in ⟨111⟩ oriented single crystals specimens under uniaxial tension. In these specimens twinning occurs at a very early stage of deformation (plastic strain < 5%), as shown in Fig. 1.4(a). At the early stage of deformation, the newly formed twin boundaries act as a barrier to dislocation glide resulting in dislocations pile-ups at the twin boundaries

and hence strain-hardening [8]. With continued deformation twin-twin interactions have also been proposed to contribute to the strain-hardening resulting in a stress-strain response with an concave upward shape [9]. The late stage twin-twin interactions in the ⟨111⟩ oriented specimens have been visualized by quantifying local deformation fields using microscale digital image correlation (DIC) technique, as shown in Fig. 1.4(b), which corresponds to significant increase in the strain-hardening rate [10].

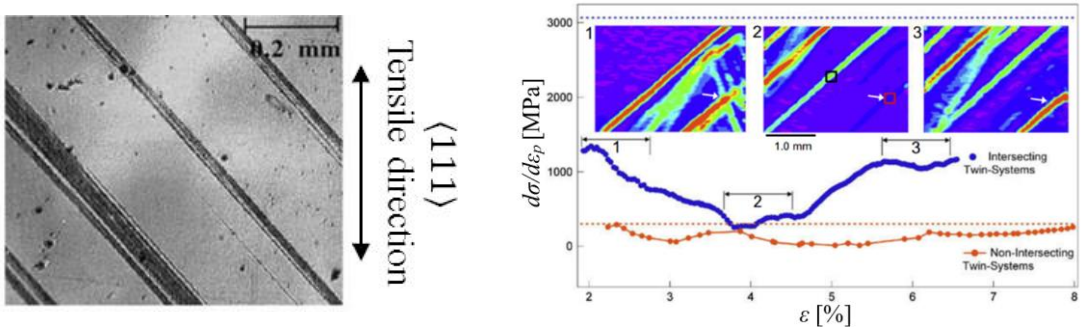

(a) (b)

Figure 1.4. (a) Hadfield steel single crystals under uniaxial tensile loading along the <111> direction deformed to a strain level of 5% at room temperature. Surface plane is <001> [9]; (b) Evolution of the strain-hardening rate with increasing applied deformation for the specimen with twin intersections (blue curve), and without twin intersections (red curve) [10].

In order to study the effects of deformation-induced twinning on the fracture response of a material, *in-situ* tensile tests of dog-bone and single-edge notch sheet specimens of carefully grown single crystals of an austenitic manganese steel are carried out. The crystallographic orientations of the single crystal specimens are chosen to selectively activate crystallographic slip or twinning. The *in-situ* tensile tests coupled with microscale Digital Image Correlation and Electron Backscattered Diffraction analysis allow simultaneously capturing macroscopic response, distribution of microscale strains,

and local microstructure evolutions. The results show that in single-edge notch specimens of preferably oriented single crystals, deformation-induced twinning occurs at a very early stage of deformation that leads to asymmetric deformation of the pre-existing notch. The cracks in these specimens predominantly grow along the twin boundaries, however, with increasing load, previously nucleated twins continue to widen that leads to crack tip blunting and crack growth arrest.

Finally, in this dissertation the synergistic effects of mechanical loading and corrosive environment on tensile response of a high strength aluminum alloy is investigated. High strength structural alloys are susceptible to premature failure due to the synergistic effects of environmental assisted degradation and mechanical loading, referred to as environmental assisted cracking (EAC). These alloys derive their exceptional properties from a complex, heterogeneous microstructure. But the underlying heterogeneous microstructure of the alloys affects the formation of the passive layer, as well as results in the formation of micron-scale galvanic cells, making them vulnerable to localized corrosive attacks. The process of localized corrosion is further aggravated by the presence of tensile loading. As shown in Figs. 1.5(a) and (b), the specimen under a constant loading, Fig. 1.5(a), exhibits a greater extent of damages at microscale than the unloaded specimen, Fig. 1.5(b).

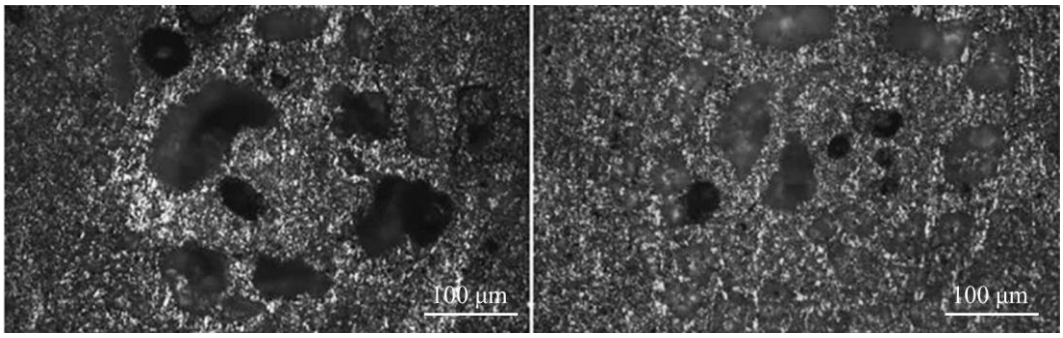

(a) (b)

Figure 1.5. Surface corrosion in the specimens of 7075-T6 aluminum alloy (a) with and (b) without mechanical loading after 2 hours of exposure to a corrosive environment [11].

To understand the synergistic effect of mechanical loading and corrosive environment on final fracture of a material, tensile specimens of AA7075 are subjected to a range of slow strain rate tensile loading in a very low pH corrosive environment. The degradation in mechanical response together with the emerging electrochemical characteristics of the material are characterized using electrochemical impedance spectroscopy (EIS). The EIS measurements coupled with the post-mortem microscopic characterization of the specimens provide an unprecedented view of all the interfacial phenomena affecting the mechanical response of the material. A failure mechanism of the material under consideration is proposed and rationalized by a qualitative fracture mechanics analysis.

In summary, in this dissertation an attempt has been made to understand the interactions of various spatiotemporal length-scales that dictate the final fracture of some of the most technologically sought after advanced structural materials using state-of-the-art *in-situ* experiments and microstructure-based simulations. The results presented in this dissertation will, hopefully, guide the development of new materials to meet the ever-

growing industrial need of lightweight yet durable structures, and will pave the way to microstructure-informed mechanistic theories and models for structural design and analysis.

2. EXPERIMENTAL METHODOLOGY

2.1. Sample preparation for *in-situ* mechanical testing

The mechanical response of a variety of advanced steels with complex microstructure is characterized by *in-situ* mechanical tests. For *in-situ* tensile tests, sub-sized flat dog-bone and single-edge notch tension specimens with axis parallel to the rolling direction of the steel sheets were machined using wire EDM. The length and width of the gauge section of the dog-bone specimens were 8 mm and 3 mm, respectively. The single-edge notch specimens had the same dimensions as the dog-bone specimen, but they contained an edge notch of depth 1.5 mm, machined using wire EDM or diamond saw in the center of the gauge section. The final tip radii of EDM machined notches were approximately 150 μm and 45 μm made by wire EDM and diamond saw, respectively. Prior to *in-situ* tensile testing, one surface of all the flat tension specimens was mechanically ground using 320 to 1200 grit SiC grinding papers and fine polished until 0.05μm alumina suspension. The mechanically polished specimens were chemically etched with 3% Nital for 15 sec to reveal the microstructure or were decorated with carefully dispersed 1 μm polycrystalline diamond particles.

2.2. *In-situ* mechanical testing

The *in-situ* mechanical tests were carried out using a Kammrath & Weiss tension module either inside a Tescan FERA-3 model Scanning Electron Microscope or under an Olympus DSX510 optical microscope. All the tension tests were carried out at a crosshead speed of 4 μm/sec giving a nominal uniaxial tensile strain rate of 0.5×10^{-3}sec^{-1} for the

dog-bone specimens. The *in-situ* tensile tests were interrupted at regular intervals to capture high-resolution micrographs of the deforming specimen surface.

2.3. Microscale digital image correlation

The series of SE images of the specimen surface captured during the *in-situ* mechanical test were then used to carry out microscale digital image correlation (DIC) by either tracking the contrast between various microstructural features or dispersed diamond particles. The DIC analyses were performed using the Ncorr open-source DIC software [12]. The Ncorr software utilizes a subset based DIC algorithm, where the reference image is partitioned into smaller regions referred to as subsets. The subsets are initially a contiguous circular group of points. In this work, subsets of radii 35 pixels with inter subset spacing of 1 pixel were used. The Ncorr software utilizes the inverse compositional method [13] for two-dimensional displacement field measurements, where the subsets in the current image are mapped with the subsets in the reference image via linear displacement mapping functions. The measured displacement fields were then used to estimate Lagrangian and/or Eulerian-Almansi strain measures.

2.4. Microstructural and fractographic analysis

For metallographic analysis, specimens were machined from both undeformed and deformed specimens. These metallographic specimens were mechanically ground using 320 to 1200 grit SiC grinding papers and fine polished until 0.05 μm alumina suspension for Electron Backscattered Diffraction (EBSD) characterization. In some cases, the mechanically polished specimens (especially those of dual-phase steels) were also chemically etched with 3% Nital for 15 sec to reveal the microstructure for Secondary

Electron (SE) characterization. EBSD and SE characterization were carried out using a (Tescan – FERA3) Scanning Electron Microscope (SEM) equipped with EBSD and SE detectors.

The fractographic analysis of the fractured specimens were carried out using a (Tescan – FERA3) SEM equipped with SE detector and/or optical microscopes (Olympus DSX510 optical microscope or Nikon SMZ 745T optical microscope with NI-150 high intensity illuminator as light source).

2.5. Slow strain rate corrosion test

The effect of corrosion and slow strain rate (SSR) loading on the mechanical behavior of a high strength aluminum alloy was analyzed using the Cortest CERT system equipped with an environmental chamber. The SSR tests in the corrosive environment were carried out at 5 nominal strain rates, 1.5×10^{-5}, 1.0×10^{-5}, 0.5×10^{-5}, 1.0×10^{-6} and $0.5\times10^{-6}s^{-1}$. The corrosive environment used was a solution containing 4*M* sodium chloride, 0.5*M* potassium nitrate, and 0.1*M* nitric acid. The initial pH of this solution is 0.4. The change in pH of the solution with time was also measured and it was found that the pH increases gradually with time, up until ~20 hours and then tends to saturate at a value slightly above 3.0 (at least until 50 hours). This solution is in general used for accelerated constant immersion exfoliation corrosion (EXCO) testing of high strength aluminum alloys [14].

A 3-electrode setup for Electrochemical Impedance Spectroscopy (EIS) was built to characterize the electrochemical response of the specimen deforming under SSR tensile loading in the corrosive environment. In this setup, the specimen was the working

electrode, graphite was the counter electrode, and the reference electrode was a saturated calomel electrode (SCE). The EIS measurements were carried out using Reference 600+ potentiostat by Gamry Instruments in the frequency range 10kHz to 10mHz and applied AC voltage of 10mV rms.

For the purpose of comparison, tensile tests in air were also carried out at a nominal strain rate of $10^{-3}s^{-1}$ using an MTS Insight 30 system and at a nominal strain rate of $10^{-5}s^{-1}$ using a Cortest Constant Extension Rate Testing (CERT) system. The extension in the gage section of all the specimens tested in air was measured using a non-contacting laser extensometer.

3. STRUCTURAL AND MICROSTRUCTRUAL INFLUENCE ON DEFORMATION AND FRACTURE OF DUAL-PHASE STEELS*

3.1. Introduction

Materials science of structural materials seeks the forward correlation of composition/processing, material microstructure and a set of mechanical properties. This forward correlation is likely unique i.e., a fixed composition/processing route leads to a unique microstructure that in turn leads to a unique set of mechanical properties. Intuitively, the inverse correlation of the same is not necessarily unique i.e., the same set of mechanical properties can be obtained from more than one microstructure resulting from different composition/processing routes. The key phrase here is "a set of mechanical properties." In general, mechanical properties of a ductile structural material are characterized via the standard tension test [15]. In the tension test, the gauge section of the test specimen undergoes homogeneous uniaxial tensile deformation at a length-scale greater than the microstructural length-scale at least until the onset of necking [16]. Thus, as long as the specimen size i.e. the structural length-scale is sufficiently greater than the microstructural length-scale, an unstructured continuum description of (a set of) mechanical properties can be obtained. These mechanical property descriptors are then be used for comparing materials, material development, structure/component design, quality control and reliability analysis, to name a few.

There is, however, an important difference between the characterization of mechanical response of a structural material in a deformation field that is homogeneous, versus in a deformation field that is heterogeneous at the structural length-scale, such as

*Reprinted with permission from "Structural and microstructural influence on deformation and fracture of dual-phase steels" by Xinzhu Zheng, Hassan Ghassemi-Armaki, Ankit Srivastava, 2020. Materials Science & Engineering A, 774, 138924, Copyright [2020] by Name of Xinzhu Zheng.

those observed in bending dominated manufacturing processes or in the vicinity of a structural discontinuity. In the former, characterization of mechanical response can be based on an unstructured continuum description of mechanical properties, such as strength and strain-hardening. On the contrary, in the latter, the characterization of mechanical response may also involve the length-scales associated with the material microstructure. This implies that even if the mechanical response of more than one microstructure is the same in a homogeneous deformation field, for example, under a tension test, it may still differ in a heterogeneous deformation field, for example, in the presence of a notch. This has far-reaching consequences in materials selection, development, and their use in critical applications.

The objective of this work is to experimentally demonstrate that two microstructures that lead to the same mechanical response in a homogeneous deformation field can lead to very different mechanical response in a heterogeneous deformation field. To this end, this work focus on two low-carbon dual-phase [17] advanced high strength steels [18], viz, DF140T and DP980, with significantly different nominal chemical compositions. Both of these steels were produced on a continuous annealing line that allows intercritical heating into the ferrite-austenite phase field followed by fast cooling to cause diffusionless martensitic transformation. The as-processed microstructure of both dual-phase steels consists of hard martensite phase particles dispersed in relatively soft ferrite phase matrix. However, the amount of ferrite and martensite phases, and their mechanical properties, such as strength and strain-hardening, in the as-processed microstructure of these two steels differ significantly [1-3].

Dual-phase advanced high strength steels are one of the most technologically sought after materials to enhance safety and efficiency of automobiles [19]. The microstructure – mechanical property correlation of dual-phase steels has been a topic of several experimental and computational studies [1-3, 20-51]. These studies have shown that under uniaxial tension, the stress-strain curves of dual-phase steels (with high martensite content) exhibit three characteristic stages: (i) at low loads the response is elastic and with increasing load yielding first occurs in the soft ferrite phase; (ii) following yielding in the ferrite phase, a period of rather strong strain-hardening is observed where the hard martensite phase remains elastic; and (iii) with further increase in load the martensite phase also reaches yield resulting in a significant reduction in the strain-hardening rate. These studies have also shown that dual-phase steels predominantly undergo ductile fracture at room temperature due to nucleation, growth and coalescence of voids, where void nucleation predominantly occurs by decohesion at ferrite – martensite interfaces and separation of adjacent or fractured martensite particles.

Here, a series of *in-situ* SEM tensile tests of flat dog-bone and single-edge notch specimens of DF140T and DP980 dual-phase advanced high strength steels is carried out. The tensile test of a dog-bone specimen corresponds to an imposed homogeneous deformation field (at least until the onset of necking) whereas that of a single-edge notch specimen corresponds to an imposed heterogeneous deformation field at the structural length-scale. The high-resolution *in-situ* SEM tensile tests coupled with microstructure-based digital image correlation [23, 24, 35, 36, 38] allows to capture both the macroscopic mechanical response and the distribution of microscale strains on the specimen surface.

The experimental results show that despite significantly different microstructure, microscale property distribution and microscale deformation, the dog-bone specimens of the two steels exhibit very similar mechanical response at macroscale. However, the mechanical response of the single-edge notch specimens of the two steels differs significantly.

The microscale strain measurements (prior to the onset of necking/fracture) coupled with fractographic analyses suggest that the interlacing of heterogeneous deformation field at the structural and the microstructural length-scales affects the deformation and fracture response of dual-phase steels. Microstructure-based finite element analyses of tensile tests of flat dog-bone and single-edge notch specimens of both the steels are also carried out to complement the conclusions drawn from the experimental observations. In the finite element calculations, the SEM images of the microstructures of the steels under consideration are directly utilized to generate two-dimensional finite element meshes and the constitutive properties of the constituent phases are obtained from the coupled micropillar compression test and finite element calculation results of refs. [1-3].

3.2. Material and method

The dual-phase advanced high strength steels examined in this work are DF140T with nominal chemical composition of 0.15%C – 1.45%Mn – 0.3%Si (wt.%) and DP980 with nominal chemical composition of 0.09%C – 2.15%Mn – 0.6%Si (wt.%). Both steels were produced on a water – quenched continuous anneal line by ArcelorMittal. The

sample preparation follows the procedure in **2.1** and the final thickness of the polished and etched tension specimens was approximately 1.35 mm.

In-situ tensile tests are performed on dog-bone and single-edge notch specimens of DF140T and DP980 as described in **2.2**. The series of high-resolution SE images of the surface microstructure captured during a tensile test were then used to carry out microstructure-based DIC by tracking the contrast between the microstructural features, as mentioned in **2.3**. The characterization of microstructure of undeformed materials and fractography analysis are performed using the procedure mentioned in **2.4**.

3.3. Experimental results

3.3.1. Material microstructure and macroscale mechanical response

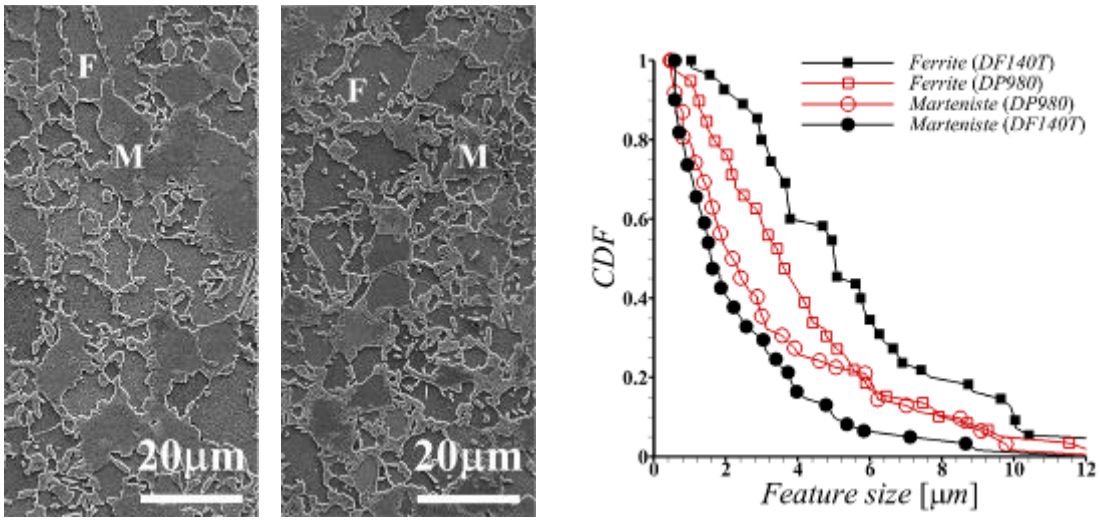

(a) (b) (c)

Figure 3.1. SE-SEM images of initial microstructures of (a) DF140T and (b) DP980 dual-phase (ferrite (F) and martensite (M)) advanced high strength steels. (c) The descending cumulative distribution function (CDF) of the size of ferrite and martensite regions in the initial microstructure of DF140T and DP980 dual-phase advanced high strength steels.

The SE-SEM images of the mechanically polished and chemically etched specimens of undeformed DF140T and DP980 steels are shown in Figs. 3.1(a) and (b),

respectively. The microstructure of both the steels consists of islands of hard martensite particles dispersed in a matrix of relatively soft ferrite grains. The microstructure of DF140T is composed of ~39±2% martensite and rest ferrite, while that of DP980 is composed of ~61±3% martensite and rest ferrite. The descending cumulative distribution function (CDF) curves of the size of ferrite and martensite regions in both the steels are shown in Fig. 3.1(c). The CDF curves can be interpreted as displaying the probability that the size of a feature will exceed a given value on the horizontal axis. From Fig. 3.1(c), it is clear that the probability that the size of ferrite region will exceed a given threshold is greater in DF140T, whereas the probability that the size of martensite region will exceed a given threshold is greater in DP980. If ignore the smallest 5% and largest 5% feature sizes, in DF140T the size of ferrite region lies within 1.83-11.32 μm and the size of martensite region lies within 0.59-7.15 μm. Similarly, in DP980 the size of ferrite region lies within 1.05-9.60 μm and the size of martensite region lies within 0.52-9.44 μm. So that, on average the size of ferrite region is greater in DF140T compared to DP980, whereas the size of martensite region is greater in DP980 compared to DF140T.

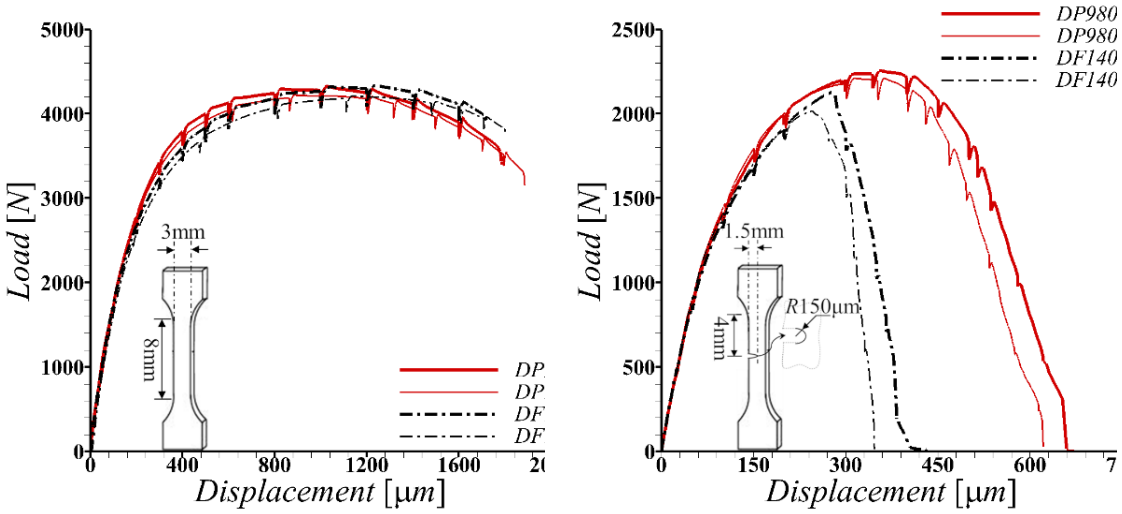

(a) (b)

Figure 3.2. Two sets of load-displacement curves of flat (a) dog-bone and (b) single-edge notch tension specimens of DF140T and DP980 dual-phase advanced high strength steels. The small drops in load at regular displacement intervals are caused by interrupting the test to capture high-resolution SE-SEM images of the evolving microstructure on the specimen surface.

The load-displacement curves of flat dog-bone and single-edge notch specimens of DF140T and DP980 steels under tension are shown in Figs. 3.2(a) and (b), respectively. All the tensile tests were carried out inside an SEM and the tests were interrupted at regular intervals to capture SE images of the evolving surface microstructure. The small drops in load at regular displacement intervals in Fig. 3.2 mark the interruption of tensile loading. As shown in Fig. 3.2(a), the tensile response of the dog-bone specimens of both the steels is very similar with ultimate tensile strength i.e. maximum load (~4300N) normalized by the initial cross-section area of the gauge section of the dog-bone specimens of both the steels being ~1GPa. However, the tensile response of single-edge notch specimens of the two steels differs significantly, Fig. 3.2(b). The single-edge notch specimens of DP980 steel can withstand greater than 6% load and exhibit more than 60% greater extension

prior to fracture as compared to the single-edge notch specimens of DF140T steel. Note that for two materials with very similar mechanical response under uniaxial tension, any classical fracture mechanics-based analysis will predict similar response in the presence of a structural defect such as a notch. The results presented in Fig. 3.2 clearly highlight the difference between the characterization of mechanical response of multiphase materials in an imposed deformation field that is homogeneous, versus in an imposed deformation field that is heterogeneous at the structural length-scale.

3.3.2. Microscale deformation field

A series of SE-SEM images of the evolving microstructure on the surface of the flat tension specimen were captured to characterize the in-plane microscale deformation field via microstructure-based DIC. The distribution of the ε_{xx} strain (strain along the tensile loading direction) in the reference configuration in a 300-by-300 μm^2 region in the center of the gauge section of the dog-bone tension specimen of DF140T and DP980 steels deformed to a (macroscale) displacement of 600μm is shown in Fig. 3.3(a). At this point, the dog-bone tension specimens of both the steels are within the uniform deformation regime, see Fig. 3.2(a). In Fig. 3.3(a), the values of ε_{xx} less than the value of ε_{xx} at the edges parallel to y-axis of the 300-by-300 μm^2 box, ε_{xx}^{box}, are whitewashed to highlight the regions of strain concentration. As shown in the figure, even though the dog-bone tension specimens of both the steels at macroscale are within uniform deformation regime, at microscale the deformation is extremely heterogeneous. Also, even though at macroscale the mechanical response of the dog-bone specimen of both the steels is very similar, at microscale the heterogeneous deformation is more pronounced in DF140T steel compared

to DP980 steel. In the dog-bone specimen of DF140T steel, under imposed tensile loading along x-axis, ε_{xx} localizes in bands that are (roughly) oriented orthogonal to the loading direction even before the onset of maximum load.

The evolution of heterogeneous deformation, in particular, the extent of strain concentration at microscale in the dog-bone tension specimen of DF140T and DP980 steels is quantified in Fig. 3.3(b). Figure 3.3(b) shows the evolution of the area fraction of various levels of ε_{xx} greater than the current value of ε_{xx}^{box} with imposed (macroscale) displacement. The results in Fig. 3.3(b) are only presented up to an imposed displacement of 1000μm which is within the macroscopic uniform deformation regime, see Fig. 3.2(a). As shown in Fig. 3.3(b), at an imposed displacement of 200μm, the area fraction of all levels of strain concertation, $\varepsilon_{xx}/\varepsilon_{xx}^{box}$, is greater in DF140T steel compared to DP980 steel. With progressive deformation (increasing imposed displacement), the area fraction of all levels of $\varepsilon_{xx}/\varepsilon_{xx}^{box}$ first decreases due to the onset of plastic deformation in both ferrite and martensite phases and then tends to increase gradually in both the steels. At greater imposed displacements, the area fraction of low levels of $\varepsilon_{xx}/\varepsilon_{xx}^{box}$ is roughly the same in both the steels. However, the area fraction of $\varepsilon_{xx}/\varepsilon_{xx}^{box} > 1.2$ is greater in DF140T compared to DP980, highlighting the extremely heterogeneous deformation with regions of extremely high strain concertation in DF140T.

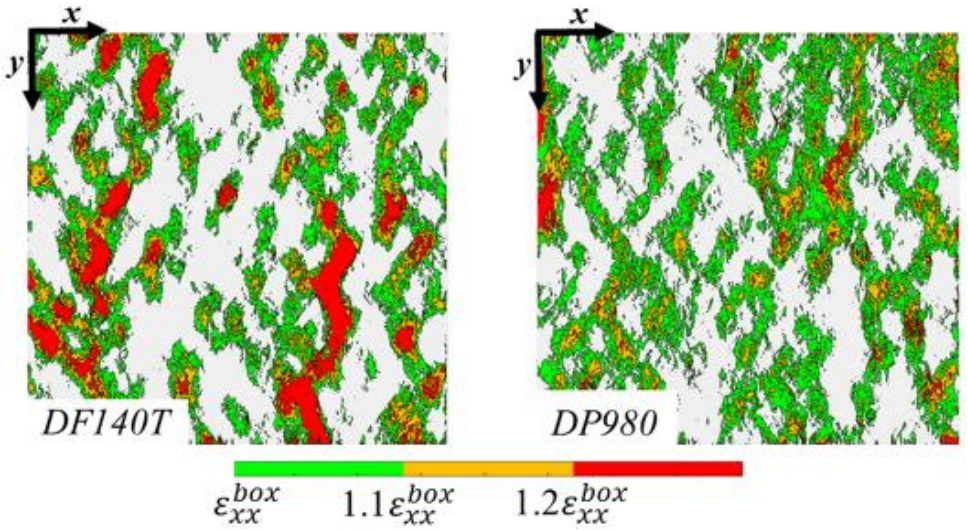

(a)

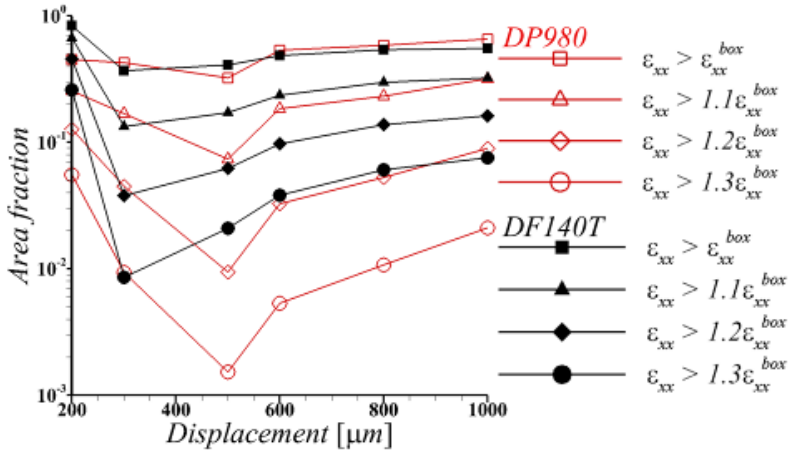

(b)

Figure 3.3. (a) The distribution of the ε_{xx} strain in a 300-by-300μm^2 region in the center of the gauge section of the dog-bone tension specimen of DF140T and DP980 steels deformed to a (macroscale) displacement of 600μm. In (a) the values of ε_{xx} less than the value of ε_{xx} at the edges parallel to *y*-axis of the region of interest i.e. the 300-by-300μm^2 box, ε_{xx}^{box}, are white washed to highlight the regions of strain concentration. The tensile loading direction in (a) is along *x*-axis and the value of $\varepsilon_{xx}^{box} \approx 0.04$ for both the steels. (b) The evolution of the area fraction of various levels of ε_{xx} greater than the current value of ε_{xx}^{box} in the regions shown in (a) with imposed displacement on the dog-bone tension specimen of DF140T and DP980 steels. The *y*-axis in (b) is on logarithmic scale.

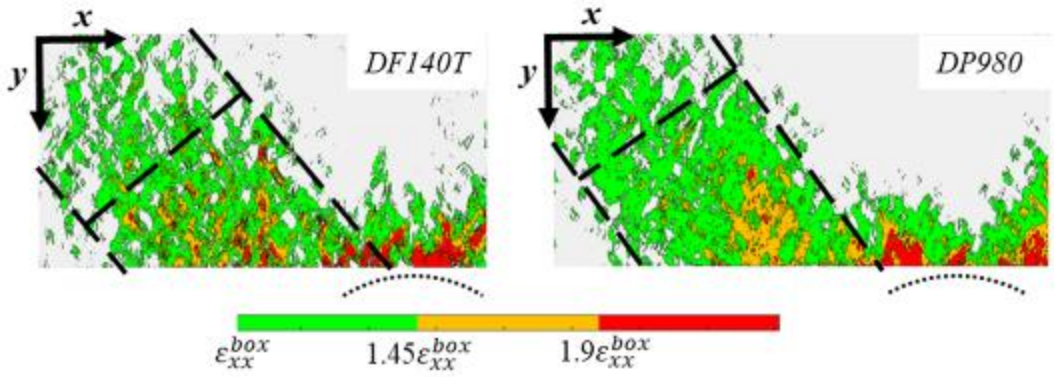

(a)

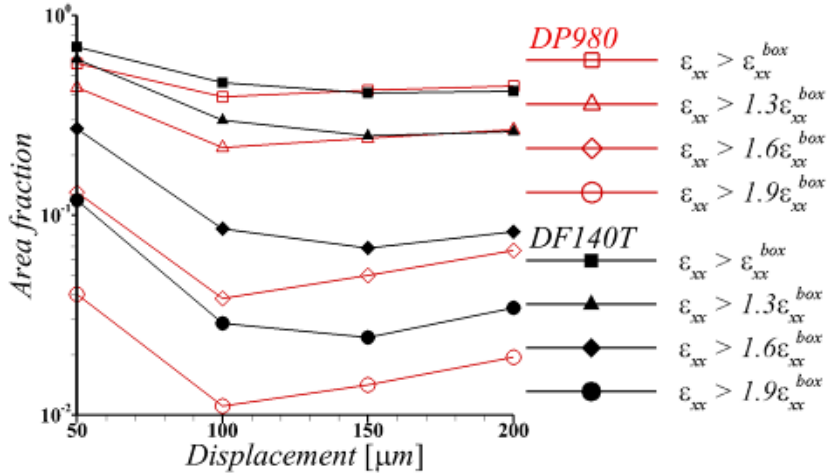

(b)

Figure 3.4. (a) The distribution of the ε_{xx} strain in a 500-by-250μm^2 region near the notch in the single-edge notch tension specimen of DF140T and DP980 steels deformed to a (macroscale) displacement of 200μm. In (a) the values of ε_{xx} less than the value of ε_{xx} at the edges parallel to *y*-axis of the region of interest i.e. the 500-by-250μm^2 box, ε_{xx}^{box}, are white washed to highlight the regions of strain concentration. The tensile loading direction in (a) is along *x*-axis, the initial notch is along y-axis and the dotted arc marks the location of the notch tip. The value of $\varepsilon_{xx}^{box}\approx 0.052$ for DF140T steel and $\varepsilon_{xx}^{box}\approx 0.05$ for DP980 steel. (b) The evolution of the area fraction of various levels of ε_{xx} greater than the current value of ε_{xx}^{box} in the regions shown in (a) with imposed displacement on the single-edge notch tension specimen of DF140T and DP980 steels. The *y*-axis in (b) is on logarithmic scale.

The distribution of the ε_{xx} strain in the reference configuration in a 500-by-250μm^2 region near the notch in the single-edge notch tension specimen of DF140T and DP980 steels deformed to a (macroscale) displacement of 200μm is shown in Fig. 3.4(a).

At the imposed displacement of 200μm neither of the single-edge notch tension specimens have reached the maximum load. As shown in Fig. 3.2(b), the single-edge notch specimens of DF140T achieve an average maximum load of ~2092N at an average extension of ~262μm while those of DP980 achieve an average maximum load of ~2237N at an average extension of ~330μm. In Fig. 3.4(a), the values of ε_{xx} less than the value of ε_{xx} at the edges parallel to the *y*-axis of the 500-by-250μm^2 box, ε_{xx}^{box}, are whitewashed to highlight the regions of strain concentration. As shown in the figure, in the single-edge notch tension specimen of both the steels, ε_{xx} localizes in wide bands originating from the corners of the deformed notch. Within this band the deformation is more heterogeneous with regions of greater strain concentrations for DF140T steel compared to DP980 steel. The difference between the deformation at microscale in the steels seen in Fig. 3.4(a) can be explained at least qualitatively based on the results shown in Fig. 3.3(a). Nevertheless, unlike the dog-bone specimen, the macroscale tensile response of the single-edge notch specimen of these steels differs significantly, see Fig. 3.2.

Similar to Fig. 3.3(b), the evolution of the extent of strain concentration at microscale in the single-edge notch tension specimen of both the steels is quantified in Fig. 3.4(b). The results in Fig. 3.4(b) are only presented up to an imposed displacement of 200μm which is before the onset of maximum load in Fig. 3.2(b). As shown in Fig. 3.4(b), at an imposed displacement of 50μm, the area fraction of all levels of strain concertation, $\varepsilon_{xx}/\varepsilon_{xx}^{box}$, is greater in DF140T steel compared to DP980 steel. With progressive deformation (increasing imposed displacement), the area fraction of all levels of $\varepsilon_{xx}/\varepsilon_{xx}^{box}$ first decreases and then tends to increase gradually in both the steels. At greater imposed

displacements, the area fraction of low levels of $\varepsilon_{xx}/\varepsilon_{xx}^{box}$ is roughly the same in both the steels. However, the area fraction of $\varepsilon_{xx}/\varepsilon_{xx}^{box} > 1.6$ is greater in DF140T compared to DP980, highlighting the extremely heterogeneous deformation with regions of extremely high strain concertation in DF140T as shown in Fig. 3.4(a).

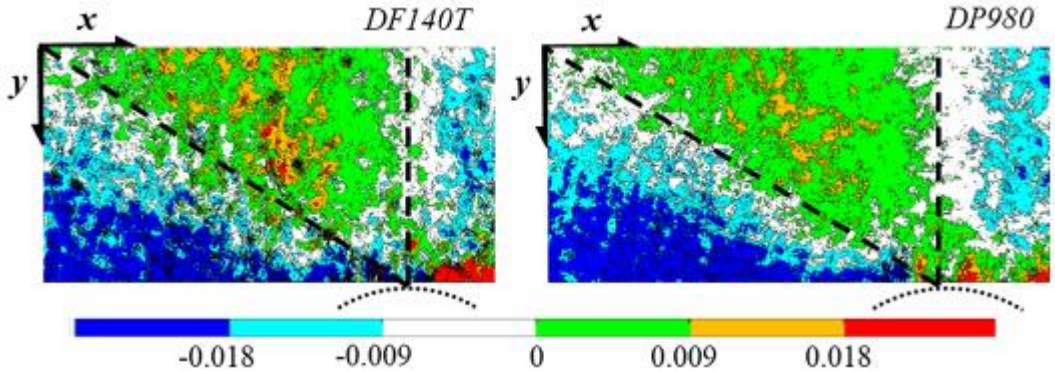

Figure 3.5. The distribution of the ε_{xy} strain in a 500-by-250μm^2 region near the notch in the single-edge notch tension specimen of DF140T and DP980 steels deformed to a (macroscale) displacement of 200μm. The tensile loading direction is along *x*-axis, the initial notch is along y-axis and the dotted arc marks the location of the notch tip.

In a single-edge notch tension specimen, the regions near the free surface may exhibit greater shear-driven plastic deformation as the stress along the thickness direction approaches zero on the free surface of the specimen. Thus, it is imperative to analyze the extent of shear strain concentration at microscale in the single-edge notch specimen of both the steels. The microscale distribution of in-plane shear strain, ε_{xy}, in the reference configuration in the single-edge notch tension specimen of both the steels in the same regions and at the same imposed displacement as in Fig. 3.4(a) is shown in Fig. 3.5. In both the steels, the positive values of ε_{xy} concentrate in triangular bands originating from the notch tip, while the values of ε_{xy} are negative on the left side of these triangular bands.

The zero shear region between the two shear directions (positive and negative) is most susceptible to damage initiation. Like Fig. 3.4(a), in Fig 3.5 as well, within the region of negative and positive values of ε_{xy}, the distribution of ε_{xy} is more heterogeneous with regions of greater strain concentrations in DF140T steel as compared to DP980 steel.

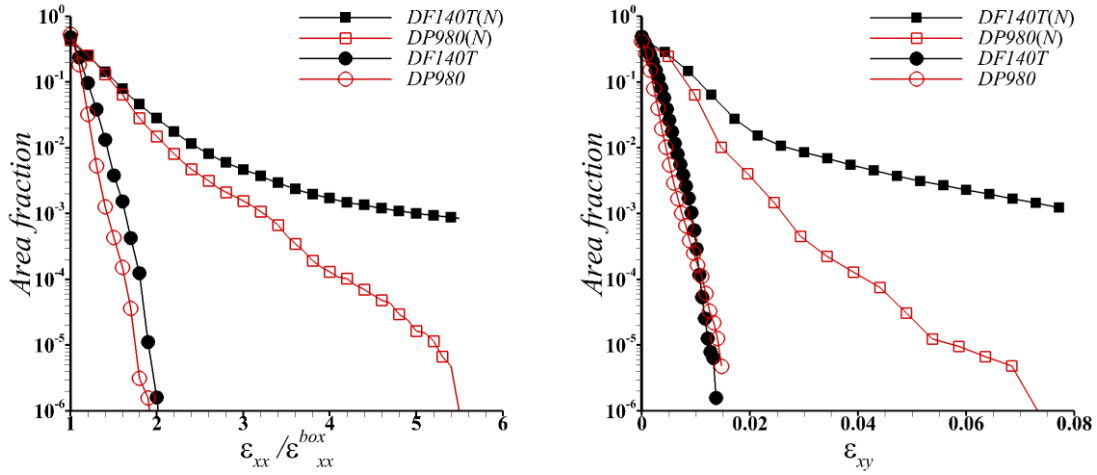

Figure 3.6. The variation of the area fraction of various levels of (a) $\varepsilon_{xx}/\varepsilon_{xx}^{box}$ and (b) ε_{xy} in a 300-by-300μm^2 region in the center of the gauge section of the dog-bone tension specimen and in a 500-by-250μm^2 region near the notch in the single-edge notch tension specimen (*N*) of DF140T and DP980 steels. For both the steels, the dog-bone tension specimen was deformed to a (macroscale) displacement of 600μm and the single-edge notch tension specimen was deformed to a displacement of 200μm. The *y*-axes in (a) and (b) are on logarithmic scale.

Figures 3.3, 3.4 and 3.5, show that at the same imposed (macroscopic) displacement the deformation at the microstructural length-scale is more heterogeneous with regions of greater strain concentrations in DF140T steel compared to DP980 steel in both the dog-bone and the single-edge notch tension specimens. To further quantify the extent of strain concentration or localization in the dog-bone and the single-edge notch tension specimens of the two steels, the variation of the area fraction of various levels of

$\varepsilon_{xx}/\varepsilon_{xx}^{box}$ and ε_{xy} at a fixed imposed displacement is considered, Fig. 3.6. As shown in Fig. 3.6, the area fraction of a given level of $\varepsilon_{xx}/\varepsilon_{xx}^{box}$ and ε_{xy} is in general greater in the single-edge notch specimen compared to the dog-bone specimen in both the steels. In the dog-bone specimen, the area fraction of both $\varepsilon_{xx}/\varepsilon_{xx}^{box}$ and ε_{xy} decreases with increasing values of $\varepsilon_{xx}/\varepsilon_{xx}^{box}$ and ε_{xy}, respectively, in both the steels. Also, the area fraction of a given level of $\varepsilon_{xx}/\varepsilon_{xx}^{box}$ and ε_{xy} is in general slightly greater in the dog-bone specimen of DF140T steel compared to that of DP980 steel. In the single-edge notch specimen of DP980 the area fraction of both $\varepsilon_{xx}/\varepsilon_{xx}^{box}$ and ε_{xy} also decreases with increasing values of $\varepsilon_{xx}/\varepsilon_{xx}^{box}$ and ε_{xy}, respectively. However, in the single-edge notch specimen of DF140T the area fraction of $\varepsilon_{xx}/\varepsilon_{xx}^{box}$ and ε_{xy} only decreases initially with increasing values of $\varepsilon_{xx}/\varepsilon_{xx}^{box}$ and ε_{xy}, respectively, and beyond a critical value of $\varepsilon_{xx}/\varepsilon_{xx}^{box}$ and ε_{xy} their area fraction tends to saturate, suggesting localization of both ε_{xx} and ε_{xy}.

3.3.3. Fracture characteristics

SE-SEM images of the fracture surface of the dog-bone tension specimen of DF140T and DP980 steels are shown in Fig. 7. The qualitative morphology of the fracture surface of the dog-bone tension specimen of both the steels is roughly the same. The fracture surface of both the steels exhibits a dimpled morphology indicative of ductile fracture due to nucleation, growth and coalescence of microscale voids. The fracture surface of both the steels at greater magnification shows large and deep holes together with relatively small dimples. The bimodal distribution of dimples on the fracture surface

is characteristics of dual-phase materials undergoing elastic-plastic deformation in both the phases [3].

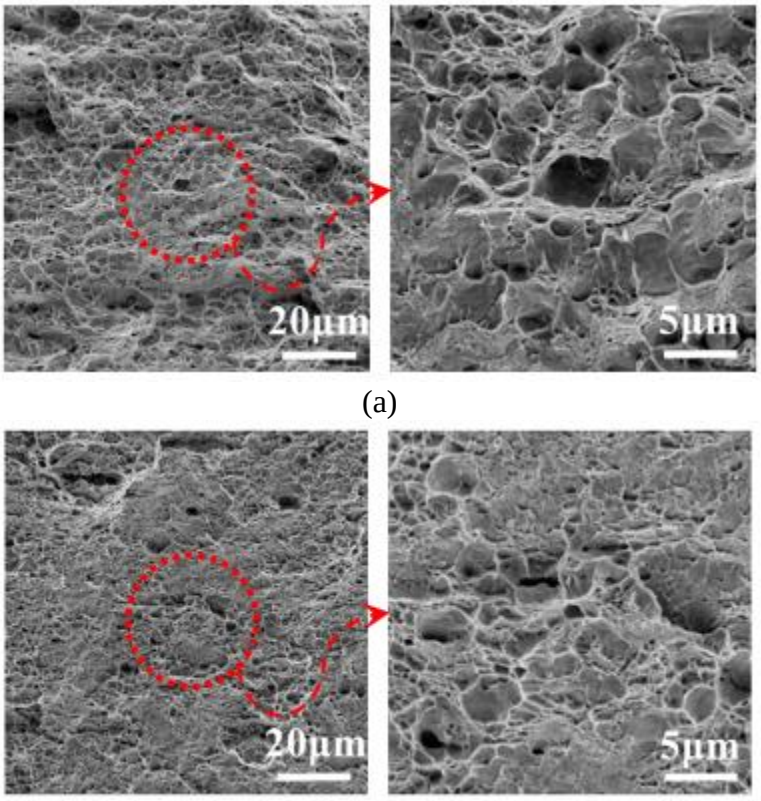

Figure 3.7. SE-SEM images of the fracture surface showing the fracture morphologies of one-half of the flat dog-bone tension specimen of (a) DF140T and (b) DP980 dual-phase advanced high strength steels. The tensile loading direction is into the viewed plane. Magnified views of regions marked with dotted circles in left images are shown in right images.

Figure 3.8 shows SE-SEM images of the fracture surface of the single-edge notch tension specimen of DF140T and DP980 steels. The crack growth direction in the specimens of both the steels is marked with arrows in the left most low magnification image in Figs 3.8(a) and (b), and the thickness of the flat specimens is along the vertical edges of the image. The low magnification image of the fracture surface of DF140T steel shows formation of shear lips near the free surfaces (horizontal edges of the image) of the

specimen. For DF140T steel, the maximum reduction in the thickness of the fractured specimen (near the notch root) was found to be ≈9.8% and the minimum reduction in the thickness of the fractured specimen (away from the notch root) was found to be ≈8.3%. On the contrary, the image taken at the same low magnification of the fracture surface of DP980 shows through thickness necking at the root of the deformed notch. For DP980 steel, the maximum reduction in the thickness of the fractured specimen (near the notch root) was found to be ≈23.3% and the minimum reduction in the thickness of the fractured specimen (away from the notch root) was found to be ≈12.0%. This clearly shows that the single-edge notch specimen of DP980 steel first underwent through thickness necking which was then followed by damage evolution and crack initiation in center of the neck. However, in the single-edge notch specimen of DF140T steel a thumbnail shaped crack initiated along the thickness of the specimen without significant through thickness necking.

The magnified images of the regions that are marked A near the notch root in the left most images in Figs 3.8(a) and (b) show large and deep holes together with relatively small dimples in both the steels. In addition to dimples, for DF140T steel, the image labelled A in Fig. 3.8(a) also shows presence of depressions with sides resembling quasi-cleavage like planes suggesting pullout of hard precipitates from the relatively soft matrix. The magnified view of the fracture surface away from the notch root that is labelled B in Fig. 3.8(a) shows no change in the fracture surface morphology with progressive crack growth in the specimen of DF140T steel. However, the magnified view of the fracture surface away from the notch root in the specimen of DP980 steel, labelled B in Fig. 3.8(b),

is different from the fracture surface morphology near the notch root, see the image labelled A in Fig. 3.8(b). The fracture surface morphology away from the notch root in the specimen of DP980 steel contains relatively large quasi-cleavage like planes together with dimples. This is likely due to overload in the ligament post necking.

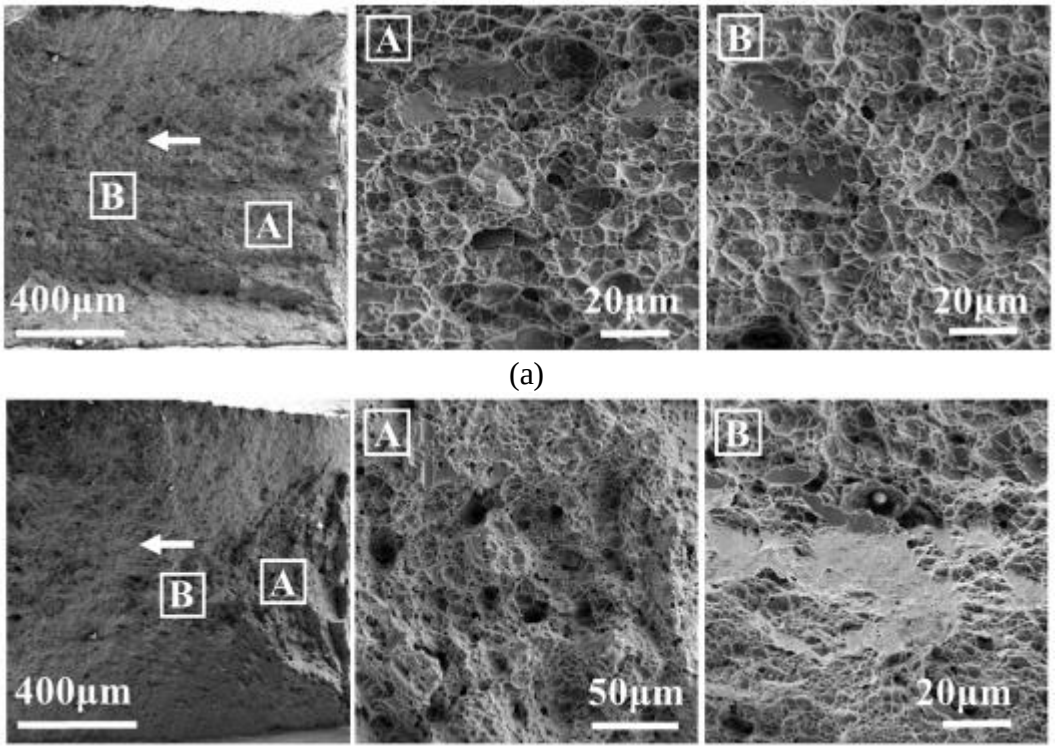

Figure 3.8. SE-SEM images of the fracture surface showing the fracture morphologies of one-half of the flat single-edge notch tension specimen of (a) DF140T and (b) DP980 dual-phase advanced high strength steels. The tensile loading direction is into the viewed plane. Magnified views of regions marked as A and B in left most images are shown in center and right images, respectively.

3.4. Discussion

The experimental results show that despite significantly different nominal chemical composition and microstructure, the dog-bone tension specimens of DF140T and DP980 dual-phase steels exhibit very similar mechanical response. However, despite this,

the mechanical response of the single-edge notch tension specimens of these two steels differs significantly. This is in contrast to any classical analysis that will predict the same mechanical response in the presence of a notch for two materials that have the same mechanical response under uniaxial tension. Furthermore, the microscale strain measurements, prior to the onset of maximum load (i.e., necking or fracture), show that irrespective of the similarities in the mechanical response of the dog-bone specimens and differences in the response of the single-edge notch specimens, the deformation at the microstructural length-scales in the two steels is always different. At the microstructural length-scale the deformation in both types of specimens of both the steels is always heterogeneous with the heterogeneous deformation being more pronounced in DF140T steel compared to DP980 steel. A quantitative analysis of the extent of strain concentration in both types of specimens of both the steels revealed that the single-edge notch specimen of DF140T steel exhibits in-plane localization of deformation. The in-plane localization of deformation in the single-edge notch specimen of DF140T steel results in onset of fracture without significant deformation along the out-of-plane (thickness) direction of the flat specimen. On the contrary, in the single-edge notch specimen of DP980 steel, onset of fracture occurs post out-of-plane necking near the notch root.

At the structural length-scale, in a dog-bone specimen, the stress state is uniaxial, and the deformation is more or less uniform up until the onset of necking, whereas in a single-edge notch specimen, the stress state is quite complex, and the deformation is always heterogeneous. Thus, it can be hypothesized that the interlacing of the heterogenous deformation at the structural and the microstructural length-scales leads to

the in-plane localization of deformation in the single-edge notch specimens of DF140T steel. To proof this hypothesis, microstructure-based finite element analyses of the dog-bone and the single-edge notch tension specimens of both the steels are carried out. Schematic representations of the microstructure-based finite element models of the two-dimensional plane strain dog-bone and single-edge notch specimens of the two steels under consideration are shown in Fig. 3.9. In theory, it is possible to carry out microstructure-based finite element analyses of the full three-dimensional dog-bone and single-edge notch specimens. However, the finite element mesh density required to discretely model the micron-size microstructural features in the specimens of dimensions in millimeters will render the calculations prohibitively time consuming. Thus, for the dog-bone specimen, a two-dimensional slice of material with dimensions 500μm along *x*-axis and 250μm along *y*-axis is considered while for the single-edge notch specimen, half of the gauge section i.e., a slice of material with dimensions 2mm along *x*-axis and 3mm along *y*-axis with a notch of depth 1.5mm along *y*-axis and tip radius 150 μm (located along the symmetry line OO', Fig. 3.9) is considered for numerical analyses.

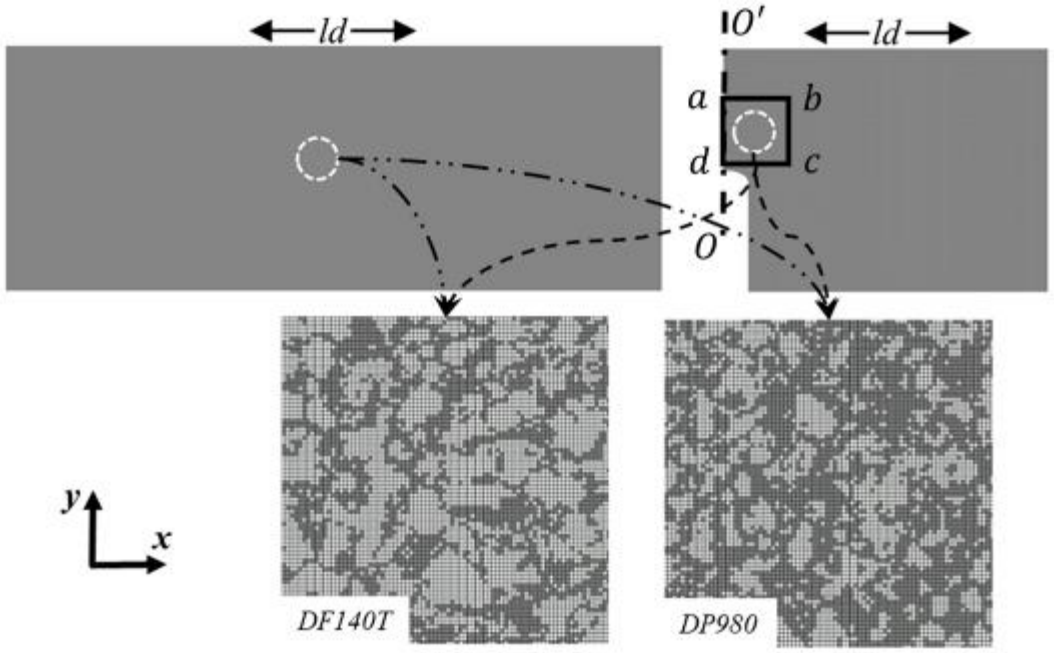

Figure 3.9. Schematic showing a slice of defect free region of the gauge section of the dog-bone specimen and a slice of one-half of the single-edge notch specimen together with zoomed-in view of finite element mesh and superimposed dual-phase microstructure of DF140T and DP980 dual-phase advanced high strength steels.

The finite element calculations are carried out using the commercial finite element code ABAQUS/Standard [52]. To simulate the tension test of flat dog-bone specimen the 500μm×250μm slice of specimen is subjected to uniaxial velocity along *x*-axis on the two free edges parallel to *y*-axis, Fig. 9. To simulate the tension test of flat single-edge notch specimen, the one-half specimen, Fig. 3.9, is subjected to *y*-axis symmetry boundary conditions along OO' and uniaxial velocity along *x*-axis on the free edge parallel to *y*-axis. The finite element meshes use eight-node plane strain, CPE8R, elements of the ABAQUS/Standard element library [52]. The finite element mesh of 500μm×250μm slice of specimen contains 500×250 elements. The half single-edge notch specimen contains 400×400 elements in 400μm×400μm region close to the notch tip (marked as *abcd* in Fig.

3.9), and rather coarse mesh outside *abcd*. Next, to generate the discrete dual-phase microstructures in the finite element models, grayscale SEM images of microstructures of the two steels are superimposed on the finite element mesh and the material properties corresponding to respective microstructural features are assigned based on elements. In the $500\mu m \times 250\mu m$ slice of specimen, the dual-phase microstructures are discretely modeled throughout the specimen whereas, in the half single-edge notch specimen, the dual-phase microstructures are discretely modeled only in the region marked as *abcd* in Fig. 3.9. The region outside *abcd* in the half single-edge notch specimen is assigned the material properties corresponding to the overall (homogenized) mechanical response of the two steels under consideration.

In the microstructure-based finite element calculations, both ferrite and martensite phases and the overall (homogenized) dual-phase steels are modeled as rate-independent isotropic elastic-plastic material within finite strain J_2 flow theory. The Young's modulus and Poisson's ratio of both the phases and homogenized dual-phase steels are taken to be, 210GPa and 0.3, respectively. The plastic response of both the phases and the homogenized dual-phase steels is modeled using the constitutive relation proposed in ref. [2],

$$\sigma_e = \sigma_0 + k_1\left(1-\exp\left(-k_2\varepsilon_e^p\right)\right) + h_s\left(\varepsilon_e^p\right)^n \tag{3.1}$$

where the first term marks the onset of plastic deformation in the soft ferrite phase, the second term represents the strong strain-hardening regime where the hard martensite phase largely remains elastic and the ferrite phase undergoes plastic deformation, and the third term represents the power-law strain-hardening regime in which both the phases undergo

plastic deformation. Also, with the value of $k_1 = 0$, Eq. (3.1) reduces to simple Ludwik type constitutive relation that can be used to capture the stress-strain response of the constituent phases. The values of the constitutive parameters in Eq. (3.1) that best represent the plastic response of both the constituent phases (ferrite and martensite) of the two steels (DF140T and DP980) under consideration and their overall plastic response are obtained from the coupled micropillar compression test results of ref. [1] and representative volume element finite element calculations of refs. [2, 3]. The final values of all the constitutive parameters for both the phases present in both the steels and for their overall plastic response are given in Table 3.1. The predicted nominal uniaxial stress-strain response of both the phases present in the two steels, and the predicted overall nominal uniaxial stress-strain response of the two steels using the constitutive parameters in Table 3.1 are shown in Fig. 3.10.

Table 3.1: The values of the constitutive parameters in Eq. (3.1) that characterize the plastic response of both the phases (ferrite and martensite) and that of homogenized dual-phase, DF140T and DP980, advanced high strength steels.

	σ_0 (MPa)	k_1 (MPa)	k_2	h_s (MPa)	n
Ferrite (DF140T)	560.3	0	0	623.7	0.53
Martensite (DF140T)	1655.3	0	0	1628.2	0.39
Homogenized DF140T	430.0	367.9	464.8	1149.2	0.45
Ferrite (DP980)	542.5	0	0	3520.5	0.94
Martensite (DP980)	1072.7	0	0	688.2	0.45
Homogenized DP980	430.0	309.4	634.8	1222.6	0.44

The key results of the microstructure-based finite element analyses of tensile tests of the dog-bone and the single-edge notch specimens of the two steels are shown in Fig. 3.11. Fig. 3.11 shows the variation of the predicted area fraction of various levels of $\varepsilon_{xx}/\varepsilon_{xx}^{box}$ and ε_{xy} in the dog-bone like and the single-edge notch specimens of the two steels at a fixed overall strain, ε_{xx}^{box}. The finite element results presented in Fig. 3.11 are qualitatively similar to the experimental results presented in Fig. 3.6. Similar to experimental results in Fig. 3.6, the numerical results in Fig. 3.11 show that: (i) for both the steels, the area fraction of a given level of $\varepsilon_{xx}/\varepsilon_{xx}^{box}$ and ε_{xy} is in general greater in the single-edge notch specimen compared to the dog-bone specimen; (ii) in both the specimens the area fraction of $\varepsilon_{xx}/\varepsilon_{xx}^{box}$ and ε_{xy} is in general greater in DF140T steel compared to DP980 steel; (iii) in dog-bone specimens, the area fraction of $\varepsilon_{xx}/\varepsilon_{xx}^{box}$ and ε_{xy} decreases with increasing values of $\varepsilon_{xx}/\varepsilon_{xx}^{box}$ and ε_{xy}, respectively, for both the steels; and (iv) in single-edge notch specimens, the area fraction of $\varepsilon_{xx}/\varepsilon_{xx}^{box}$ and ε_{xy} decreases with increasing values of $\varepsilon_{xx}/\varepsilon_{xx}^{box}$ and ε_{xy}, respectively, for DP980 steel but for DF140T steel, beyond a critical value of $\varepsilon_{xx}/\varepsilon_{xx}^{box}$ and ε_{xy} their area fraction tends to saturate. The results of the microstructure-based finite element analyses confirm that the interlacing of heterogeneous deformation at the structural and the microstructural length-scales can lead to localization of deformation in the single-edge notch specimens of DF140T steel.

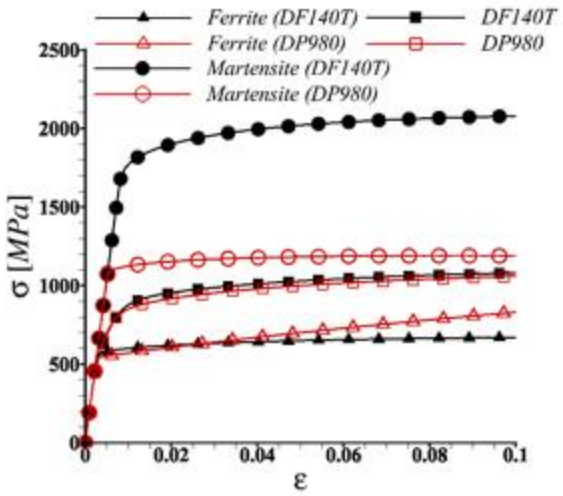

Figure 3.10. Nominal stress (σ) – strain (ε) response of the ferrite and the martensite phases present in DF140T and DP980 dual-phase advanced high strength steels, and the overall nominal stress-strain response of DF140T and DP980 dual-phase advanced high strength steels predicted using the constitutive parameters given in Table 3.1.

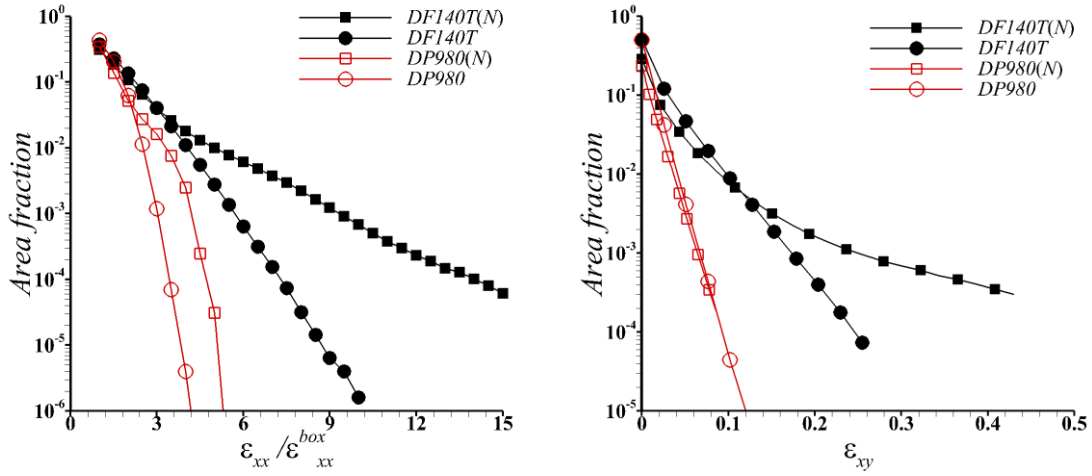

(a) (b)

Figure 3.11. The variation of the area fraction of various levels of (a) $\varepsilon_{xx}/\varepsilon_{xx}^{box}$ and (b) ε_{xy} in the defect free specimen (mimicking dog-bone specimen) and in the region marked as *abcd* in Fig. 9 near the notch in the single-edge notch tension specimen (*N*) of DF140T and DP980 steels. For both the steels, the defect free specimens were deformed to a macroscopic strain, ε_{xx}^{box}=0.04, and single-edge notch tension specimens were deformed to an overall strain, ε_{xx}^{box}=0.05, in the region marked as *abcd* in Fig. 3.9. The *y*-axes in (a) and (b) are on logarithmic scale.

The in-plane localization of deformation prior to the onset of maximum load (i.e., necking or fracture) in the single-edge notch specimen of DF140T steel, will affect the damage evolution and final failure. As shown in Fig. 3.12, in the single-edge notch specimen of DF140T steel the deformation predominantly localizes in the softer non strain-hardening ferrite phase in bands emanating from the corners of the deformed notch. These bands are inclined at angles of ~45^{o} and ~135^{o} with respect to the loading axis. With progressive deformation, damage predominantly initiates and evolves in the ferrite phase within these bands and finally a crack nucleates along one of the bands resulting in premature fracture. However, due to a lack of in-plane localization of deformation, the single-edge notch specimen of DP980 steel undergoes through thickness necking near the notch root before fracture, Fig. 3.12. Therefore, in the single-edge notch specimen of DP980 steel, damage initiates and evolves in both the phases. In the absence of a dominant structural length-scale in the dog-bone specimens, both the steels undergo necking before fracture and exhibit the same mechanical response. The same mechanical response of the dog-bone specimens of the two steels is largely due to the competing effect of the overall microstructure and the microscale properties of the constituent phases. Recall that the microstructure of DF140T contains only ~39±2% martensite compared to ~61±3% martensite in DP980, and due to the differences in their nominal chemical composition, the strength of martensite of DF140T is greater than that of DP980 while the ferrite of DP980 exhibits slightly greater strain-hardening than that of DF140T.

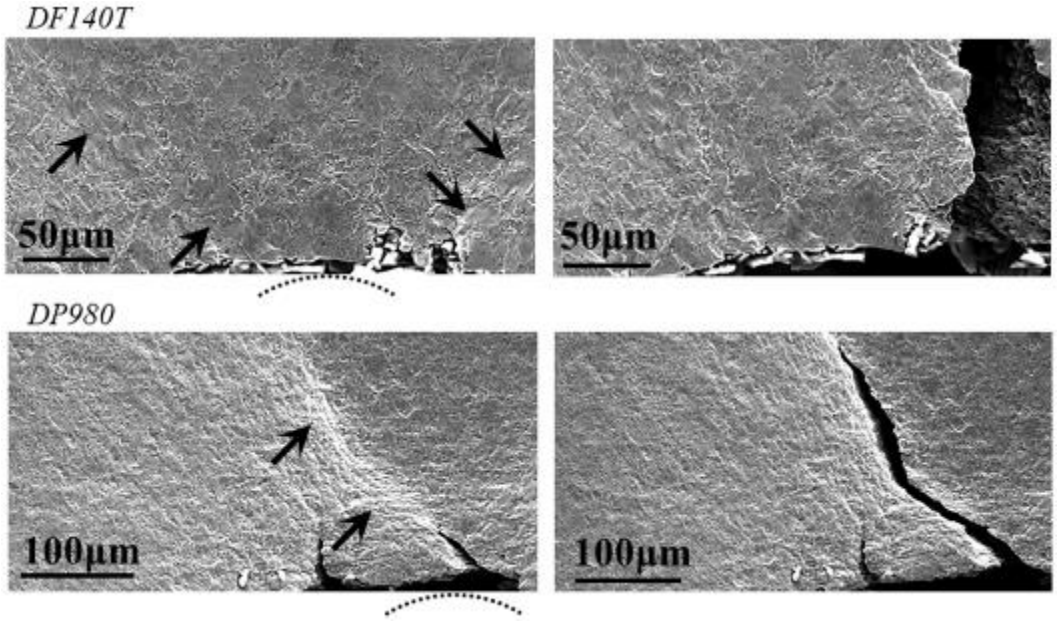

Figure 3.12. SE-SEM images of surface microstructures near the notch in the single-edge notch tension specimen of DF140T and DP980 dual-phase advanced high strength steels, just before and after fracture. For DF140T, left and right images correspond to imposed macroscale displacements of 300μm and 350μm, respectively, while for DP980, left and right images correspond to imposed macroscale displacements of 500μm and 515μm, respectively.

In other words, the differences in the microstructure and the microscale properties always lead to significantly different deformation at the microstructural length-scale in the two dual-phase steels. Nonetheless, due to the imposed homogeneous deformation field at the structural length-scale in the dog-bone tension specimens, there is a separation between the structural and the microstructural length-scales. Therefore, the mechanical response of the dog-bone tension specimens of the two steels is effectively that of an unstructured homogenized material. However, the interlacing of the heterogenous deformation field at the structural and the microstructural length-scales in the single-edge notch specimens, results in extremely localized deformation in DF140T steel. The localized deformation in DF140T steel in turn results in breakdown in scale separation

between the structural and the microstructural length-scales. Thus, the mechanical response of the single-edge notch tension specimens of dual-phase steels cannot be based on an unstructured continuum description of mechanical properties and must also involve the length-scales associated with the material microstructure.

3.5. Conclusions

It has been elucidated that how the interlacing of the structural and the microstructural length-scales affects the mechanical response of dual-phase steels. To this end, the mechanical response of the dog-bone and the single-edge notch specimens of two dual-phase steels, viz, DF140T and DP980, was characterized via *in-situ* SEM tensile tests. The microstructure of DF140T steel contains ~39±2% martensite compared to ~61±3% martensite in DP980 steel. In addition, due to the differences in their nominal chemical composition, the strength of the martensite of DF140T steel is greater than that of DP980 steel while the ferrite of DP980 exhibits slightly greater strain-hardenability than that of DF140T. The results of *in-situ* tensile tests were complemented with microstructure-based digital image correlation, fractographic analysis and microstructure-based finite element analysis. The key conclusions of this work are as follows:

1. Despite significantly different microstructure and microscale properties, the dog-bone tension specimens of the two steels exhibit very similar mechanical response (yield strength, strain-hardening, ultimate tensile strength and ductility), but the mechanical response (maximum load bearing capacity and extension to failure) of the single-edge notch tension specimens of the two steels differs significantly.

2. At the microscale, even prior to the onset of maximum load (i.e., onset of necking or fracture), the deformation in both the dog-bone and the single-edge notch tension specimens of the two steels is always heterogeneous with the extent of heterogeneous deformation being more pronounced in DF140T steel compared to DP980 steel.

3. The interlacing of the heterogenous deformation at the structural and the microstructural length-scales in the single-edge notch tension specimens of DF140T steel results in localized deformation in the softer non strain-hardening ferrite phase. Thus, with further deformation damage predominantly initiates and evolves in the ferrite phase resulting in premature fracture.

4. On the contrary, the single-edge notch tension specimens of DP980 steel undergo through thickness necking near the notch root before fracture.

5. The dog-bone tension specimens of both the steels undergo necking before fracture and their same mechanical response is due to the competing effect of the overall microstructure and the microscale properties of the constituent phases.

4. CORRELATING THE PRIOR AUSTENITE MICROSTRUCTURE AND FRACTURE OF ULTRA-HIGH STRENGTH MARTENSITIC STEELS*

4.1. Introduction

Advanced high strength steels (AHSS) are one of the most attractive materials for automotive applications as they offer a wide range of microstructures and mechanical properties [18, 19, 53]. Different AHSS are used in different parts of a vehicle to meet the diverse manufacturing and performance requirements [18, 54]. For example, the parts in the front of a vehicle usually have complex shapes and call for materials with good formability. While the need to enhance crashworthiness of a vehicle calls for materials with high strength and toughness. However, the strength-ductility (toughness) trade-off limits the strength level of AHSS that can be used in the manufacturing of complex shapes. Nevertheless, during front-impact collision of a vehicle, there is a large space for the structure to deform and absorb energy before the impact endangers passengers. On the contrary, during a side-impact collision, there is very limited space for the structure to deform. Thus, vehicle parts such as the A-pillar that supports the windshield, the B-pillar between the front and the rear doors, and the beams in the vehicle doors call for materials with ultra-high strength. Advanced low-carbon martensitic steels with strength level in excess of 1.2 GPa are the most widely sought-after structural materials for these parts to enhance the overall crashworthiness of a vehicle [55, 56].

For automotive applications, press hardening is used extensively to economically manufacture ultra-high strength martensitic steel parts. This process involves first heating the steel above the upper critical temperature (Ac3) to achieve fully austenitic

microstructure which is then followed by hot press forming to form complex shape and finally rapid quenching to achieve fully martensitic microstructure. In this process, temperature and time of heat-treatment can be varied to achieve different microstructures. In general, the heat-treatment temperature and time during this processes varies from 900^{o}C to 950^{o}C and 4 to 10 minutes, respectively [57] to obtain fully austenitic microstructure and avoid undesirable grain coarsening. The final microstructure of the material comprises lath-like martensite with a hierarchical structure consisting of laths, blocks, and packets within prior austenite grains (PAGs) [6, 58-61].

The mechanical properties of these materials are determined by the chemical composition, particularly carbon content [62-65], and by the microstructural features, such as block and packet sizes that are proportional to the PAG size [66, 67]. In general, the strength and hardness of low-carbon martensitic steels have been found to increase with decreasing PAG size [4, 5, 7, 66-71]. However, the dependence of ductility of the material on the PAG size is rather ambiguous and it does not simply follow the typical strength-ductility trade-off associated with microstructure refinement. Specifically, one study [4] has reported that the ductility of low-carbon martensitic steels decreases with decreasing PAG size (in this study PAG size varied in the range 7-17 μm), others [5, 7] have reported that it increases with decreasing PAG size (in these studies PAG size varied in the range 10-125 μm), and still others [69, 71] have reported that it is somewhat insensitive to the PAG size (in these studies PAG size varied in the range 5-35 μm). While the fracture properties, such as notch ductility as characterized by double-edge notch tension tests [4,

71] and impact toughness as characterized by Charpy impact tests [5, 7, 69, 70] have been reported to increase with decreasing PAG size for PAG size ≥ 10 μm.

There is a great interest in understanding the effect of the PAG size on the deformation and fracture response of low-carbon martensitic steels with average PAG size less than tens of microns. This is because even though the standard press hardening process qualitatively results in fine microstructures that impart ultra-high strength, technologically it is important to understand the effect of small variations in the process parameters (heat-treatment temperature and time) on the final microstructure and mechanical performance of the material. Furthermore, as noted in the preceding paragraph, the current state of understanding of the effect of the PAG size raises more questions than it answers. In particular, there are two lingering questions that need to be answered: (i) What is the effect of the PAG size on the ductility and fracture response of low-carbon martensitic steels with a very fine microstructure? (ii) If at all, why the fracture properties of low-carbon martensitic steels degrade with increasing PAG size? To answer these questions, a series of heat-treatments of a low-carbon martensitic steel have been carried out to vary the PAG microstructure in the material. The resultant microstructures are characterized by Electron Backscatter Diffraction (EBSD), which are then used to reconstruct PAGs. Next, the deformation and fracture response of all heat-treated materials are characterized by *in-situ* tension tests of dog-bone and single-edge notch specimens under a high-resolution optical microscope, allowing to capture both the macroscopic mechanical response and the distribution of microscopic strains via microscale Digital Image Correlation (DIC).

Finally, microstructure-based finite element analyses are carried out to rationalize the effect of the PAG microstructures on the mechanical response of the material.

Our results show that both the bimodality and average size of the PAGs in the low-carbon martensitic steel increases significantly with increasing heat-treatment temperature and time, for the range of temperature and time considered in this work. Despite this their yield and tensile strength levels as well as the ductility only decrease slightly with increasing average PAG size. However, the notch strength and ductility as well as the crack-tip opening displacement (CTOD) at crack growth initiation as characterized by the tension tests of the single-edge notch specimens decrease significantly with increasing average PAG size. This contrasts with any analysis based on classical engineering fracture mechanics that will predict very similar fracture response for materials that exhibit very similar stress-strain response under uniaxial tension. The results of the *in-situ* tests together with microstructure-based finite element analysis clearly elucidate that it is the interaction of the heterogeneous deformation fields induced by the notch and the bimodal PAG size distribution that leads to an increase in the propensity of shear strain localization and in turn degradation in the fracture response of the martensitic steel with increasing heat-treatment temperature and time (or average PAG size). A major conclusion derived from the results is that achieving a uniform distribution of fine grains is an effective way to increase the strength levels and enhance the fracture properties of the low-carbon martensitic steels.

4.2. Materials and Methods

The low-carbon ultra-high strength martensitic steel considered in this work is a cold rolled fully martensitic steel by ArcelorMittal with nominal chemical composition of ~0.25 wt.% Carbon, ~0.4 wt.% Silicon and ~1.4 wt% Manganese. This steel has an A_C3 temperature of 863^{o}C [71]. To understand the effect of the variability in the process parameters, the steel was subjected to five heat-treatments: 870^{o}C for 4 minutes, 870^{o}C for 10 minutes, 930^{o}C for 4 minutes, 930^{o}C for 10 minutes and 950^{o}C for 10 minutes. All heat-treatments were followed by rapid cooling to achieve fully martensitic microstructure. The deformation and fracture response of all five heat-treated materials were characterized via *in-situ* tension tests using the methodology described in **2.1** and **2.2** on the specimens with final thickness of 1.08 mm. Microscale DIC is performed using **2.3**, and the displacement fields measured by DIC were then used to estimate the Green-Lagrange strain. The microstructure characterization of the undeformed material and fractographic analysis of the fractured specimens were carried out as mentioned in **2.4**.

4.3. Results

4.3.1. Material microstructure

The EBSD inverse pole figure (IPF) maps of the low-carbon fully martensitic steel post five heat-treatments are shown in Fig. 4.1. The rolling direction is along the horizontal axis for all the IPF maps and each IPF map represents a 150×200 μm^2 area. The electron beam was scanned in steps of 0.3 μm at voltage of 20 kV; the EBSD pattern was indexed using the Fe-bcc phase. The different colors in the IPF maps represent the blocks of the martensitic microstructure. As can be seen from the IPF maps, the block size in the

microstructure increased significantly from the heat-treatment condition of 870°C for 4 min to 950°C for 10 min. For the heat-treatment conditions 870°C for 4 min and 10 min, the blocks have an equiaxed polygonal morphology while for heat-treatment conditions 930°C for 4 min and 10 min and 950°C for 10 min, the blocks tend to take a non-equiaxed morphology.

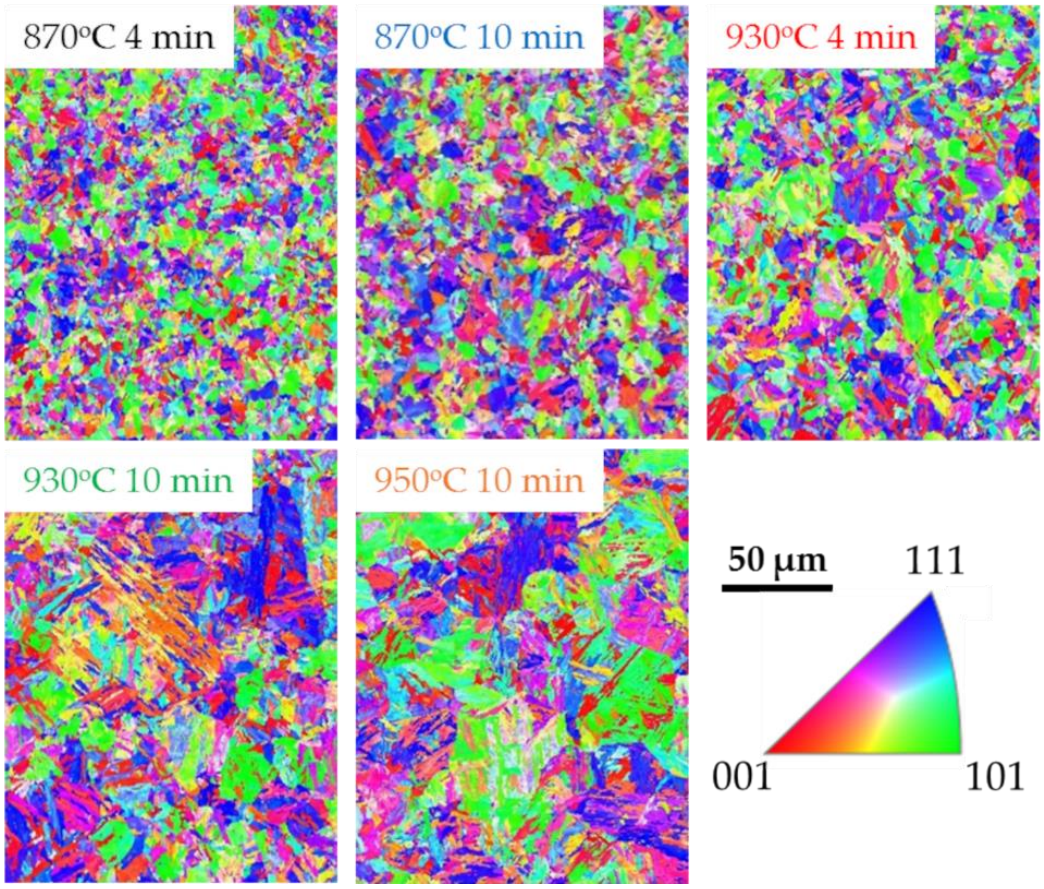

Figure 4.1. EBSD inverse pole figure maps of the low-carbon fully martensitic steel post five heat-treatments and the associated color-coded stereographic triangle.

The IPF maps of the five heat-treated materials were used to reconstruct the PAGs. The PAG reconstruction was carried out using an open source MATLAB based software, MTEX [72-74] with an interface PAG_GUI [75]. This software utilizes the Kurdjumov-

Sachs orientation relationship to reconstruct PAGs from the IPF maps of the martensitic microstructure. The reconstructed IPF maps of PAGs using the IPF maps of the five heat-treated materials shown in Fig. 4.1 are shown in Fig. 4.2. The orientation scatter of the PAGs in all five IPFs in Fig. 4.2 shows that the heat-treated materials do not possess a pronounced texture. Also, in-line with the block size, the PAG size in the microstructure (on average) increased significantly with increasing heat-treatment temperature and time. The reconstructed PAG maps also show that in all the five heat-treated steels, the PAG size is not homogeneous i.e., they contain a distribution of small and large grains.

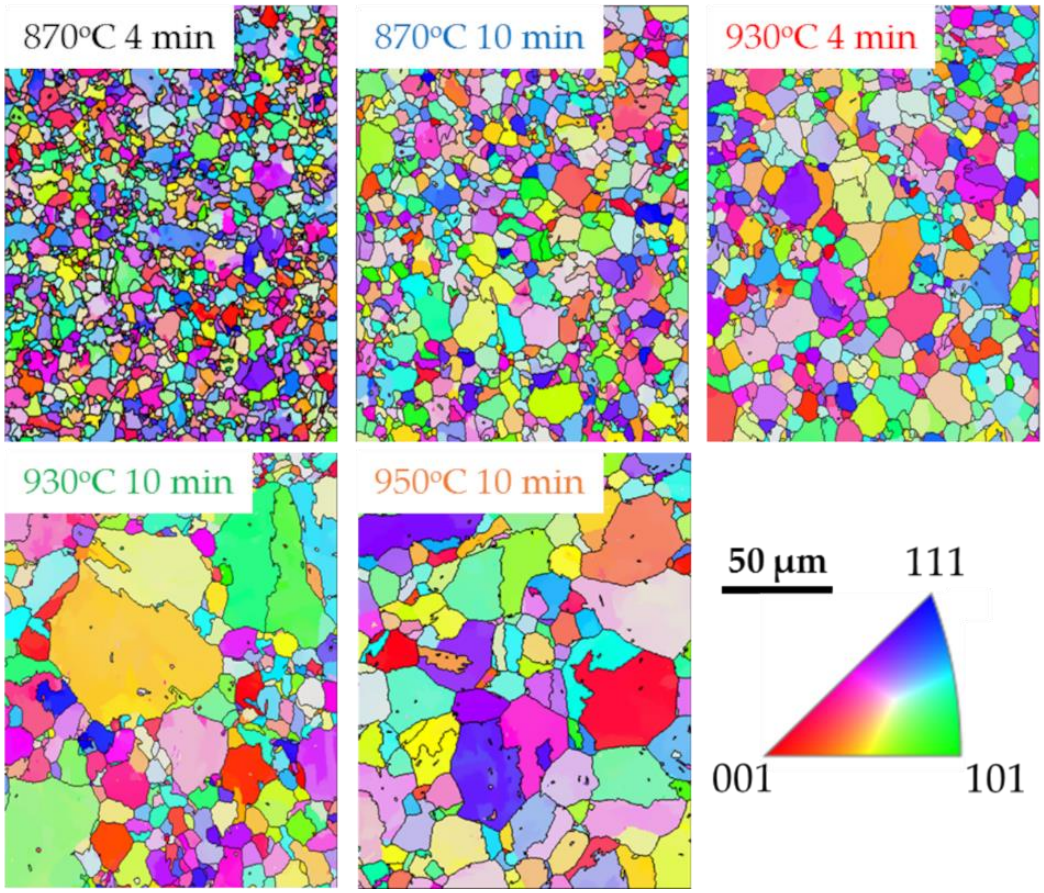

Figure 4.2. Reconstructed EBSD inverse pole figure maps of the prior austenite grains using the inverse pole figure maps of the five heat-treated martensitic steels (shown in Fig 4.1) and the associated color-coded stereographic triangle.

The PAG size in the five heat-treated materials was measured from multiple IPF maps of the reconstructed PAGs, as in Fig. 4.2, following the Heyn linear intercept procedure [76]. The descending cumulative distribution function (CDF) of the PAG size in the five heat-treated materials is shown in Fig. 4.3(a). The CDF curves represent the probability that the PAG size in a heat-treated material is greater than a given value on the *x*-axis. As shown in Fig. 4.3(a), the probability of finding PAGs greater than a given value increases significantly with increasing heat-treatment temperature and time. In other words, for a given probability, the PAG size increases significantly with the increasing heat-treatment temperature and time. The probability density plot of the PAG size in the five materials, Fig. 4.3(b), does, however, show that the PAG size follows a bimodal distribution, especially in the 930°C 10 min and 950°C 10 min heat-treated materials. The bimodal distribution of the PAG size in the materials can be represented as a sum of two normal distributions:

$$f_{mix}(x) = p \times \frac{1}{\sigma_1\sqrt{2\pi}} e^{-\frac{1}{2}\left(\frac{x-\mu_1}{\sigma_1}\right)^2} + (1-p) \times \frac{1}{\sigma_2\sqrt{2\pi}} e^{-\frac{1}{2}\left(\frac{x-\mu_2}{\sigma_2}\right)^2}, \quad (4.1)$$

where p is the fraction, μ_i are the mean and σ_i are the standard deviation of the two normal distributions. The parameters of the bimodal fit to the probability density plots of PAG size in the five materials are given in Table 1. It can be noted from the data in Table 1 that not only both μ_1 and μ_2 but their difference also increases with the increasing heat-treatment temperature and time suggesting an increase in the bimodality of the PAG size consistent with the reconstructed PAG maps shown in Fig. 4.2.

Table 4.1. Parameters of the bimodal fit (Equation 4.1) to the probability density plots of the five heat-treated materials shown in Fig. 4.3 (b).

Heat-treatment conditions	p	μ_1	μ_2	σ_1	σ_2
870°C 4 min	0.7	2.9	7.3	1.4	3.4
870°C 10 min	0.6	3.6	8.4	1.8	3.7
930°C 4 min	0.6	4.2	10.0	2.1	4.6
930°C 10 min	0.8	6.2	20.3	3.5	13.4
950°C 10 min	0.5	6.5	18.8	3.2	9.5

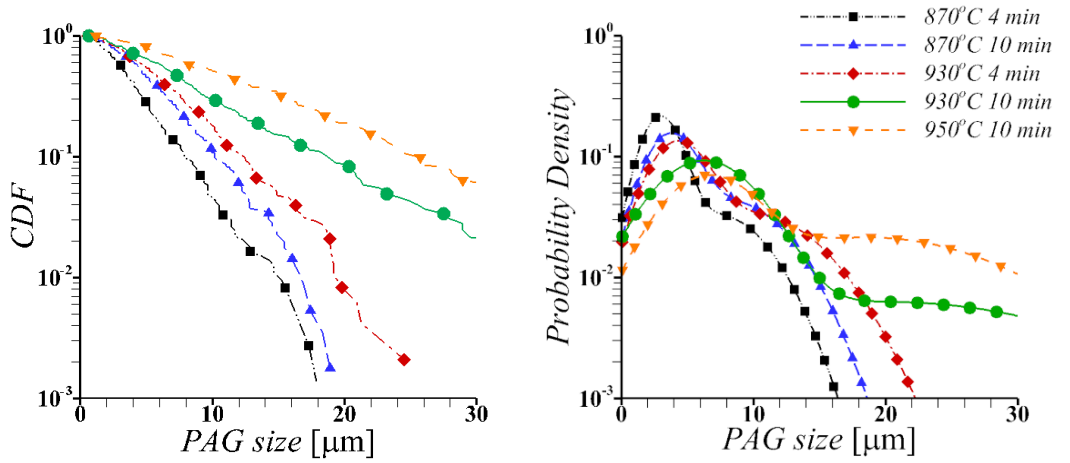

(a) (b)

Figure 4.3. (a) The descending cumulative distribution function (CDF) and (b) the probability density function of the prior austenite grain (PAG) size in the low-carbon fully martensitic steel post five heat-treatments.

4.3.2. Mechanical response

A comparison of the engineering stress (σ_{eng}) – strain (ε_{eng}) response obtained from the tension tests of the dog-bone specimens of the five heat-treated materials is shown in Fig. 4.4(a); while Fig. 4.4(b) compares the evolution of the true stress (σ) normalized strain-hardening rate, $1/\sigma$ ($d\sigma/d\varepsilon_p$), as a function of the true plastic strain

(ε_p). As can be seen from the figures, qualitatively the tensile flow response of all five heat-treated materials is the same. The tensile flow response of all the materials exhibits an elastic response until the onset of yielding, which is followed by strain-hardening up until $\varepsilon_{eng} \approx 0.05$ at which point $1/\sigma\ (d\sigma/d\varepsilon_p) \rightarrow 1$ and necking ensues. Post-necking, the load-bearing capacity of all five materials decreases rather gradually up until final fracture.

Although, the PAG size in the five materials follows a bimodal distribution, for the purpose of comparison, here define a weighted average PAG size, d_G, which is approximately 4 μm, 5.5 μm, 6.5 μm, 9 μm and 13 μm in the five heat-treated materials, 870°C for 4 minutes, 870°C for 10 minutes, 930°C for 4 minutes, 930°C for 10 minutes and 950°C for 10 minutes, respectively. Next, the variation of the yield and tensile strengths and that of the plastic strain to failure with d_G are shown in Fig. 4.4(c), (d). The error bars in Fig. 4.4(c), (d) are plus/minus one standard error. As shown in the figures, the yield and tensile strengths as well as the tensile ductility of the material increase slightly with decreasing d_G. On average a decrease in the value of d_G from 13 μm to 4 μm results in approximately a 5% increase in yield strength, 4% increase in tensile strength, and 5% increase in tensile ductility.

The curves of the tensile force, F, normalized by the minimum cross-sectional area, A_0^{min}, and the extension, δ, normalized by the initial gauge length, L_0, of the single-edge notch specimens, Fig. 4.5(a), of the five heat-treated materials are compared in Fig. 4.5(b). As shown in Fig. 4.5(b), the linear portion of the normalized force-displacement curves of the single-edge notch specimens is independent of the heat-treatment condition

while the onset of the non-linearity and the maximum load bearing capacity (maximum force) depend on the heat-treatment condition. The variation of the normalized maximum force, F^{max}/A_0^{min}, and that of the normalized maximum extension, δ^{max}/L_0, with d_G are shown in Fig. 4.5(c), (d). The error bars in the figures are plus/minus one standard error. As shown in the figures, the values of both F^{max}/A_0^{min} and δ^{max}/L_0 increase with decreasing d_G. On average a decrease in the value of d_G from 13 μm to 4 μm results in approximately 8% increase in the notch strength i.e., F^{max}/A_0^{min}, and a 16% increase in the notch ductility i.e., δ^{max}/L_0.

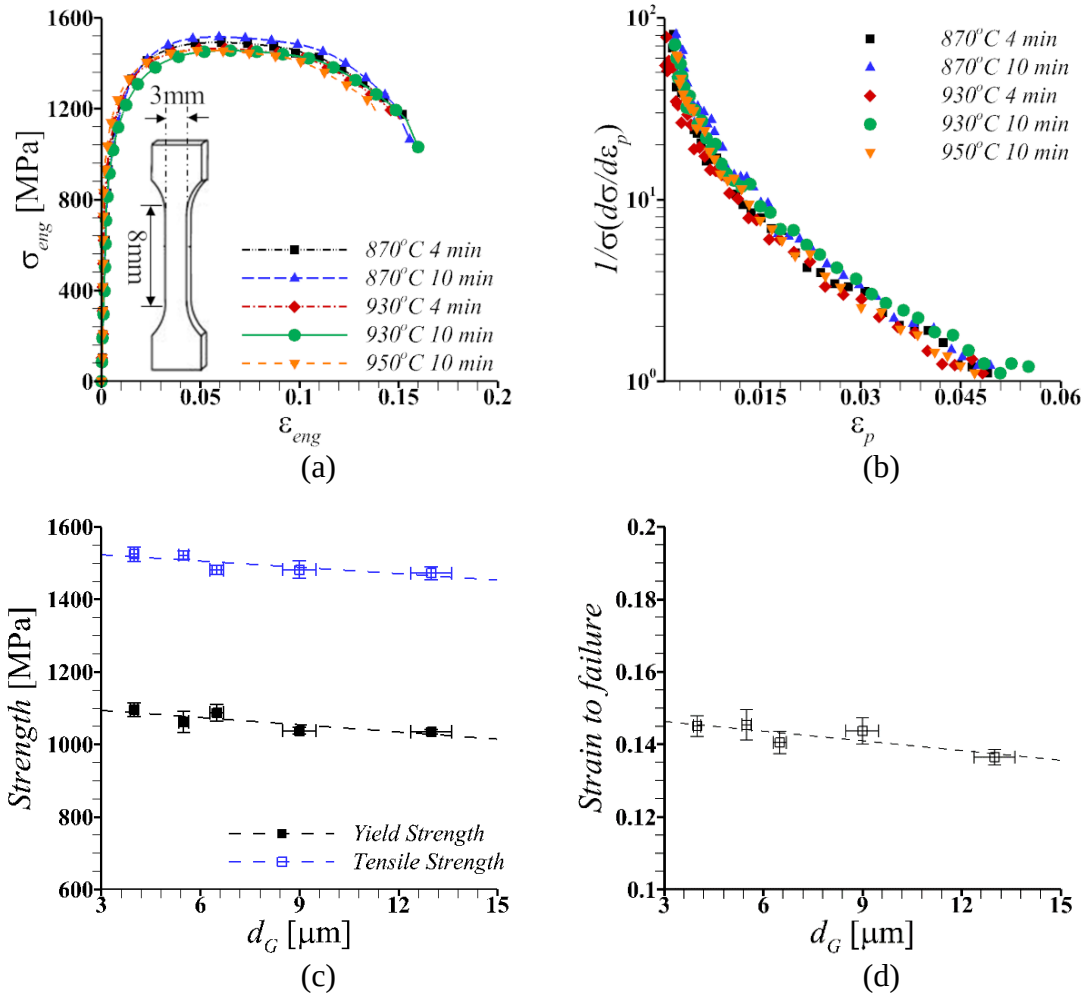

Figure 4.4. (a) Engineering stress-strain (σ_{eng}–ε_{eng}) response and (b) evolution of the true stress (σ) normalized strain-hardening rate, $1/\sigma\ (d\sigma/d\varepsilon_p)$, with true plastic strain, ε_p, obtained from the dog-bone specimens of the five heat-treated martensitic steels. (c) Variation of the yield and tensile strengths and that of the (d) plastic strain to failure with average prior austenite grain size, d_G, in the five materials.

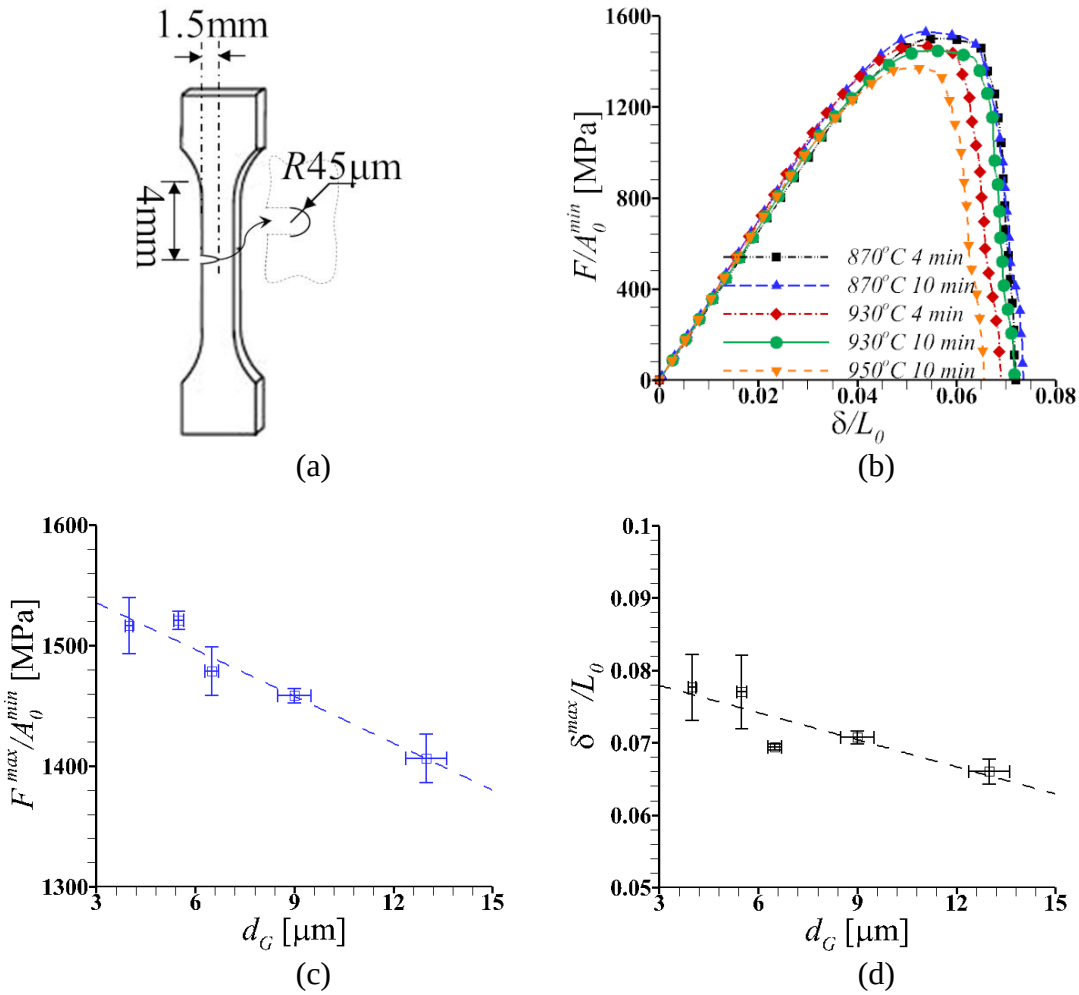

Figure 4.5. (a) Schematic of the single-edge notch specimen. (b) Normalized force-extension curves (Force, F, is normalized by the minimum cross-sectional area, A_0^{min}, and extension, δ, is normalized by the initial gauge length, L_0) of the five heat-treated martensitic steels. (c) Variation of the normalized maximum force, F/A_0^{min}, and that of the (d) normalized maximum extension, δ^{max}/L_0, with average prior austenite grain size, d_G, in the five materials.

A series of optical images captured during the *in-situ* tension tests of the single-edge notch specimens were used to extract crack-tip opening displacement, Δ. The crack-tip opening displacement is an effective parameter to characterize the extent of local deformation at the notch root [77-79]. The value of Δ is defined as the distance between

the intercepts of two orthogonal lines originating from the notch tip and the opposite sides of the notch, as shown schematically in Fig. 4.6(a). The critical value of Δ at the crack growth initiation, Δ_c, was estimated as follows. First, the value of δ/L_0 at which crack growth ensues, δ_c/L_0, was identified from the force-displacement curve, Fig. 4.5(b), as the point at which the load bearing capacity of the specimen decreases rapidly. This was confirmed by visual inspection during the *in-situ* tension tests. Second, the value of Δ_c was obtained from the Δ versus δ/L_0 curve as the value of Δ at δ_c/L_0 by exponential interpolation. The variation of the normalized critical crack-tip opening displacement, $\Delta_c^n = (\Delta_c - \Delta_0)/\Delta_0$, where Δ_0 is the initial crack-tip opening, with d_G is shown in Fig. 4.6(b). The error bars in the figure are plus/minus one standard error. As shown in Fig. 4.6(b), the value of Δ_c^n increases significantly with decreasing d_G. On average, a decrease in the value of d_G from 13 μm to 4 μm results in approximately 36% increase in the value of Δ_c^n.

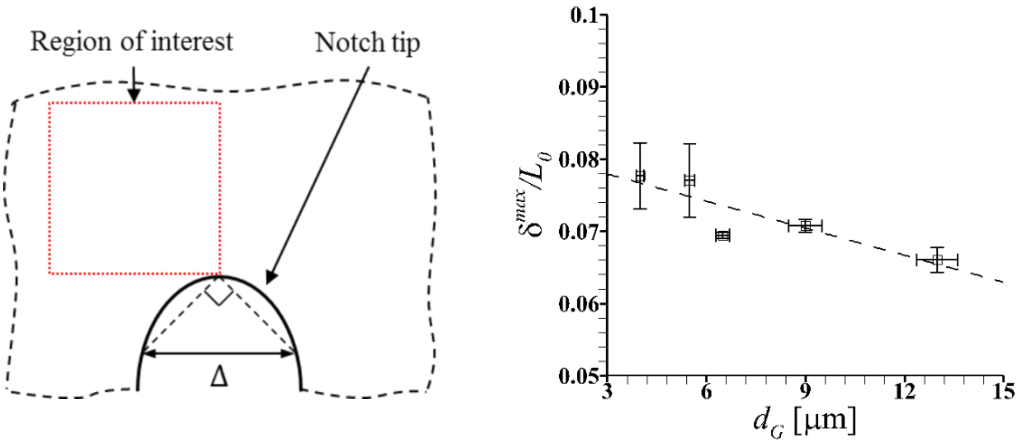

(a) (b)

Figure 4.6. (a) Schematic showing a magnified view of the notch in a single-edge notch specimen and the definition of the crack-tip opening displacement, *Δ*. (b) Variation of the normalized critical crack-tip opening displacement, Δ_c^n with average prior austenite grain size, d_G.

4.3.3. Microscale deformation characteristics

The series of high-resolution optical images of the polished surface (decorated with a fine dispersion of 1 μm polycrystalline diamond particles) of all the specimens captured at regular intervals throughout the tensile deformation were also used to characterize the in-plane microscale strain fields via DIC. The distribution of the microscale strain along the tensile loading direction, ε_{xx}, in the reference configuration in a 270-by-270 μm^2 region in the center of the gauge section of the dog-bone specimens of the five heat-treated materials deformed to a macroscopic tensile strain of 0.048 ± 0.004 is shown in Fig. 4.7. As can be seen in Fig. 4.4(a), at this macroscopic tensile strain level, all the five materials are undergoing uniform deformation i.e., necking has not occurred yet. In Fig. 4.7, the values of ε_{xx} less than the average value of ε_{xx} in the region of interest, ε_{xx}^{b}, are whitewashed to highlight the regions of strain concentration or hot spots. As shown in the figure, the distribution of ε_{xx} at the microscale is heterogeneous and the extent of this heterogeneity increases with increasing heat-treatment temperature and time, even though all the specimens are undergoing homogeneous deformation at the macroscale. For instance, notice the increase in the size of the strain hot spots i.e., regions with the values of $\varepsilon_{xx} > 1.2\varepsilon_{xx}^{b}$ with increasing heat-treatment parameters. Despite the increase in the size of the strain hot-spots, their overall area fraction is not very sensitive to heat-treatment parameters. This is because the number of strain hot spots decreases with increasing heat-treatment temperature and time.

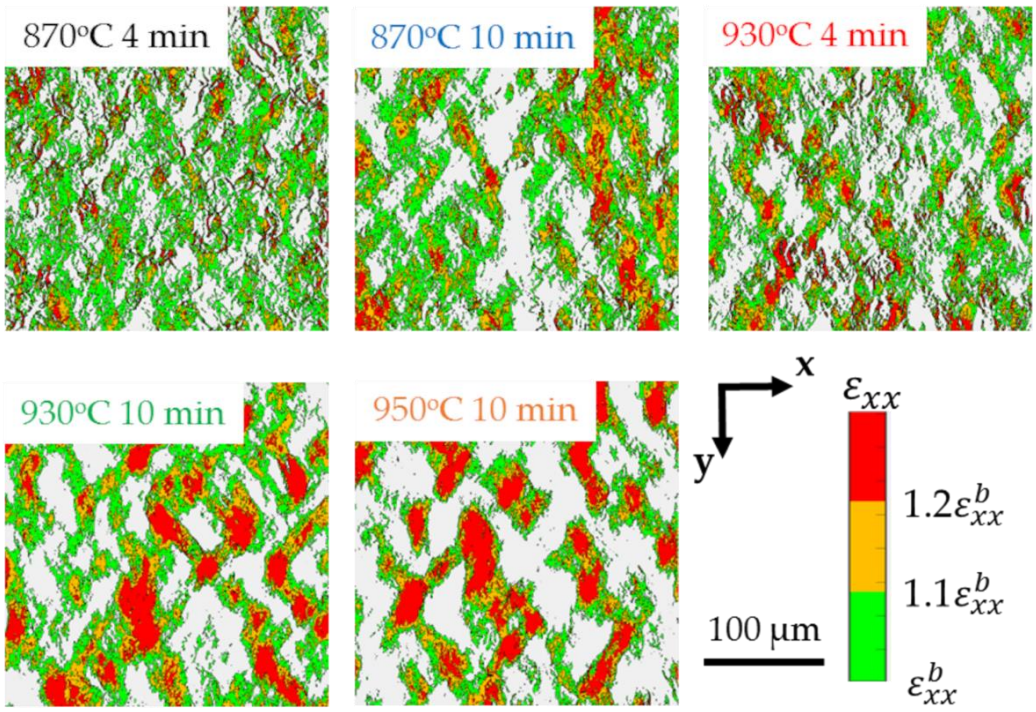

Figure 4.7. The distribution of the axial strain, ε_{xx}, in a 270-by-270 μm^2 region in the center of the gauge section of the dog-bone specimens of the five martensitic steels deformed to a macroscopic tensile strain of 0.048±0.004. The loading direction is along the *x*-axis.

Similarly, the distribution of the ε_{xx} in the reference configuration in a 135-by-135 μm^2 region close to the notch (marked in Fig 4.6(a) as 'region of interest') in the single-edge notch specimens of the five heat-treated materials deformed to a macroscopic normalized extension, δ/L_0, of 0.05±0.003 is shown in Fig. 4.8. As can be seen in Fig. 4.5(b), at this macroscopic deformation level none of the single-edge notch specimens have reached the maximum force, F^{max}. In Fig. 4.8, the values of ε_{xx} less than the average value of ε_{xx} in the region of interest, ε_{xx}^{b}, are whitewashed to highlight the regions of strain concentration or hot spots. As shown in the figure, in the single-edge notch specimens of all five materials, ε_{xx} concentrates in wide bands that emanate from the

corners of the deformed notch and are inclined at ≈ 45° with respect to the loading axis. The distribution of ε_{xx} within these bands is heterogeneous but there is no obvious correlation between heat-treatment parameters and the extent of heterogeneity. This is despite the observations made in Figs. 4.5 and 4.6 that the macroscopic mechanical response and the value of the crack-tip opening displacement at the crack growth initiation of the single-edge notch specimens of the five materials significantly depend on the heat-treatment condition (or d_G).

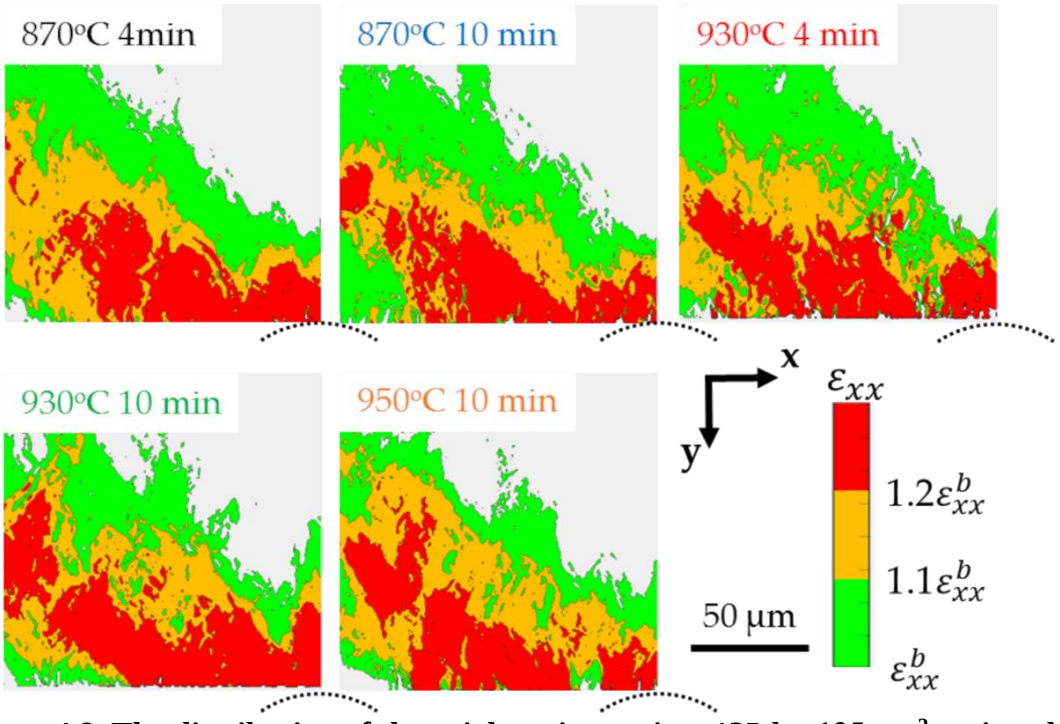

Figure 4.8. The distribution of the axial strain, ε_{xx}, in a 135-by-135 µm^2 region close to the notch (marked in Fig. 4.6 (a) as 'region of interest') in the single-edge notch specimens of the five martensitic steels deformed to a macroscopic normalized extension, δ/L_0, of 0.05±0.003. The loading direction is along the *x*-axis and the dotted arcs mark the initial location of the notch tip.

To further understand the effect of the heat-treatment parameters on the microscale deformation characteristics that in-turn affects the macroscopic mechanical response of

the single-edge notch specimens of the five heat-treated materials, here analyze the distribution of the shear strain, ε_{xy}, close to the notch. The distribution of the ε_{xy} in the reference configuration in a 135-by-135 μm^2 region close to the notch (marked in Fig. 4.6(a) as 'region of interest') in the single-edge notch specimens of the five materials deformed to a macroscopic normalized extension, δ/L_0, of 0.05 ± 0.003 is shown in Fig. 4.9. As shown in the figure, in the single-edge notch specimens of all the five materials, the positive values of ε_{xy} concentrate in triangular bands originating from the notch tip, while the values of ε_{xy} are negative on the left side of these triangular bands. The distribution of ε_{xy} within these triangular bands is heterogeneous and the extent of heterogeneity or the size of the shear strain hot spots (regions with the values of $\varepsilon_{xy} > 0.018$) increases with increasing heat-treatment temperature and time. Also, unlike the distribution of ε_{xx} shown in Fig 4.8, the overall area fraction of ε_{xy} hot spots increase with increasing heat-treatment parameter suggesting an increase in the propensity of shear strain localization.

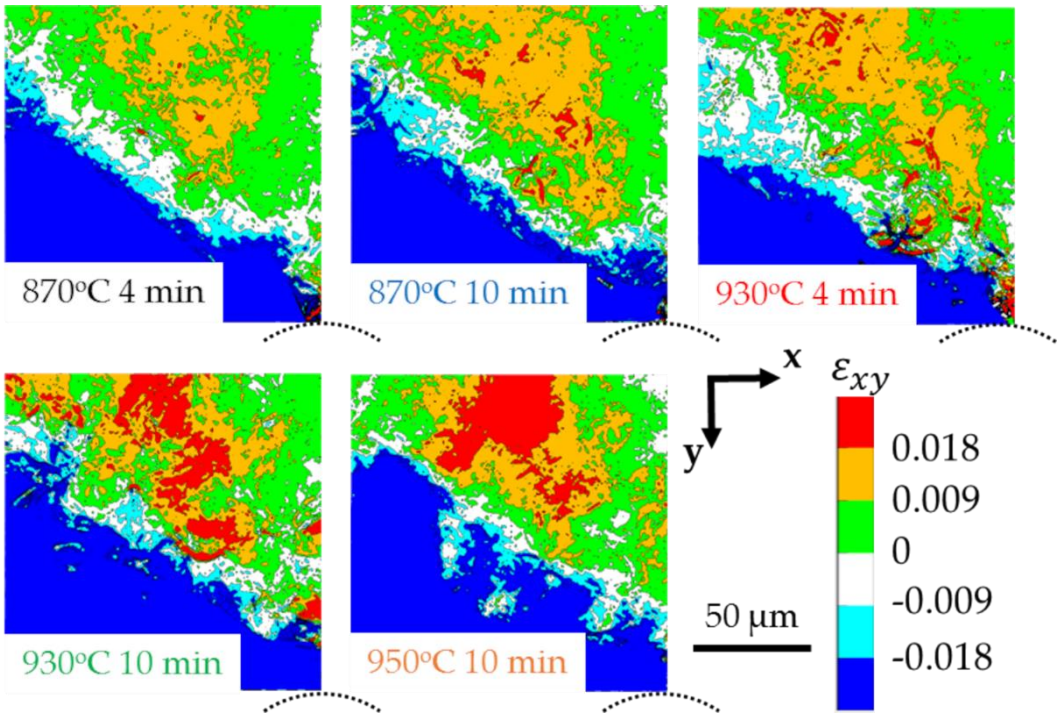

Figure 4.9. The distribution of the shear strain, ε_{xy}, in a 135-by-135 μm^2 region close to the notch (marked in Fig. 4.6 (a) as 'region of interest') in the single-edge notch specimens of the five martensitic steels deformed to a macroscopic normalized extension, δ/L_0, of 0.05±0.003. The loading direction is along the *x*-axis and the dotted arcs mark the initial location of the notch tip.

4.3.4. Fracture characteristics

SE-SEM images showing the fracture surface morphology of the dog-bone specimens of the five heat-treated materials are shown in Fig. 4.10. The images shown were taken from the center of the fracture surface of the specimens, however, it can be note that the fracture surface morphology throughout the fracture surface was roughly the same. Also, as shown in Fig. 4.10, the fracture surface morphology of the dog-bone specimens of all five heat-treated materials is qualitatively the same. The fracture surface of all the five materials exhibits a dimpled morphology indicative of ductile fracture due to nucleation, growth, and coalescence of microscale voids.

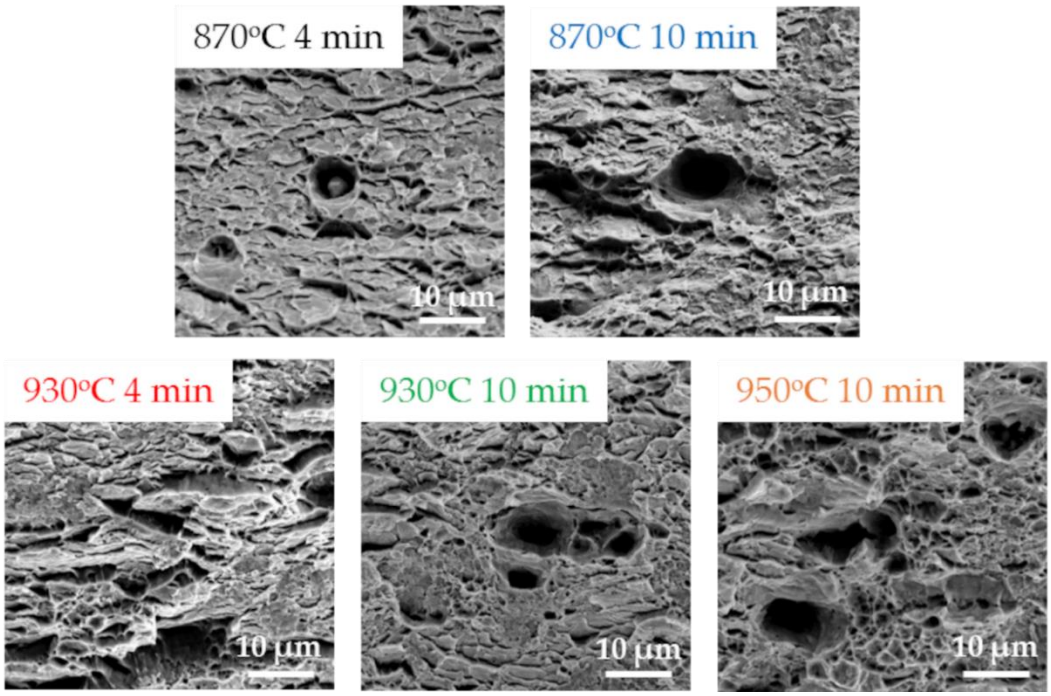

Figure 4.10. SE-SEM images taken from the center of the fracture surface of the dog-bone specimens of the five martensitic steels. The loading direction is into the viewed plane.

The fracture surface morphology of the single-edge notch specimens of all five heat-treated materials is also qualitatively the same. The fracture surface of the single-edge notch specimens of all five materials exhibits thumbnail shaped regions close to the root of the initial notch. Also, for all five materials, the fracture surface morphology inside this thumbnail shaped region is slightly different compared to the morphology outside of this region. SE-SEM images of the fracture surface of the single-edge notch specimens of the five materials inside the thumbnail shaped region close to the initial notch tip and outside this region are shown in Figs. 4.11 and 4.12, respectively. As shown in Fig. 4.11, the fracture surface of all the five materials inside the thumbnail shaped region exhibits a dimpled morphology which is indicative of ductile fracture due to nucleation, growth, and

coalescence of microscale voids. While as shown in Fig. 4.12, the fracture surface of all the five materials outside the thumbnail shaped region exhibits both dimples and quasi-cleavage like planes.

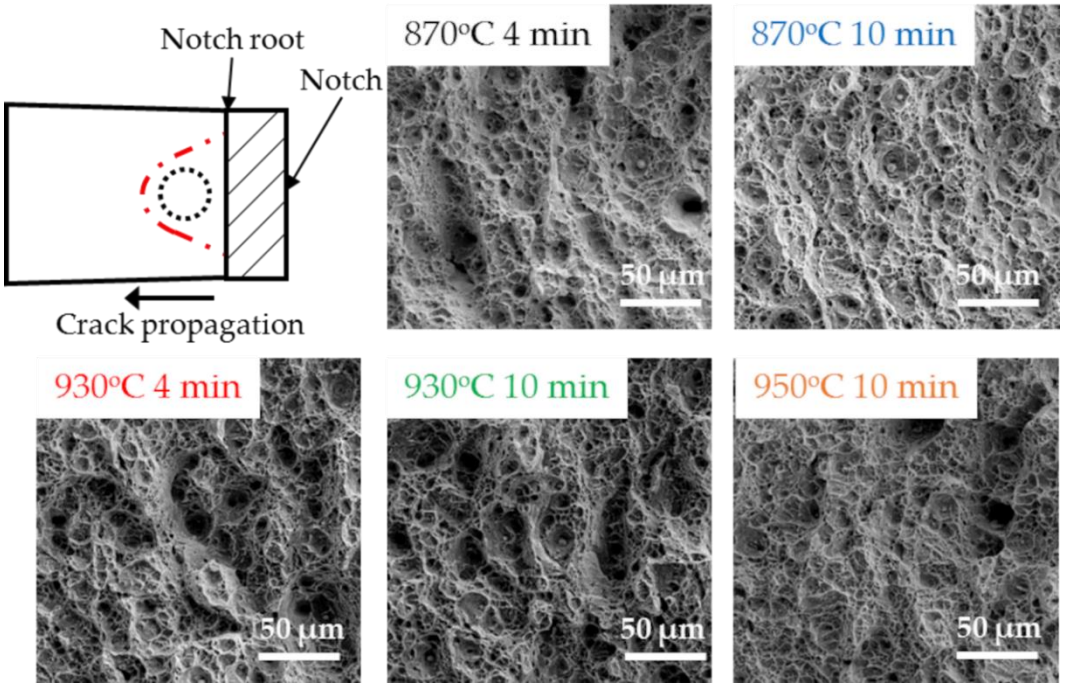

Figure 4.11. SE-SEM images taken from a location that lies within the thumbnail shaped region on the fracture surface near the initial notch root of the single-edge notch specimens (as shown in the schematic) of the five martensitic steels. The loading direction is into the viewed plane.

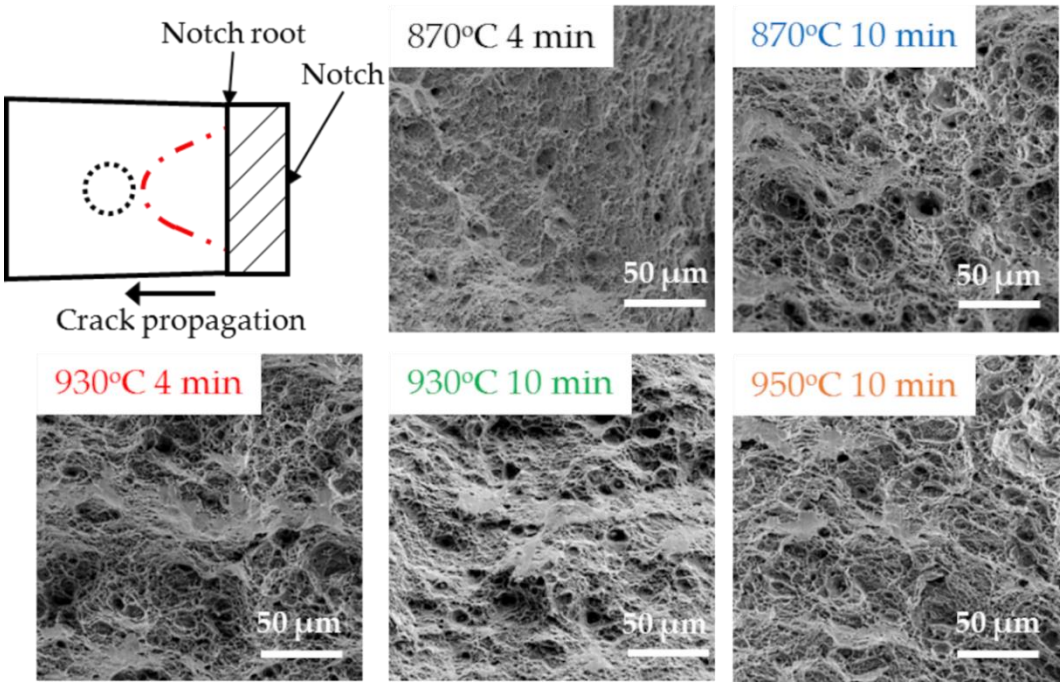

Figure 4.12. SE-SEM images taken from a location that lies outside the thumbnail shaped region on the fracture surface near the initial notch root of the single-edge notch specimens (as shown in the schematic) of the five martensitic steels. The loading direction is into the viewed plane.

4.4. Discussion

Our results show that both the average size and bimodality (distribution of small and large grains) of the PAGs in the low-carbon martensitic steel increase significantly with increasing heat-treatment temperature and time, for the range of temperature and time considered in this work. Nevertheless, the yield and tensile strengths, and ductility of the heat-treated materials as characterized by the tension test of the dog-bone specimens only decrease slightly with increasing average PAG size, d_G. While, the notch strength and ductility, and the crack-tip opening displacement at crack growth initiation as characterized by the tension test of the single-edge notch specimens decrease significantly with increasing d_G. This contrasts with any analysis based on classical engineering

fracture mechanics that will predict very similar fracture response for materials that exhibit very similar stress-strain response under uniaxial tension, as is the case for the heat-treated martensitic steels considered here.

The microscale strain measurements show that in the single-edge notch specimens of the heat-treated martensitic steels there is an increase in the propensity of shear strain localization with increasing heat-treatment temperature and time. A quantitative representation of the shear strain, ε_{xy}, localization in the single-edge notch specimens of the five heat-treated materials is shown in Fig. 4.13. In Fig. 4.13, the variation of the area fraction of various levels of ε_{xy} in the region shown in Fig. 4.9 is plotted and at the same imposed macroscopic extension. The plot in Fig. 4.13 basically shows the fraction of area in the ε_{xy} contour plots in Fig 4.9 with the value of ε_{xy} being greater than a given value of ε_{xy} on the x-axis. As shown in the figure, the area fraction of ε_{xy} greater than a given value decreases with increasing value of ε_{xy} irrespective of the heat-treatment condition. However, the rate of decease of the area fraction with increasing value of ε_{xy} decreases with increasing heat -treatment temperature and time for $\varepsilon_{xy} > 0.005$. This analysis quantitatively confirms the increase in the propensity of shear strain localization with increasing heat-treatment temperature and time (or simply d_G) in the martensitic steel. The increase in the propensity of shear strain localization with increasing heat-treatment temperature and time also qualitatively rationalizes the presence of both dimples and quasi-cleavage like planes on the fracture surfaces of single-edge notch specimens of the heat-treated materials.

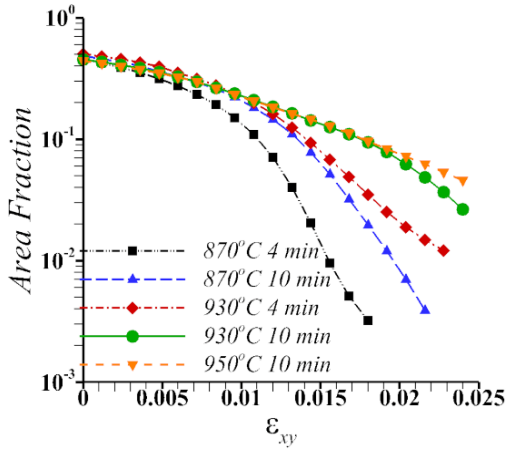

Figure 4.13. Variation of the area fraction of various levels of the shear strain, ε_{xy}, in 135-by-135 μm^2 region close to the notch in the single-edge notch specimens of the five martensitic steels deformed to a macroscopic normalized extension, δ/L_0, of 0.05±0.003.

The hypothesis that the increase in the propensity of shear strain localization in the single-edge notch specimens of the material is due to the increase in the bimodality and average size of the PAGs in the material microstructure with increasing heat-treatment temperature and time is made. To proof this hypothesis, microstructure-based finite element analysis of single-edge notch specimens of materials with bimodal distributions of grain size is also carried out. Schematic of the finite element model of one half of a two-dimensional plane strain single-edge notch specimen with a zoomed-in view of a unimodal and bimodal microstructure close to the notch tip is shown in Fig. 4.14(a). The specimen modeled has the same gauge length and notch dimensions as in the experiments and is subjected to x-axis symmetry boundary conditions along the plane of symmetry of the notch and x-axis velocity on the free surface normal to the axis of the specimen. All the finite element analyses are carried out using a commercial finite element code, ABAQUS/Standard [80]. The finite element meshes use eight-node plane strain, CPE8R,

elements of the ABAQUS/Standard element library. A 200-by-200 μm^2 region close to the notch tip contains 400-by-400 elements and a rather coarse mesh is used outside this region. Next, a bimodal distribution of grain microstructures with grain sizes 2 ± 0.2 μm and 50 ± 5 μm is generated in the 200-by-200 μm^2 fine mesh region close to the notch tip using Voronoi tessellations. Specifically, five grain microstructures with percentage of 2 ± 0.2 μm grain size as 100%, 80%, 70%, 60% and 50% are considered. These five microstructures are referred to as unimodal, 80-20 bimodal, 70-30 bimodal, 60-40 bimodal and 50-50 bimodal, respectively. In the calculations, all grains in the material microstructure are modeled as rate-independent isotropic elastic-plastic material within finite strain J_2 flow theory. The Young's modulus and Poisson's ratio of the material is taken to be 210 GPa and 0.3, respectively. The plastic response of a grain of size d_G is modeled using the constitutive relation,

$$\sigma = \sigma_0 + A(d_G)^{-\frac{1}{2}} + B\varepsilon_{pl}^{n} \tag{4.2}$$

where σ_0 =949 MPa, A =296 MPa·μm^2, B =1938 MPa and n =0.41 are obtained from the experimentally measured dependence of yield strength on d_G, Fig. 4.4(c), and average strain-hardenability of the material, Fig. 4.4(a). Note that inside the 200-by-200 μm^2 fine mesh region area where the grains are discretely modeled, d_G is the size of the grain while outside this region, d_G is simple the average grain size.

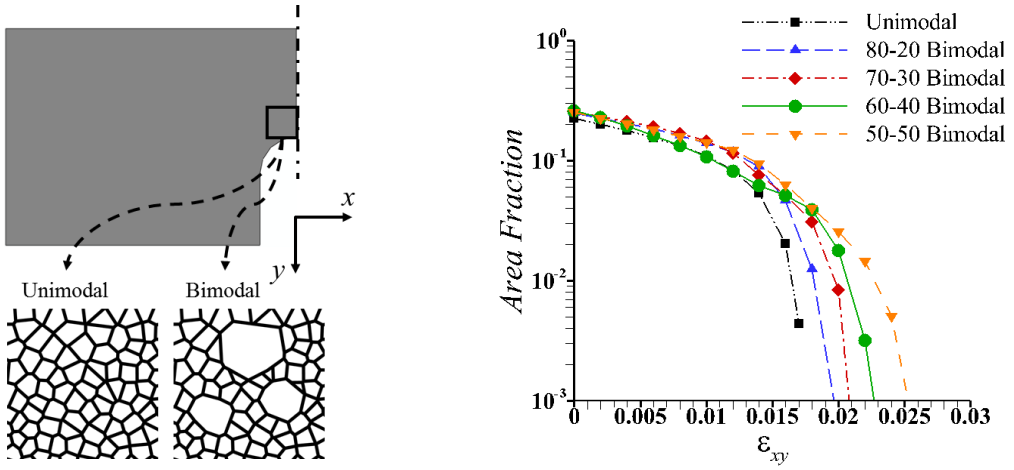

(a) (b)

Figure 4.14. (a) Schematic showing the finite element model of one-half of the single-edge specimen together with zoomed-in view of a unimodal and bimodal grain microstructure close to notch tip. (b) Variation of the area fraction of various levels of the shear strain, ε_{xy}, in 200-by-200 μm^2 region close to the notch in a unimodal and four bimodal microstructures deformed to a macroscopic normalized extension, δ/L_0, of 0.015.

A quantitative representation of the shear strain, ε_{xy}, localization in the five finite element models is shown in Fig. 4.14(b). The figure shows the variation of the area fraction of various levels of ε_{xy} in the 200-by-200 μm^2 region close to notch tip at the same macroscopic extension. As be seen in the figure the area fraction of ε_{xy} greater than a given value decreases with increasing value of ε_{xy} irrespective of the extent of the bimodal grain distribution in the microstructure. However, the rate of the decease of the area fraction with increasing value of ε_{xy} decreases with increasing percentage of large grains for $\varepsilon_{xy} > 0.015$. The results presented in Fig. 4.14(b) proofs the hypothesis that the propensity of shear strain localization in the single-edge notch specimens increases with an increase in the bimodality and average size of the PAGs in the material microstructure.

In summary, it has been shown that even though the uniaxial stress-strain response of the low-carbon martensitic steel is not very sensitive to the variation in the heat-treatment conditions, their fracture response differ significantly. This is like dual-phase steels, for which it has been shown that the interaction of the heterogeneous deformation fields induced by the geometry of deformation i.e., the presence of a notch in the single-edge notch specimens or three-point bending and the material microstructure i.e., distribution of a hard (martensite) and soft (ferrite) phase leads to an increase in the propensity of deformation localization that significantly affects the fracture response of these materials [81-83]. Although, the low-carbon martensitic steel considered in this work is a single-phase material, their microstructure comprises a bimodal distribution of grains (i.e., PAG). Furthermore, the average size and the bimodality of the PAG distribution in the material increase with increasing heat-treatment temperature and time. The results of the *in-situ* tests together with microstructure-based finite element analysis clearly elucidate that it is the interaction of the heterogeneous deformation fields induced by the notch and the bimodal PAG size distribution that leads to an increase in the propensity of shear strain localization and in turn degradation in the fracture response of the martensitic steel with increasing heat-treatment temperature and time.

4.5. Conclusions

In this work, the effect of small variations in the heat-treatment conditions on the microstructure and the deformation and fracture response of an ultra-high strength low-carbon martensitic steel have been quantified. To this end, the material of interest was subjected to five heat-treatments and the prior austenite grain (PAG) microstructure in the

resultant microstructures was characterized by reconstructing PAGs from the EBSD IPF maps of the martensitic microstructure. Next, the deformation and fracture response of all heat-treated materials were characterized by *in-situ* tension tests of dog-bone and single-edge notch specimens under a high-resolution optical microscope, allowing to capture both the macroscopic mechanical response and the distribution of microscopic strains via microscale DIC. The *in-situ* tension tests were also complemented with fractographic and microstructure-based finite element analyses. The key findings and conclusions of this work are:

1. The average size and bimodality (distribution of small and large grains) of the PAG distribution in the low-carbon martensitic steel increase with increasing heat-treatment temperature and time.

2. The yield and tensile strengths, and ductility of the martensitic steel (as characterized by the tension tests of the dog-bone specimens) only decrease slightly with increasing heat-treatment temperature and time (or average PAG size). However, due to the interaction of the heterogeneous deformation fields induced by the material microstructure (bimodal PAG size distribution) and the geometry of deformation (single-edge notch specimen), the fracture properties of the material (notch strength and ductility, and the crack-tip opening displacement at crack growth initiation) decrease significantly with increasing PAG heat-treatment temperature and time (or average PAG size).

3. The interaction of the heterogeneous deformation fields induced by the bimodal material microstructure and the geometry of deformation (single-edge notch specimen) leads to an increase in the propensity of shear strain localization which in turn gives rise

to the strong dependence of the fracture properties of the martensitic steel on the average PAG size.

4. The final fracture of the dog-bone specimens of the heat-treated martensitic steel occurs by void nucleation, growth, and coalescence for the range of heat-treatment parameters considered. However, the fracture surfaces of the single-edge notch specimens of the material exhibit both dimples and quasi-cleavage like planes.

5. Achieving a uniform distribution of fine grains is an effective way to increase the strength levels and enhance the fracture properties of the low-carbon martensitic steels.

5. INTERACTION OF DEFORMATION-INDUCED TWINNING AND CRACK GROWTH IN SINGLE CRYSTALS OF A MANGANESE STEEL

5.1. Introduction

Single phase austenitic steels with 11-15 wt% manganese exhibit extremely high strain-hardening rate that endows these steels with high ductility, toughness, and wear resistance [84-87]. These steels are widely used in railroad applications and in heavy machineries to meet the need of high wear resistance and impact strength. The high strain-hardening rate in this class of material is associated with deformation-induced twinning [8-10, 88-101]. The activation of twinning in these materials have been widely studied by mechanical testing of both polycrystalline [88-95] and single crystal specimens [8-10, 96-101]. Majority of these single crystal level studies used carefully grown single crystals of austenitic manganese steels widely referred to as Hadfield steel [8, 9, 97, 98]. The work on single crystal specimens is particularly important since it is very challenging to deconvolute the effect of twining on the mechanical response of a material by testing their polycrystalline aggregates. This is largely due to the simultaneous activation of crystallographic slip and twining in different grains within a polycrystalline material [88-93].

The mechanical testing of single crystal specimens of Hadfield steel has been carried out under uniaxial tension along various crystallographic orientations, such as $\langle 111 \rangle$, $\langle 001 \rangle$ and $\langle 123 \rangle$ [8, 9, 97, 98]. These studies have shown that the $\langle 123 \rangle$ and $\langle 001 \rangle$ oriented specimens deform predominantly by crystallographic slip while the $\langle 111 \rangle$ oriented specimens deform predominantly by twinning [9, 98]. The deformation-induced

twinning in the ⟨111⟩ oriented specimens have been observed to occur at a very early stage of deformation (plastic strain < 5%). At the early stage of deformation, the newly formed twin boundaries act as a barrier to dislocation glide resulting in dislocations pile-ups at the twin boundaries and hence strain-hardening [8]. With continued deformation twin-twin interactions have also been proposed to contribute to the strain-hardening resulting in a stress-strain response with an concave upward shape [9]. The late stage twin-twin interactions in the ⟨111⟩ oriented specimens have been visualized by quantifying local deformation fields using microscale digital image correlation (DIC) technique [10].

Although, the effects of deformation-induced twining on the strain-hardening response of austenitic manganese steels has been well established, less is known about their effects on fracture response of the material. Nevertheless, limited postmortem analysis of polycrystalline and single crystal specimens fractured under uniaxial tension have provided some insight on the effects of twinning on the fracture response of the material. From these experiments, it has been postulated that the cracks predominantly nucleate and propagate along the twin boundaries [95, 102-104]; and the twin boundaries can also serve as obstacle to crack propagation if the angle between the propagating crack and the twin boundary is large [94]. The preferred crack nucleation and propagation along twin boundaries have also been postulated from postmortem analysis of fractured specimens [105, 106] and observed during *in-situ* experiments [107] on other polycrystalline austenitic steels that contain a large amount of pre-existing annealing twins.

The objective of this work is to understand the effect of deformation-induced twinning on the fracture response of an austenitic manganese steel. To this end, *in-situ* tensile tests of dog-bone and single-edge notch sheet specimens of single crystals of the steel of interest are carried out. The crystallographic orientation ⟨111⟩ of the single crystal specimens is chosen to selectively activate twinning and orientation ⟨001⟩ of the single crystal specimens is chosen to selectively activate slip. Furthermore, the *in-situ* tests carried out in this work enabled us to simultaneously capture macroscopic response, microstructure evolution and the distribution of microscale strains.

5.2. Material and methods

The material used in this study is single crystals of Hadfield steel with a nominal composition of 13 wt.% Manganese, 1.1 wt.% Carbon, and rest Iron. The single crystals of Hadfield steel were grown following the Bridgeman technique in Helium atmosphere. These crystals were then subjected to homogenization heat-treatment at 1373 K for 24 hours in an inert gas atmosphere. Next, flat dog-bone specimens with either ⟨111⟩ or ⟨100⟩ crystallographic orientations along the axis of the specimens were prepared following the procedure described in **2.1**. After polishing, the final thickness of all the specimens was approximately 0.7 mm. *In-situ* tensile tests of the dog-bone and single-edge notch specimens of single crystal Hadfield steel were performed either under a high-resolution digital optical microscope (Olympus DSX510) or inside a Scanning Electron Microscope – SEM (Tescan – FERA3) as detailed in **2.2**. Next, the high-resolution images captured during the *in-situ* tensile tests were used to carry out microscale DIC to obtain Eulerian-Almansi strain tensor as described in **2.3**.

The evolution of deformation-induced twinning in select specimens were also characterized using *in-situ* EBSD analysis. Detailed *ex-situ* metallographic analysis of both undeformed and deformed specimens using EBSD analysis and SEM imaging as well as detailed fractographic analysis of the fractured specimens were also carried out.

5.3. Results

Herein, *in-situ* tensile tests of dog-bone and single-edge notch specimens, Fig. 5.1(a), of single crystals of Hadfield steel are carried out to understand the effect of twinning on the deformation and fracture response of the material. EBSD characterization was performed on undeformed specimens and the Inversed Pole Figure map along the x-axis (IPF-X map) of the undeformed specimen is shown in Fig. 5.1(b). The step size for the EBSD scan was 1.2 μm. As shown in Fig. 5.1(b), the x-axis of the scanned area is oriented approximately along the $\langle 111 \rangle$ direction, and from the Euler angles obtained from EBSD data, it was confirmed that the orientation of the gauge section of the specimen is approximately 7^{o} off from the $\langle 111 \rangle$ crystallographic direction.

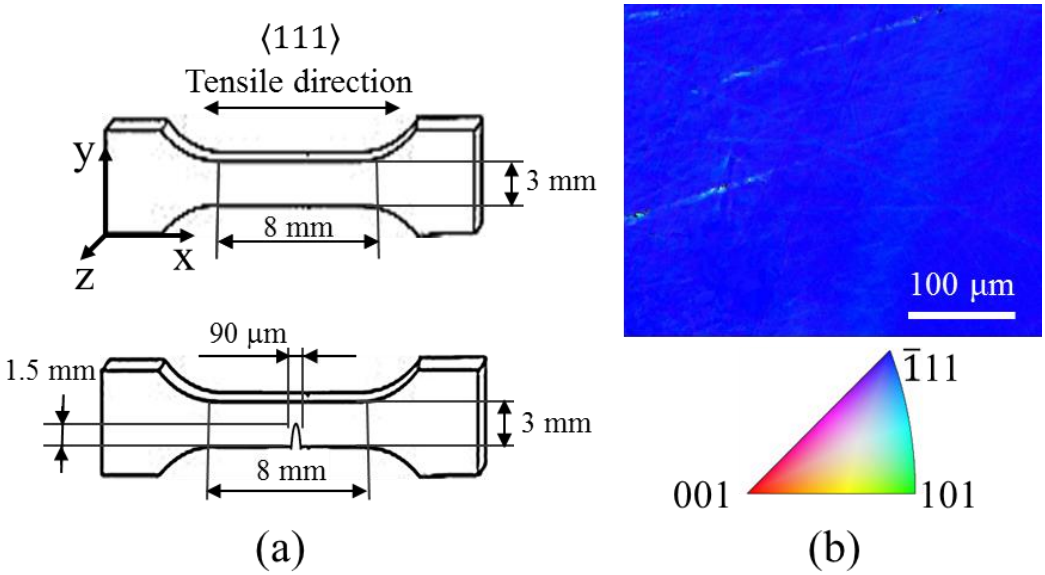

Figure 5.1. (a) Schematic of the dog-bone and single-edge notch specimens. (b) IPF-X map of the undeformed specimen with IPF key.

5.3.1. Deformation response of <111> oriented single crystal under uniaxial tension

The nominal stress-strain response of a dog-bone specimen is shown in Fig. 5.2(a). The stress drops in the curve correspond to the locations at which the test was interrupted to capture high-resolution images. Note that due to the measurement limitation of the tensile stage, the specimen was deformed only until $\varepsilon = 0.46$. The specimen under uniaxial tension yields at around 350 MPa and as the applied nominal strain increases, the strain-hardening rate of the material increases, leading to a concave shape stress-strain curve. The IPF-X map of the deformed dog-bone specimen is shown in Fig. 5.2(b) in a 1750×1250 μm^2 area in the center of the gauge section. The step size of the EBSD scan was 5 μm. The $\Sigma 3 \pm 5^o$ twin boundaries are marked with white solid lines. In this relatively large region, one twin system is activated and most area has undergone twinning, leaving the untwinned area discrete. Note that due to the rather coarse step size, thin untwinned stripes between adjacent twin bands may not have been characterized, resulting in a larger

area fraction of twinned region than expected. In a ⟨111⟩ oriented specimen, three twin systems can activate [9], however, due to a ~7° offset of the loading direction from the ⟨111⟩ crystallographic direction, only one twin system $(1\bar{1}1)$ [121] in this specific case is found to activate.

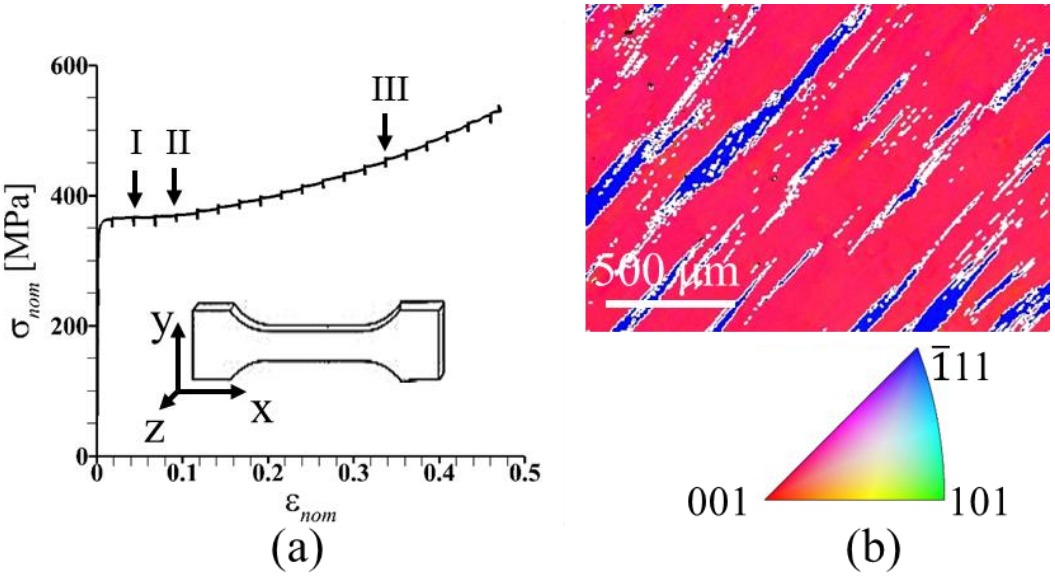

Figure 5.2. (a) Nominal stress-strain ($\sigma_{nom} - \varepsilon_{nom}$) response of a dog-bone specimen of <111> oriented single crystal Hadfield steel. (b) Post deformation IPF-X map at $\varepsilon = 0.46$ with IPF key. The Σ3±5° twin boundaries are marked with white lines.

The axial strain (ε_{xx}) distribution contour maps obtained from DIC at ε_{nom}= 0.042, 0.092 and 0.34 are shown in Fig. 5.3. The locations of these three nominal strains are marked as I, II and III in Fig. 5.2(a). As shown in the schematic in Fig. 5.3(a), a rectangular region, ABCD, in the center of the gauge section of the dog-bone specimen is selected as the region of interest for DIC analysis, and the coordinate of DIC analysis is plotted with x and y axes marked on the top left of the schematic. At a rather small imposed deformation, ε_{nom}= 0.042, strain localization occurs in several bands. Due to the obvious deflection on the edge of region of interest at strain localization bands, the strain

localization bands are likely due to twinning which is also confirmed later by EBSD analysis. As shown in Figs. 5.3(c) and (d), with increasing applied strain, new twin keeps nucleating while adjacent twin bands widen and coalesce. At large applied strain, ε_{nom}= 0.34, most of the area has undergone twin transformation and interaction of twin bands is also seen, confirming the observation in post deformation IPF-X map in Fig. 5.2(b). Few spots with noisy DIC data inside in the contour plots can be seen in Figs 5.3(a), (b) and (c), especially at late stage of deformation. These are caused by the nucleation of micro-cracks on the surface of the specimen. DIC results are affected around micro-cracks and leave noisy spots in the contour plot.

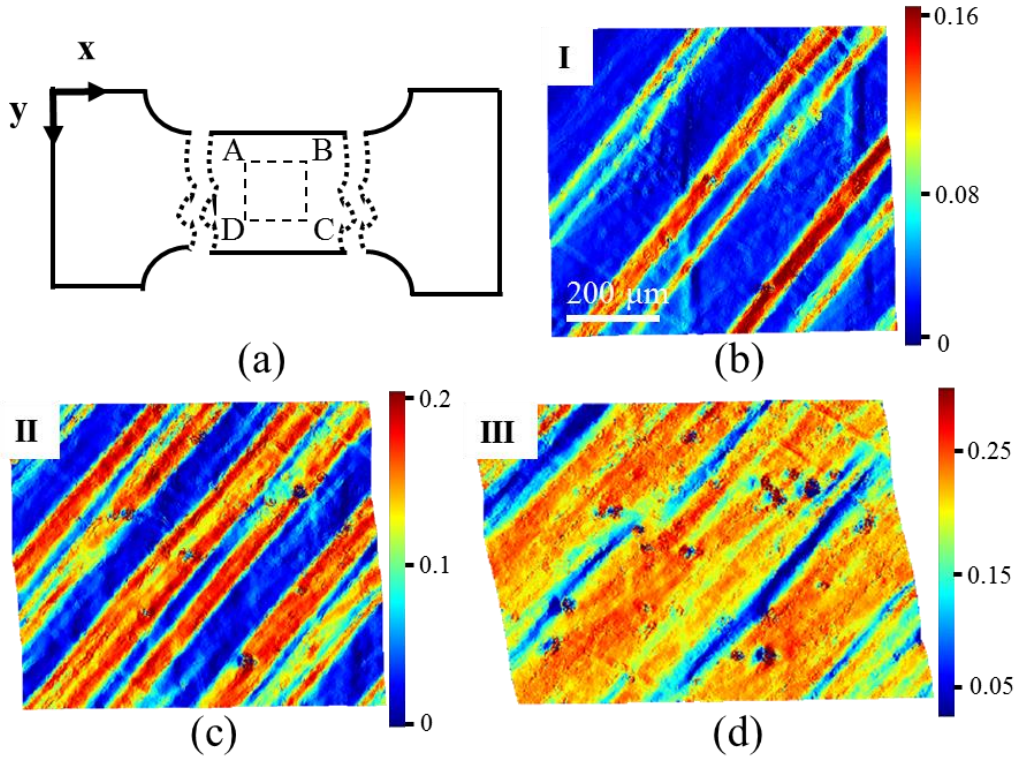

Figure 5.3. (a) Schematic of a dog-bone specimen showing the location of the region of interest, ABCD, for DIC analysis. The axial strain (ε_{xx}) distribution at a nominal imposed strain of (b) 0.042, (c) 0.092 and (d) 0.34 (marked as I, II and III in Fig. 5.2(a), respectively). The localization of ε_{xx} indicates deformation by twinning.

5.3.2. Deformation and fracture response of <111> oriented single crystal

The *in-situ* tensile test of dog-bone specimen of ⟨111⟩ oriented single crystal Hadfield steel indicates twinning behavior during uniaxial deformation. The fracture behavior for dog-bone specimen is difficult to analyze via *in-situ* tensile test because the location of crack initiation is unpredictable, and the crack propagates too rapidly to capture. Hence, a single-edge notch specimen of ⟨111⟩ oriented single crystal Hadfield steel is used to analyze the effect of deformation twin on fracture response of the material. The evolution of normalized force (F_n) with normalized displacement (δ_n) of a single-edge notch specimen during *in-situ* tensile test under optical microscope is plotted in Fig. 5.4(a). The red diamond on the curve indicates the crack initiation point, and the optical image close to the notch is shown in Fig. 5.4(b), with the blue arrow showing the crack propagation direction. The force post crack initiation slightly increases with applied displacement first and then keeps decreasing until rapid force drop occurs and specimen fractures completely.

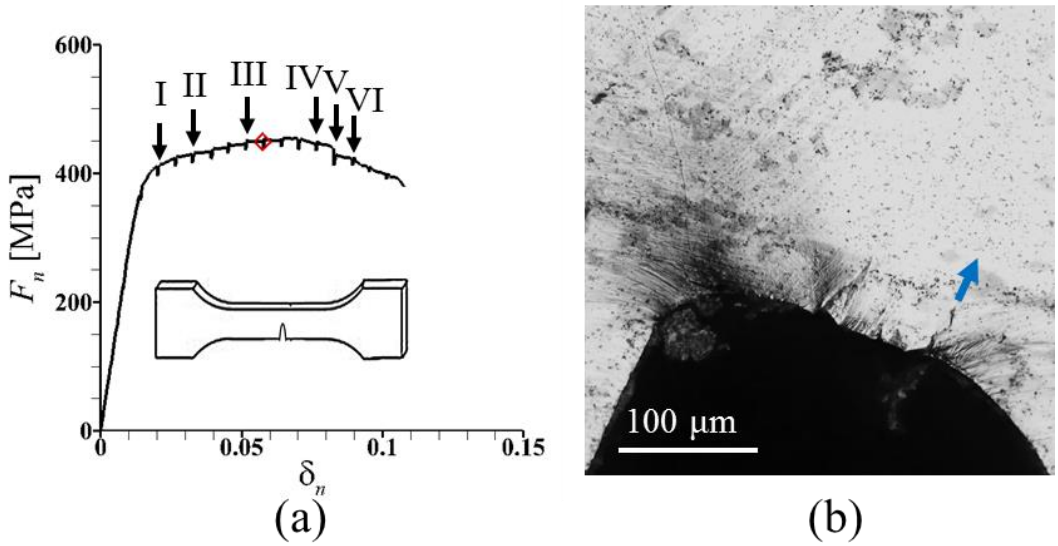

Figure 5.4. (a) Force normalized by the minimum cross section area (F_n) versus displacement normalized by the gauge length (δ_n) curve obtained from the tensile test of a single-edge notch specimen of <111> oriented single crystal of Hadfield steel. The red diamond on the curve marks the initiation of a crack from the deformed notch. (b) Optical micrograph showing crack initiation from the deformed notch. The propagation direction of the crack is marked with a blue arrow.

The axial strain (ε_{xx}) distribution contour maps obtained by DIC at δ_n= 0.02, 0.033 and 0.051 prior to crack initiation (I, II and III marked in Fig. 5.4(a), respectively) at a location close to the initial notch are shown in Fig. 5.5 to reveal deformation twin under complex loading condition. The localization of ε_{xx} indicates the location of twin. As shown in Fig. 5.5(a), a rectangular region, ABCD, close to the notch of single-edge notch specimen is selected as a region of interest for DIC analysis, and the coordinate of DIC analysis is plotted with x and y axes. Twin occurs at a low strain level, δ_n= 0.02, right after linear regime as shown in F_n - δ_n curve in Fig. 5.4(a). The twin close to the notch is relatively mature comparing to that away from the notch. As applied displacement

increases to δ_n= 0.033 and 0.051, large fraction of specimen surface is covered with twins by new twin formation, individual twins widen, and adjacent twins coalesce. Close to the notch, the axial strain also localizes along 45^o bands originating from the notch tip due to the strain concentration effect of the notch tip. Strain localization caused by twin interacts with the field induced by the presence of the notch and it forms a special strain distribution map close to the notch tip which is different from the strain distribution map of dog-bone specimen. The dotted white lines of each strain distribution map in Figs. 5.5(b), (c) and (d) indicate the shape and location of the current notch tip. Noticeably, notch deforms asymmetrically with increasing applied deformation, causing the curvature of the right part of the notch tip to decrease significantly, while the curvature of the left part remains roughly the same as was in the undeformed configuration.

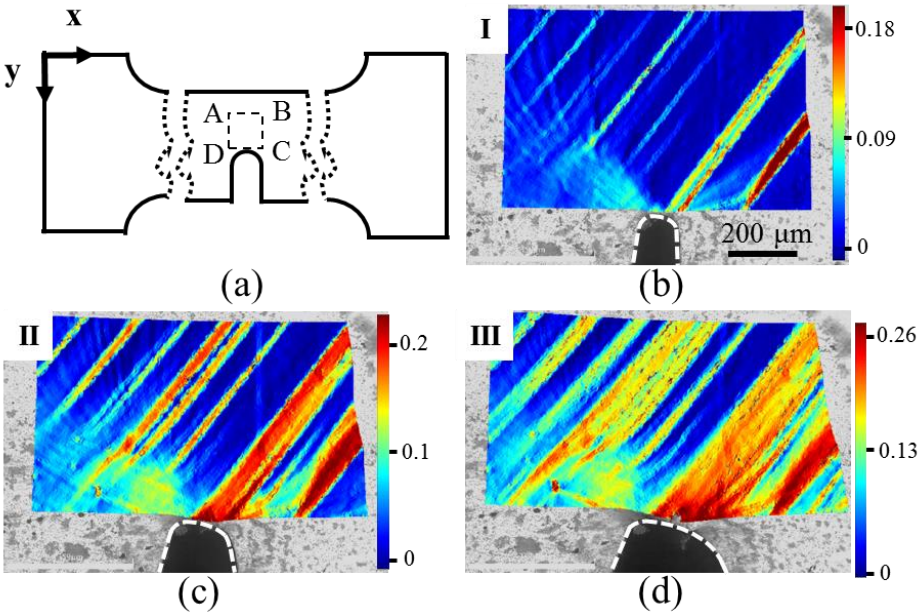

Figure 5.5 (a) Schematic of a single-edge notch specimen showing the location of the region of interest, ABCD, for DIC analysis. The axial strain (ε_{xx}) distribution at a δ_n value of (b) 0.02, (c) 0.033 and (d) 0.051 (marked as I, II and III in Fig. 5.4(a), respectively). The localization of ε_{xx} indicates the deformation by twinning. The dotted white line marks the current shape and location of the notch.

In the next optical image at δ_n= 0.058 after applied displacement at location III, crack initiation is observed, Fig. 5.4(b). A smaller region of interest area slightly away from the notch tip ahead of the crack propagation direction, as marked with the blue arrow in Fig. 5.6(a), is selected for DIC analysis to reveal the twin-crack interaction. The zoomed in axial strain (ε_{xx}) distribution contour maps obtained by DIC analysis at δ_n= 0.076, 0.083 and 0.089 post crack initiation (IV, V and VI marked in Fig. 5.4(a), respectively) at a location along the crack propagation path are shown in Figs. 5.6(b), (c) and (d), respectively. In twin areas, twin boundaries leave noisy DIC results due to large extent of deformation, and the crack initiates and propagates along twin boundary at first (Fig. 5.6(a) and (b)). As the crack propagates, the twin area ahead of the crack propagation direction also propagates towards left top direction and traps the crack tip inside the twin area. The crack tip tends to propagate towards the direction of twin area propagation and crack starts to bifurcate (Fig. 5.6(c)). When the crack bifurcates, the newly formed branch keeps propagating (note that the bifurcated crack keeps propagating along the black arrow) while the initial branch is arrested (Fig. 5.6(d)). Fig. 5.7(e) is one optical image taken after Fig. 5.6(d), and it further shows the propagation of the new branch. DIC result for Fig. 5.7(e) is not available because the region of interest continuously moves out of the optical image due to severe local deformation close to the crack during crack propagation.

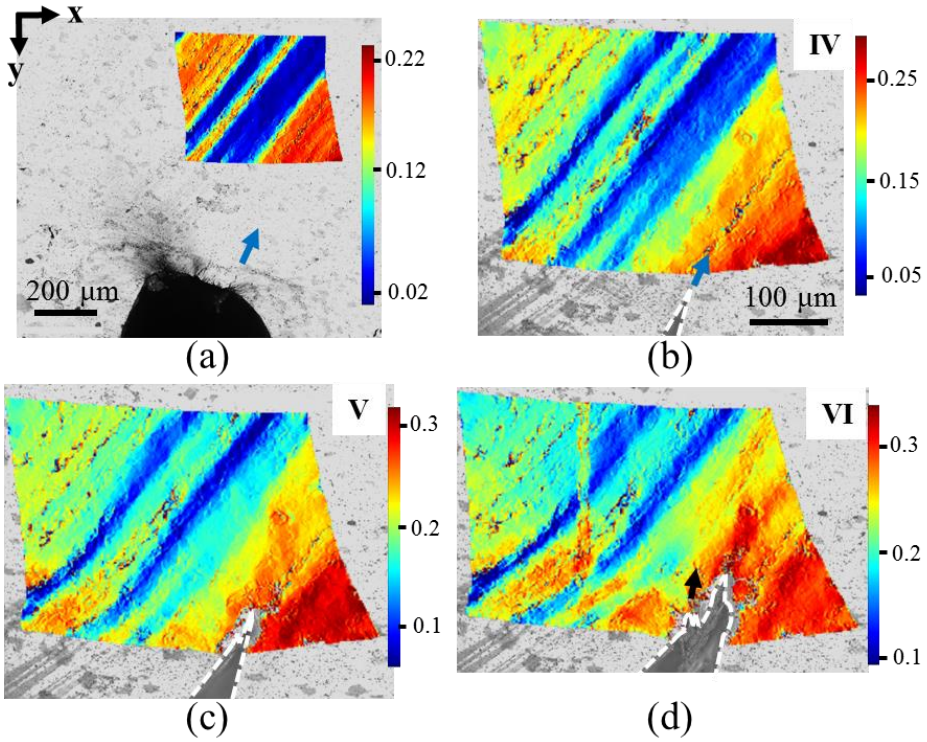

Figure 5.6. The axial strain (ε_{xx}) distribution at the (a) crack initiation and δ_n= (b) 0.076, (c) 0.083 and (d) 0.089 (IV, V and VI in Fig. 5.4 (a), respectively) at a location away from the initial notch and along the crack propagation path. The dotted white lines indicate the current shape and location of the growing crack. Blue arrow indicates the crack propagation direction before crack bifurcation and black arrow indicates the crack propagation direction after crack bifurcation.

Next, the surface of the fully fractured specimen close to the fracture surface is characterized with SEM. Fig. 5.7(a) shows the low magnification SE image from the notch tip across the gauge width. The position and shape of the notch and part of the crack close to the notch tip are marked with dotted black-white lines. Multiple crack bifurcation (location I and II, high magnification SE images of both sides of crack at location I and II are shown in Figs. 5.7(d) and (c), respectively) are observed along the crack path, where location I is the crack bifurcation captured during *in-situ* test, Fig. 5.6. At the location away from pre-notch (location III), micro-cracks on the surface can be observed, which

could be due to slip-twin interaction at twin boundaries leading to stress concentration and multiple micro-crack nucleation within twinned areas [108, 109]. By comparing the SE images at same location on both side of crack, it can be concluded that generally the specimen surface on the side where primary twin locates shows more damage than the other side.

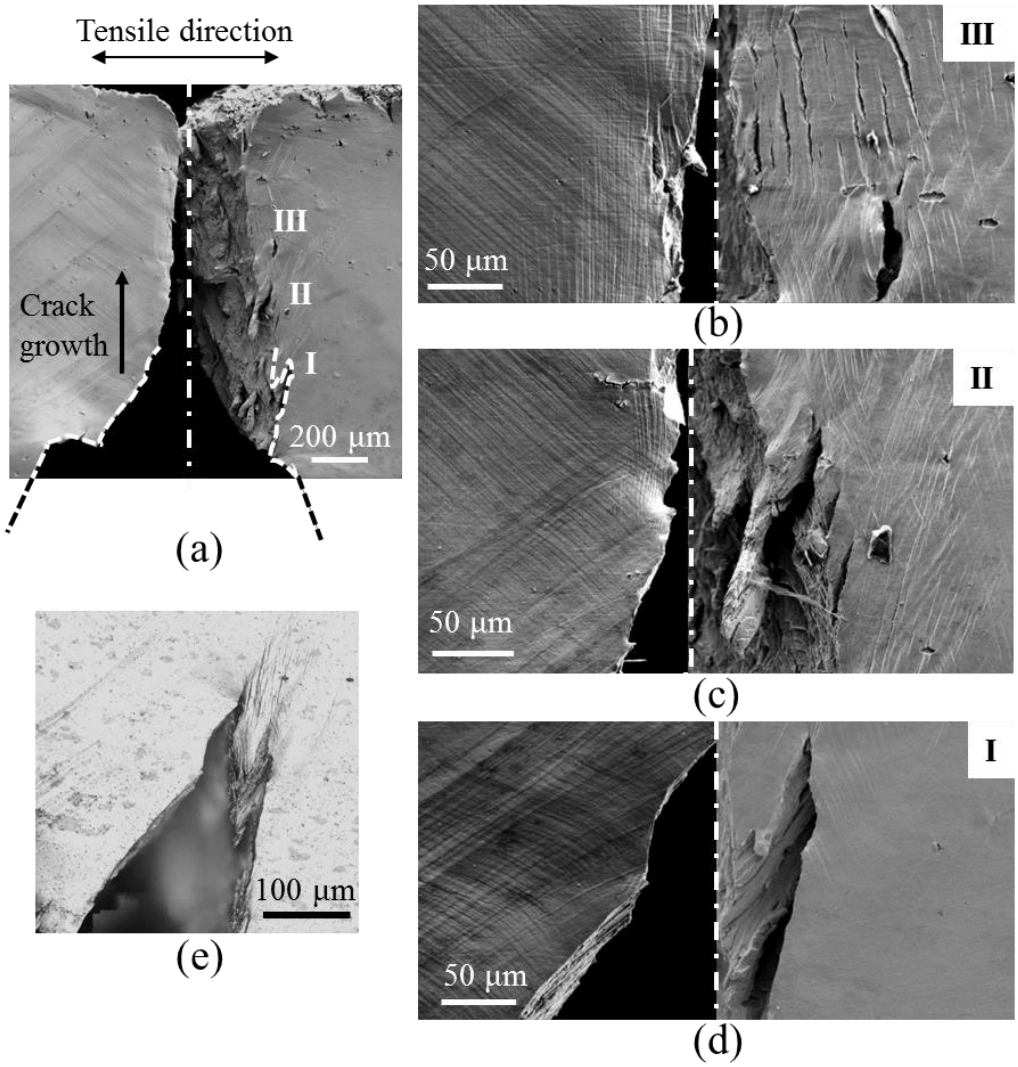

Figure 5.7. Specimen surface on both sides of the fractured single-edge notch specimen of <111> oriented single crystal Hadfield steel. (b), (c), and (d) are high magnification images of locations III, II and I, respectively. Location I is the crack bifurcation captured in Fig. 5.6 and morphology of crack at δ_n= 0.095 is shown in (e).

Next, the surfaces of both half of the fractured specimen are polished until 0.05 μm alumina and the orientation of sub-micron scale area close to crack on the polished surface of fractured specimen was characterized with EBSD with step size of 0.5 μm. The IPF-X map of the surface of the specimen along crack 0-400 μm away from the initial notch is shown in Fig. 5.8. Most area at the right side of crack has already finished twin transformation while at left side of crack there still exists some area that are oriented along ⟨111⟩ (i.e., these areas have not undergone twinning). The area at 200-400 μm away from the original notch tip is location I in Fig. 5.7. Due to the large extent of deformation and tilt close to initial notch and crack bifurcation location, the untwinned areas are oriented away from ⟨111⟩, resulting in various colors in IPF-X map. The postmortem EBSD further confirmed the observation of DIC result that as the crack propagates, the crack tip was trapped inside the twinned area and the new branch of the bifurcated crack keeps propagating along the new twin boundary. In the area involved in EBSD characterization, one twin system $(1\bar{1}1)$ $[\bar{1}12]$ is activated.

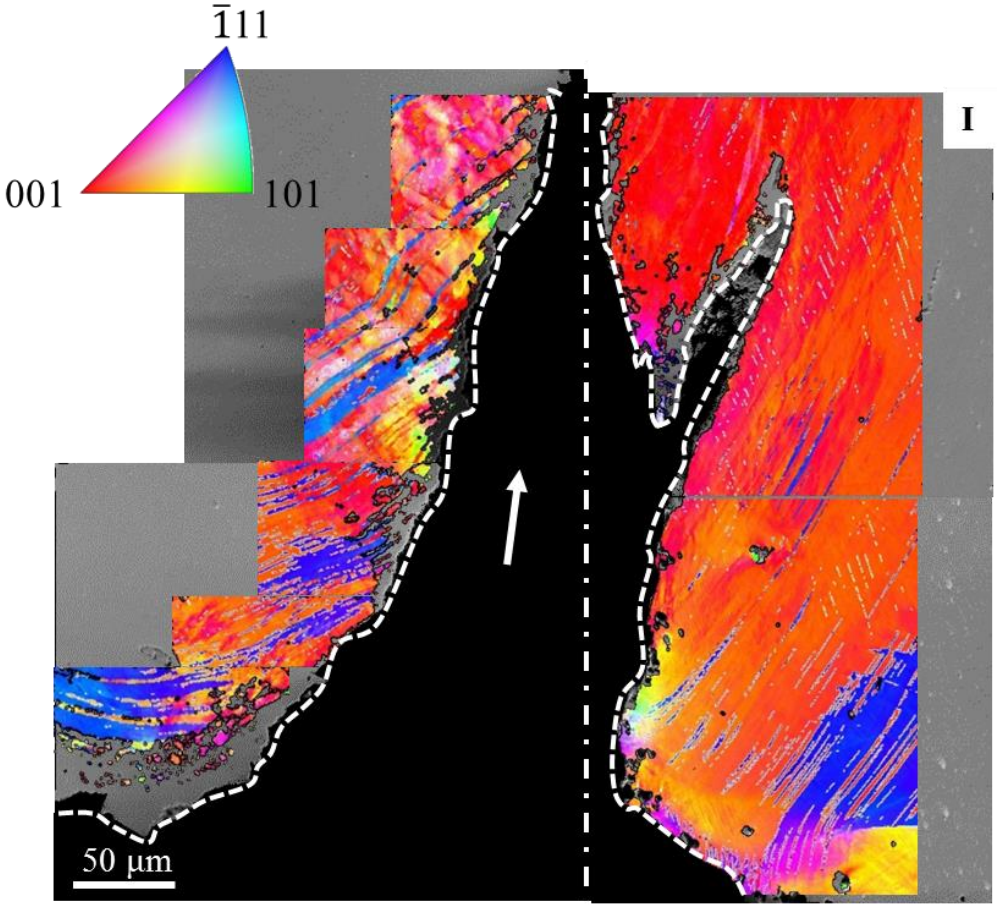

Figure 5.8. Postmortem IPF-X map of the polished surface of the fractured single-edge notch specimen of <111 > oriented single crystal Hadfield steel specimen at 0-400 μm away from the initial notch. White arrow marks the crack propagation direction and fracture line is highlighted with white dotted lines.

The IPF-X map of the surface of the specimen along crack 400-800 μm away from the initial notch is shown in Fig. 5.9(a). The step size of EBSD scan is 0.5 μm. Most area at the right side of the crack has already finished twin transformation. At around 600 μm away from the initial notch, most area on the left side of the crack finished twin transformation. The distribution of the crystal orientations is plotted in IPF color keys for each IPF-X map in the black blocks in Fig. 5.9(b). At locations 1 and 2, most of orientation distributes close to ⟨001⟩, which has finished twin transformation. In contrast, at locations

3 and 4, the distribution of orientation close to ⟨111⟩ is unneglectable. Comparing to location 3, the crystal orientation distribution in location 4 tends to concentrate at ⟨001⟩. The distribution of the crystal orientations in IPF color keys confirms the qualitative observations of Fig. 5.9(a). Close to crack bifurcation (location II marked in Fig. 5.7), the left side of the crack undergoes large deformation and tilt and correspond to various colors in the IPF-X map.

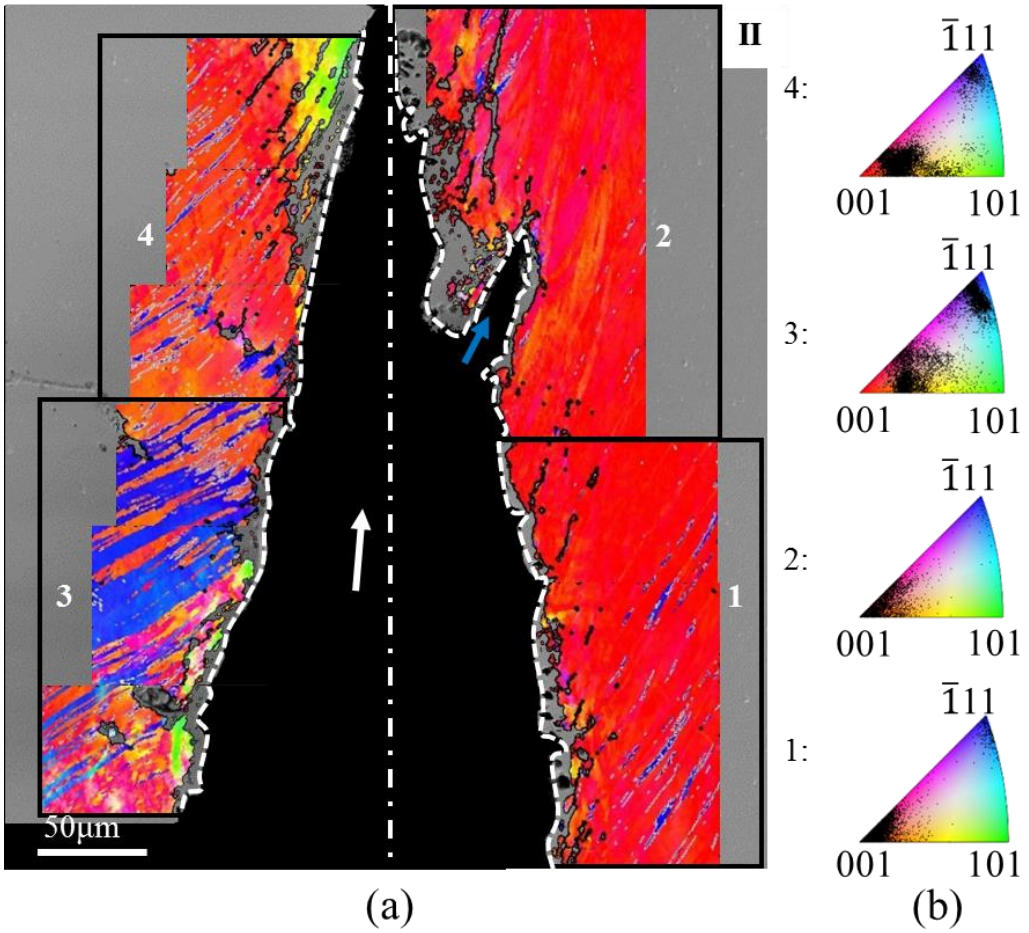

Figure 5.9. (a) Postmortem IPF-X map of the polished surface of the fractured single-edge notch specimen of <111> oriented single crystal Hadfield steel at 400-800 μm away from the initial notch. White arrow marks the crack propagation direction and fracture line is highlighted with white dotted lines. (b) The distribution of the crystal orientations is marked in IPF color keys for the regions marked as 1-4 in the IPF-X map.

SE-SEM images of the fracture surface of the single-edge notch specimen of ⟨111⟩ oriented single crystal Hadfield steel are shown in Fig. 5.10. The loading direction, x-axis, is into the viewed plane. The notch tip is on the right of the low magnification image through thickness, and crack propagation direction is marked with white arrow in the low-resolution image at top left of Fig. 5.10. The whole fracture surface presents similar features, which are dimples together with quasi-cleavage facets and delamination cracks normal to the fracture surface. High-resolution images of the location marked as I, II and III are also shown in Fig. 5.10. In all these high-resolution images, randomly distributed small dimples together with signs of plastic deformation on the large quasi-cleave facets can be seen. There are also few large holes on the fracture surface that are likely pre-exiting pores in the material. Note that grain boundaries are usually attributed to delamination cracks on the fracture surface [110, 111], however, no grain boundary is involved in single crystal Hadfield steel and thus, the delamination cracks are likely due to the separation of twin boundaries normal to the crack propagation direction.

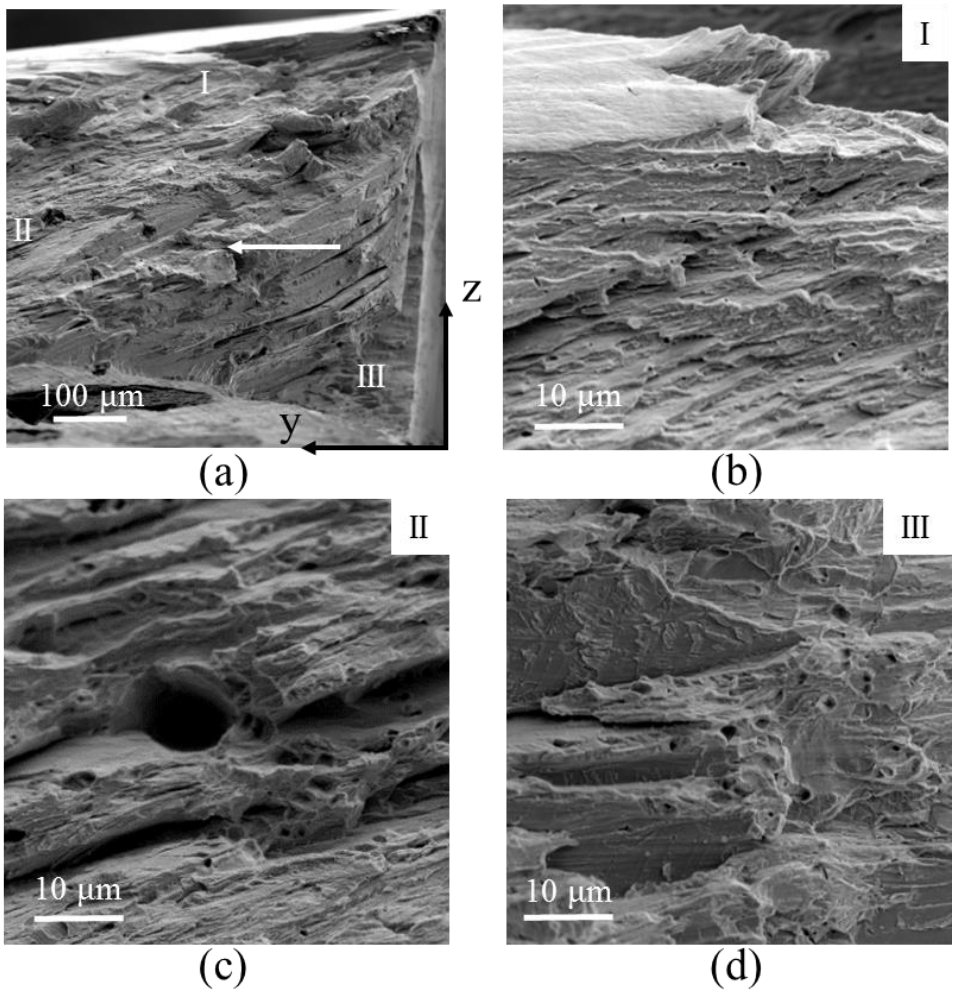

Figure 5.10. SE-SEM images of the fracture surface of the single-edge notch specimen of <111> oriented single crystal Hadfield steel. The loading direction is into the viewed plane. Crack propagation direction is marked with white arrow in the low magnification image at top left.

5.3.3. Twin evolution and crack growth interaction of <111> oriented single crystal

In-situ EBSD tensile test was also performed on a single-edge notch specimen to gather more information on the twin-crack interaction. Normalized force (F_n) vs. normalized displacement (δ_n) curve of the single-edge notch specimen during *in-situ* EBSD tensile test is shown in Fig. 5.11(a). The red diamond on the curve indicates the crack initiation and the SE image close to the deformed notch at crack initiation is shown

in Fig. 5.11(b). The eventual propagation direction of the crack is marked with a blue arrow. The two curves of mechanical response of single-edge notch specimen, Fig. 5.4 and Fig. 5.11, are in good agreement with one another.

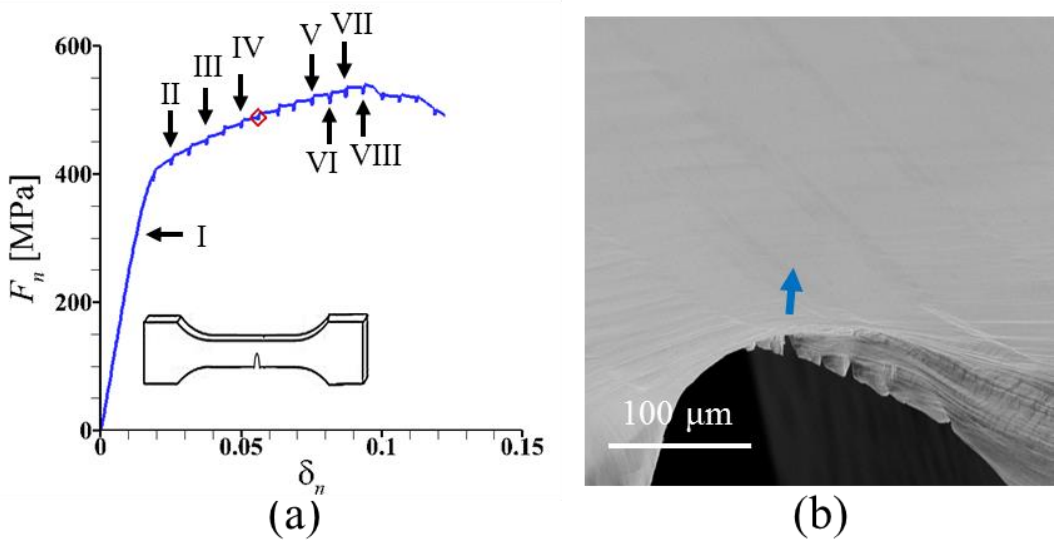

Figure 5.11. (a) Force normalized by the minimum cross section area (F_n) versus displacement normalized by the gauge length (δ_n) curve obtained from the tensile test of a single-edge notch specimen of <111> oriented single crystal of Hadfield steel during *in-situ* EBSD tensile test. The red diamond on the curve marks the initiation of a crack from the deformed notch. (b) SE-SEM micrograph showing crack initiation from the deformed notch. The propagation direction of the crack is marked with a blue arrow.

IPF-X maps at δ_n= 0.013, 0.025, 0.038 and 0.050 (I, II, III, and IV in Fig. 5.11(a), respectively) at location close to the notch is shown in Fig. 5.12. The step size of the EBSD scan is 1 μm. At no load condition, the single crystal orientates along ⟨111⟩, as marked by location 1 in Fig. 5.12(a). At δ_n= 0.013, although the specimen is still under linear mechanical response as shown in the F_n-δ_n curve, one twin on the right side of notch occurs, which is marked as location 2 in Fig. 5.12(a). At δ_n= 0.025, location 2 widens rapidly. Meanwhile new twin with a different variant from the twin at δ_n= 0.025 occurs

on the left side of the notch, as marked as location 3 and 4 in Fig. 5.12(b). Note that some extent of axial strain localization can also be observed on the left side of the notch in Figs. 5.5(b) (c) and (d). It can be hypothesized that two variants of twin occur on both sides of the notch, causing axial strain localization inside twin, and only one variant of twin becomes prominent twin. New twin keeps nucleating (location 5 in Fig. 5.12(c)) and existing twin keeps developing as applied displacement increases to 0.038 and then to 0.050. Due to large extent of deformation, the surface of the specimen becomes rough and some locations cannot be indexed, leaving blank data points on the surface.

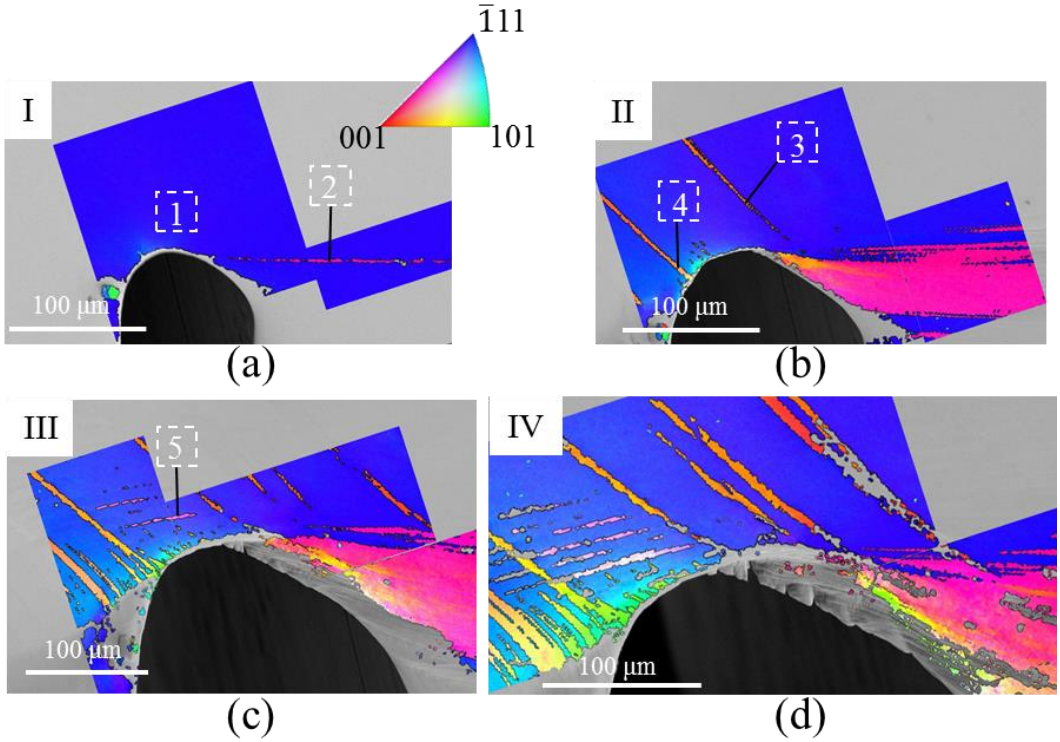

Figure 5.12. IPF-X maps at δ_n= 0.013, 0.025, 0.038 and 0.050 (I, II, III, and IV in Fig. 5.11(a), respectively) at location close to the notch.

As applied strain increases, all locations close to the notch are deformed and tilted, causing a change of crystal orientation. With EBSD data, the twin systems can be obtained,

and the two variants of twin are $(11\bar{1})$ $[\bar{1}21]$ and (111) $[\bar{2}11]$. Locations 2 and 5 are the same variant twin with twin system $(11\bar{1})$ $[\bar{1}21]$ while locations 3 and 4 are the same variant twin with twin system (111) $[\bar{2}11]$.

The IPF-X maps at δ_n=0.075, 0.081, 0.087 and 0.093 (V, VI, VII and VIII in Fig. 5.11(a), respectively) at locations ahead of crack are shown in Fig. 5.13. The step size is 1 μm. The crack is highlighted with white dotted lines. Due to severe deformation, IPF index in some area are not detected. According to Fig. 5.12 and the EBSD result at δ_n=0.075, 0.081 in current figure, one can infer that the unindexed area at right side of the crack has accomplished twin transformation while the unindexed area at left side of the crack has not. Crack is trapped in the twinned area and the crack tip blunt but with corners. At δ_n=0.093, the new branch of the crack tip propagates along the twin boundary, while the other branch is trapped in the twinned area. This reconfirms the observation made from the DIC analysis.

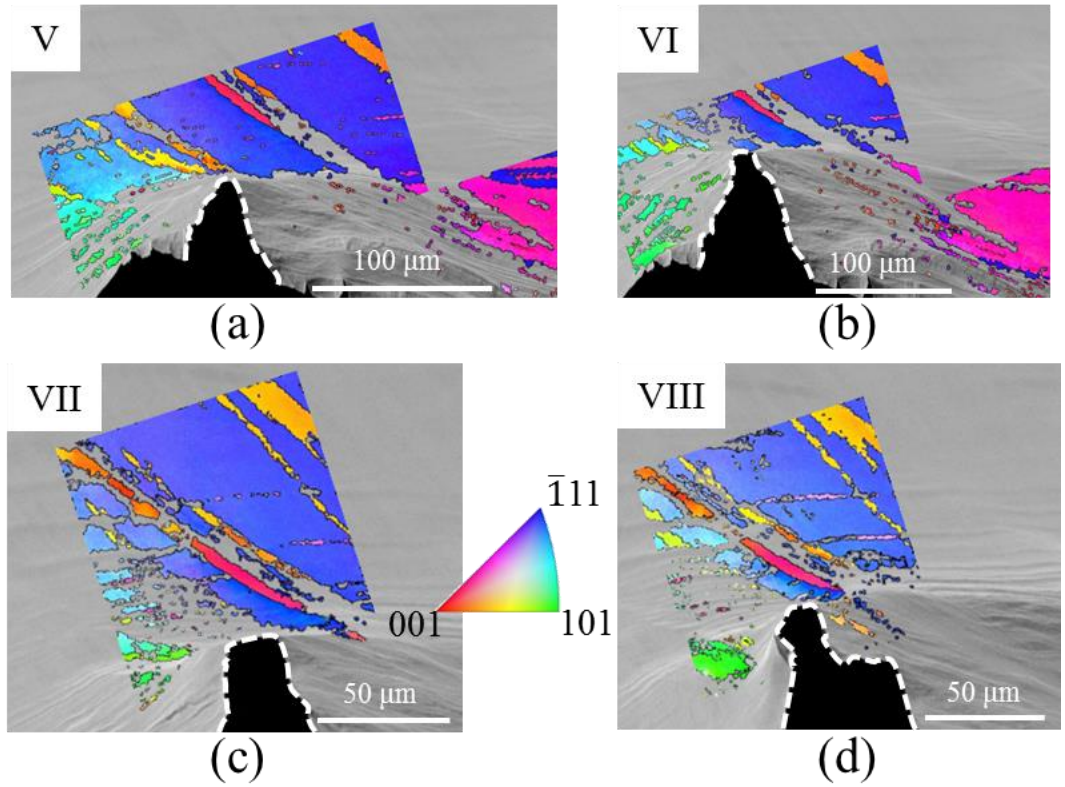

Figure 5.13. IPF-X maps at δ_n=0.075, 0.081, 0.087 and 0.093 (V, VI, VII and VIII in Fig. 5.11(a), respectively) at locations ahead of the growing crack, which is highlighted with white dotted lines.

5.4. Discussion

The asymmetrical notch deformation was repeatedly during the *in-situ* tensile testing of the single-edge notch specimens of ⟨111⟩ oriented single crystal Hadfield steel. These show consistently that the curvature of the right part of the notch decreases and that of the left part of the notch approximately remains the same. This can be attributed to deformation-induced twinning. To confirm this, *in-situ* tensile test under optical microscope was performed on a single-edge notch ⟨001⟩ oriented single crystal Hadfield steel. The ⟨001⟩ oriented specimens are known to not undergo deformation-induced twinning under overall tensile deformation. Normalized force (F_n) vs. normalized

displacement (δ_n) curve of single-edge notch specimen of $\langle 001 \rangle$ oriented single crystal Hadfield steel during *in-situ* tensile test under optical microscope is shown in Fig. 5.14(a). The red diamond on the curve indicates the crack initiation. The specimen yields at around 380MPa, and the strength at crack initiation is 580 MPa. Axial strain (ε_{xx}) distribution at δ_n=0.03 prior to crack initiation at location close to the notch of $\langle 001 \rangle$ oriented specimen is shown in Fig. 5.14(b). The dotted white lines in each strain distribution map indicate the shape and location of the current notch. Unlike $\langle 111 \rangle$ oriented specimen, the localization of ε_{xx} distributes symmetrically along the center of notch in the single-edge notch specimens of $\langle 001 \rangle$ oriented single crystal Hadfield steel. Post crack initiation, the axial strain (ε_{xx}) distribution at δ_n=0.08 at location close to notch of $\langle 001 \rangle$ direction specimen is shown in Fig 5.14(c). As shown in the figure, the crack nucleates in the center of the notch and propagates approximately along the notch length direction. Besides, the axial strain shown in Figs. 5.14(b) and (c) before and after crack initiation, respectively, also localizes symmetrically along 45^o direction originating form the notch tip. This confirms that the asymmetrical deformation of the notch tip in the <111> oriented single-edge specimens are due to the deformation induced twinning. Note that this is in contrast to previous works on single crystal magnesium alloys that showed that twin initiated and evolved approximately symmetrically on both side of the notch [113, 114] leading to symmetrical deformation of the notch prior and post crack initiation.

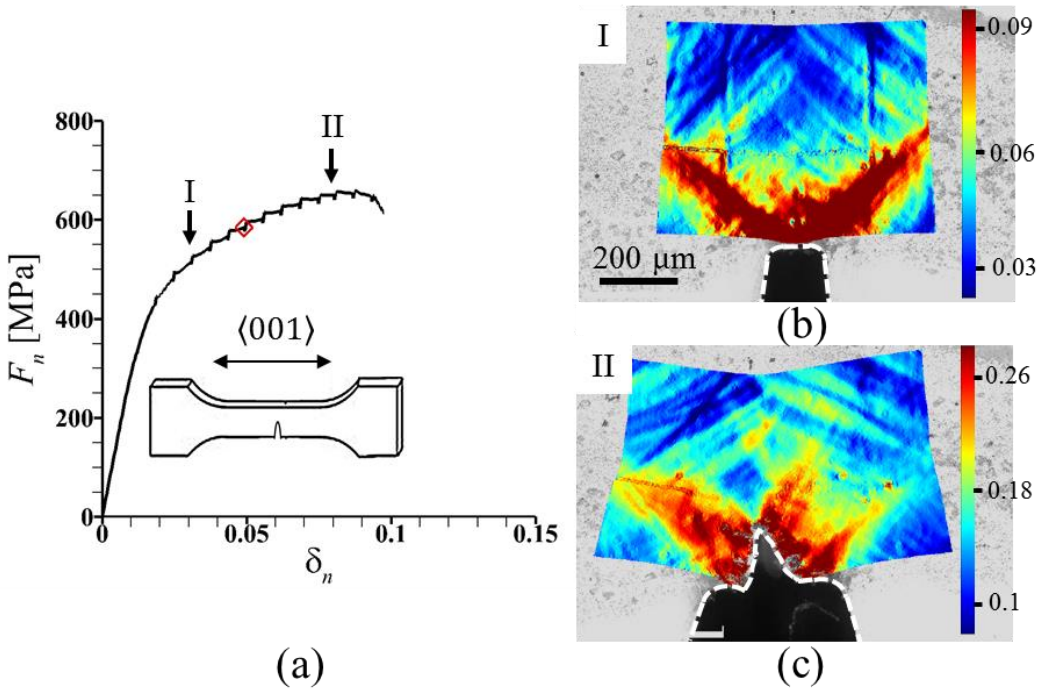

Figure 5.14. (a) Force normalized by the minimum cross section area (F_n) versus displacement normalized by the gauge length (δ_n) curve obtained from the tensile test of a single-edge notch specimen of <001> oriented single crystal of Hadfield steel during *in-situ* under an optical microscope. The red diamond on the curve marks the initiation of a crack from the deformed notch. Axial strain (ε_{xx}) distribution at δ_n= (b) 0.03 and (c) 0.08 (I and II in (a), respectively) at a location close to the notch tip. The dotted white lines in each strain distribution map indicate the current shape and location of the deforming notch and crack.

As shown here, the cracks in single-edge notch specimens of ⟨111⟩ oriented single crystal Hadfield steel predominantly grow along the twin boundaries, however, with increasing load, previously nucleated twins continue to widen that leads to crack tip blunting and crack growth arrest. This results in the crack bifurcation during the crack propagation. The crack growth arrest and crack bifurcation enhance the fracture resistance of this material. For example, the macroscopic normalized deformation to failure is ~0.11

for the ⟨111⟩ oriented specimens while it is ~0.09 for the ⟨001⟩ oriented specimens of the Hadfield steel.

5.5. Concluding remarks

In-situ tensile tests of dog-bone and single-edge notch sheet specimens of carefully grown single crystals of an austenitic manganese steel are carried out. The crystallographic orientations of the single crystal specimens are chosen to selectively activate crystallographic slip or twinning. The *in-situ* tensile tests coupled with microscale Digital Image Correlation and Electron Backscattered Diffraction analysis allow us to simultaneously capture macroscopic response, distribution of microscale strains, and local microstructure evolutions. Our results show that in the <111> oriented single-edge notch specimens of single crystal Hadfield steel (as confirmed for the first time using *in-situ* tensile tests coupled with microscale DIC and EBSD analysis), twinning causes asymmetrical deformation of the notch tip. Next, a crack nucleates from the deformed tip and first propagates along a twin boundary. However, widening of twins leads to crack growth arrest and large crack tip blunting. Finally, with progressive loading the crack bifurcates and continues to grow. This process is repeatedly observed until final fracture. On the contrary, in the absence of deformation-induced twinning, as confirmed by the *in-situ* tensile tests of <001> oriented single-edge notch specimens of single crystal Hadfield steel, the notch deforms symmetrical and crack nucleates from the center of the deformed notch that roughly grows straight ahead. These results clearly show that the spatial and temporal evolutions of the material microstructure should be considered in any mechanistic analysis of the interaction of deformation-induced twinning and crack growth.

6. SYNERGISTIC EFFECTS OF CORROSION AND MECHANICAL LOADING ON PRE-MATURE FRACTURE OF AN ALUMINUM ALLOY*

6.1. Introduction

Structural alloys are susceptible to premature failure due to the synergistic effects of environmental assisted degradation and imposed mechanical loading, referred to as environmental assisted cracking (EAC). Such a premature failure of structural alloys is observed in many applications ranging from oil and gas to aerospace [115-117]. In fact, a large percentage of aircrafts suffer from EAC [117]. This is true even with the use of structural alloys, such as the high strength aluminum alloys, that form a natural passive layer [118], because in highly aggressive environment and under imposed mechanical loading the natural passive layer of the alloys tends to deteriorate [119]. In addition, the microstructure of the high strength aluminum alloys, such as AA7075 (Al-Zn-Mg alloy), contains intermetallic particles that are introduced to enhance the mechanical properties of the material. But the presence of intermetallic particles can adversely affect the formation of the natural passive layer, as well as can result in the formation of micron-scale galvanic cells, making the material vulnerable to localized corrosive attacks [120-124].

Classically, EAC can involve a combination of mechanisms such as anodic dissolution, tarnish rupture, film induced cleavage, and adsorption-enhanced cracking [115, 125]. While a particular mechanism of the EAC in structural alloys remain debatable and depends on specific conditions related to material, environment and loading. It is generally recognized that the processes of localized corrosion such as pitting, intergranular

*Reprinted with permission from "Synergistic effects of corrosion and slow strain rate loading on the mechanical and electrochemical response of an aluminium alloy" by Xinzhu Zheng, Homero Castaneda, Huajian Gao, Ankit Srivastava, 2019. Corrosion Science, 153, 53-61, Copyright [2019] by Name of Xinzhu Zheng.

corrosion or exfoliation in a susceptible material such as AA7075 are aggravated by the presence of tensile stresses, resulting in EAC [11, 126-130]. The EAC of AA7075 is an active topic of research due to its technological importance for a host of structural applications. In general, EAC susceptibility of AA7075 is studied by exposing the specimens to a number of corrosive environments such as sodium chloride or EXCO solutions, under static or slow strain rate (SSR) tensile loading [11, 126-130]. In conventional static tests, the EAC susceptibility of the material is expressed in terms of time to failure at a given imposed tensile stress level. On the other hand, the SSR testing can provide degradation in mechanical properties of the material. However, if the test time or the imposed strain rate is the controlling parameter in EAC experiments, it can be expected that the EAC of the material will strongly depend on both the application of the tensile stresses/strains and the establishment of the favorable electrochemical conditions for corrosion and cracking. Nevertheless, the attempts to characterize the electrochemical response of AA7075 in literature has been limited to static EAC tests [11, 127] and for one imposed strain rate under SSR EAC test [130].

The SSR testing in a corrosive environment over a range of imposed strain rates provides full detail of the environmental assisted degradation on the mechanical response of the material and is the most reproducible test of EAC [131]. During SSR testing the continuous application of strain on the specimen facilitates crack nucleation and propagation. Additionally, the measured dependence of mechanical properties on the imposed strain rate can be used to infer the mechanism of EAC [119, 131-133]. For example, the presence of a minimum strain rate below which the degradation in the

mechanical properties is no longer noticeable is considered as evidence of the slip-dissolution mechanism of EAC [119, 131, 132]. For the slip-dissolution mechanism, a minimum strain-rate is assumed to result from a competition between re-passivation and blunting at the crack tip. But it has also been argued that hydrogen embrittlement or pitting induced EAC need not exhibit a minimum strain rate for mechanical degradation [119]. Furthermore, during SSR testing if the imposed strain rate is too high the material can simply fail by mechanical overload while it is also possible for the strain rate to be too slow for EAC to occur [131, 134]. This is because once the specimen is exposed to a corrosive environment, the electrochemical reactions at the electrolyte/specimen interface can result in the formation of a corrosion film as such the role of the imposed strain rate is to either promote rupture of the film or maintain a transition film of poor quality that facilitates crack initiation and propagation [135]. Hence, it is warranted to characterize both the mechanical and the electrochemical response of the material as a function of the imposed strain rate during SSR EAC tests.

In this work the objective is to characterize the synergistic effect of localized corrosion and imposed strain rate on the overall mechanical and electrochemical response of the material during SSR EAC tests. Specifically, this work focus on answering questions such as: How does the imposed strain rate affect the process of localized corrosion and the electrochemical phenomena at the electrolyte/specimen interface? To what extent the emerging electrochemical response of the material can explain the degradation in its mechanical properties? Can the degradation in mechanical properties of the material as a function of the imposed strain rate be related to the extent of localized

corrosion? To this end, AA7075 that is susceptible to localized corrosion is concentrated on. Specimens of AA7075 are subjected to a range of SSR tensile loading in a very low pH corrosive environment where the native passive layer of the alloy is thermodynamically unstable [136, 137]. The degradation in mechanical properties of the material are measured and a detailed failure analysis of the fractured specimens are carried out. The electrochemical behavior of the material is characterized using a 3-electrode setup for Electrochemical Impedance Spectroscopy (EIS). The EIS measurements provide a detailed view of all the interfacial phenomena occurring at the electrolyte/specimen interface.

6.2. Material and method

The material examined in this work is an aluminum alloy 7075-T651. Bare plates of the alloy of dimensions $72 \times 2.4 \times 1.0$ *inches* (with largest dimension parallel to the rolling direction) conforming to AMS-QQ-A250/12 was acquired from California Metal & Supply Inc., Santa Fe Springs, CA. The standard uniaxial tensile test specimens [138] of gauge length 1*inch* (25.4*mm*) and diameter 0.25*inch* (6.35*mm*) with gauge length oriented parallel to the rolling direction were then machined from these plates.

The synergistic effects of mechanical loading and corrosive environment on the fracture response is investigated through slow strain rate test coupled with electrochemical impedance spectroscopy, as described in **2.5**.

Metallographic studies were performed on both the as received material and specimens tested under electrochemical-mechanical loading conditions using optical and SEM following **2.4**.

6.3. Results

6.3.1. Initial Microstructure and Mechanical Response in Air

The EBSD maps of the undeformed AA7075 specimen along the axis and the cross section of the tensile specimen are shown in Figs. 6.1(a) and (b), respectively. The associated inverse pole figure is shown in Fig. 6.1(c). Fig. 6.1(a) represents an area of $112 \times 112 \mu m^2$ and Fig. 6.1(b) represents an area of $100 \times 100 \mu m^2$. The electron beam was scanned in steps of $1 \mu m$ and the EBSD pattern was indexed using aluminum face-centered-cubic (fcc) phase. The EBSD maps in Figs. 6.1 (a) and (b) reveal that the undeformed microstructure of the material contains elongated pancake shaped grains aligned along the axis of the tensile specimen. The EBSD maps also highlight the presence of several low angle grain boundaries within the grains. The unindexed spots along the grain boundaries in the EBSD map, Figs. 6.1(a) and (b), likely correspond to grain boundary precipitates, typical of aluminum alloy 7075-T651 [139].

The tensile nominal stress-strain response of the material in air at imposed nominal strain rates of $10^{-3} s^{-1}$ and $10^{-5} s^{-1}$ are shown in Fig. 6.1(d). As seen in the figure, two orders of magnitude change in the imposed nominal strain rate in air does not significantly affect the stress-strain response of the material. On average the material yields at a yield strength (σ_y) of 511.4*MPa,* which is followed by mild strain hardening until a total strain (ε_u) of ~10.6%. The average ultimate tensile strength (σ_u) of the material is 572.1*MPa* and the material undergoes fracture at a total strain (ε_f) of ~14.2%.

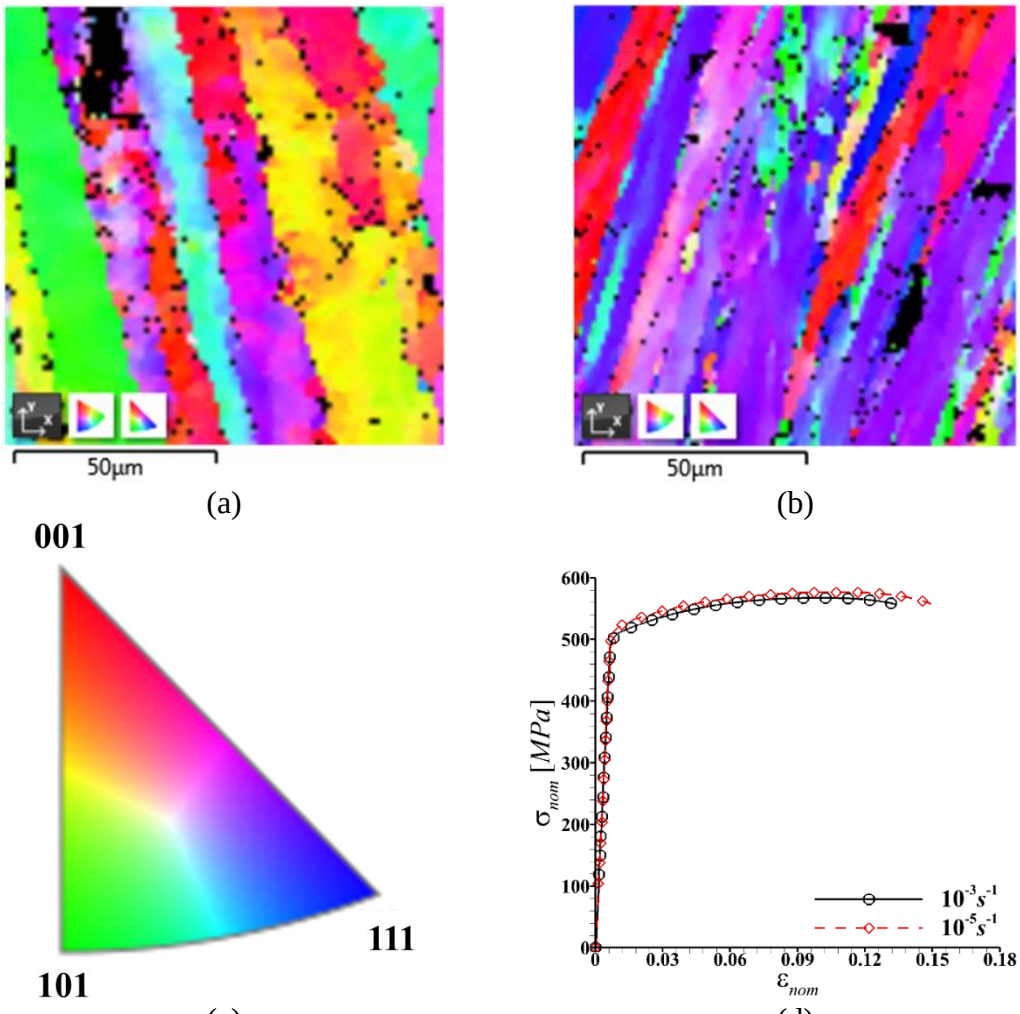

Figure 6.1. EBSD map of the microstructure of undeformed AA7075 along (a) the axis and (b) the cross-section of the tensile specimen. The inverse pole figure associated with (a) and (b) is shown in (c). (d) The nominal stress-strain curves of the AA7075 specimens tested in air under uniaxial tension at imposed nominal strain rates of $10^{-3}s^{-1}$ and $10^{-5}s^{-1}$.

6.3.2. Mechanical Response in Corrosive Environment

The tensile nominal stress-strain response of the materials tested in the corrosive environment of EXCO solution at five imposed strain rates are shown in Fig. 6.2 (a). All the tensile specimens were first immersed in the EXCO solution for roughly 30mins prior to the application of the tensile strain. Note that no extensometer was used for the slow

strain rate tests in the corrosive environment. This is why the elastic slope of the stress-strain curves shown in Fig. 6.2 (a) is less than the elastic slope of the stress-strain curves in Fig. 6.1 (d). As shown in Fig. 6.2 (a), unlike the tests conducted in air, the mechanical response of the material in the corrosive environment strongly depends on the imposed strain rate. Since the mechanical response of the material itself is not very sensitive to the imposed strain rate, the strong imposed strain rate dependence in Fig. 6.2 (a) is likely due to the exposure to highly corrosive EXCO solution. For the same imposed nominal strain rate of $10^{-5}s^{-1}$ the mechanical properties measured in air such as σ_y decreased by ~6%, σ_u decreased by ~14%, ε_u decreased by ~66% and ε_f decreased by ~65% when tested in the corrosive environment.

The variations of the apparent σ_y and σ_u of the material exposed to corrosive environment with the inverse of the imposed strain rate, $\dot{\varepsilon}^{-1}$, are shown in Fig. 6.2 (b). The parameter $\dot{\varepsilon}^{-1}$ represents the time scale of the exposure of the specimens to the corrosive environment. For each imposed strain rate three tests were carried out except for the slowest strain rate of $0.5\times10^{-6}s^{-1}$. The symbols in Fig. 6.2(b) correspond to experimentally measured data whereas the lines are power law fit to the variation of mean values with $\dot{\varepsilon}^{-1}$ For σ_y versus $\dot{\varepsilon}^{-1}$ data, $\sigma_y = 483 \times (\dot{\varepsilon}^{-1} \times 10^{-5})^{-0.06}$, whereas for σ_u versus $\dot{\varepsilon}^{-1}$ data, $\sigma_u = 493 \times (\dot{\varepsilon}^{-1} \times 10^{-5})^{-0.065}$. The σ_y and σ_u of the specimens exposed to the corrosive environment initially decrease rapidly with increasing $\dot{\varepsilon}^{-1}$ and then tend to saturate. In addition, the degrading effect of the exposure to the corrosive

environment as marked by the effect of $\dot{\varepsilon}^{-1}$ on σ_u of the material is initially greater than the degrading effect on σ_y, so that for large $\dot{\varepsilon}^{-1}$ or small $\dot{\varepsilon}$ $\left(\dot{\varepsilon} \leq 10^{-6}\,\mathrm{s}^{-1}\right)$, $\sigma_u \approx \sigma_y$. This shows that in the corrosive environment below a threshold imposed strain rate the specimen breaks without appreciable (macroscopic) plastic deformation.

The dependence of ε_u (strain at σ_u) and ε_f of the material exposed to corrosive environment on the inverse of the imposed strain rate, $\dot{\varepsilon}^{-1}$ are shown in Fig. 6.2 (c). The symbols in the figure correspond to experimental data whereas the solid lines are power law fit. For ε_u versus $\dot{\varepsilon}^{-1}$ data, $\varepsilon_u = 0.037 \times (\dot{\varepsilon}^{-1} \times 10^{-5})^{-0.25}$, whereas for ε_f versus $\dot{\varepsilon}^{-1}$ data, $\varepsilon_f = 0.05 \times (\dot{\varepsilon}^{-1} \times 10^{-5})^{-0.3}$ Similar to the strength parameters, ε_u and ε_f of the specimens exposed to the corrosive environment initially decrease rapidly with increasing $\dot{\varepsilon}^{-1}$ and then tend to saturate. Also the degrading effect of the exposure to the corrosive environment as marked by the effect of $\dot{\varepsilon}^{-1}$ on ε_f of the material is initially greater than the degrading effect on ε_u, so that for large $\dot{\varepsilon}^{-1}$ or small $\dot{\varepsilon}$, $\varepsilon_f \to \varepsilon_u$. This suggests that the overall damage tolerance of the material in the corrosive environment decreases with decreasing imposed strain rate, and for slow enough strain rate the material is essentially brittle.

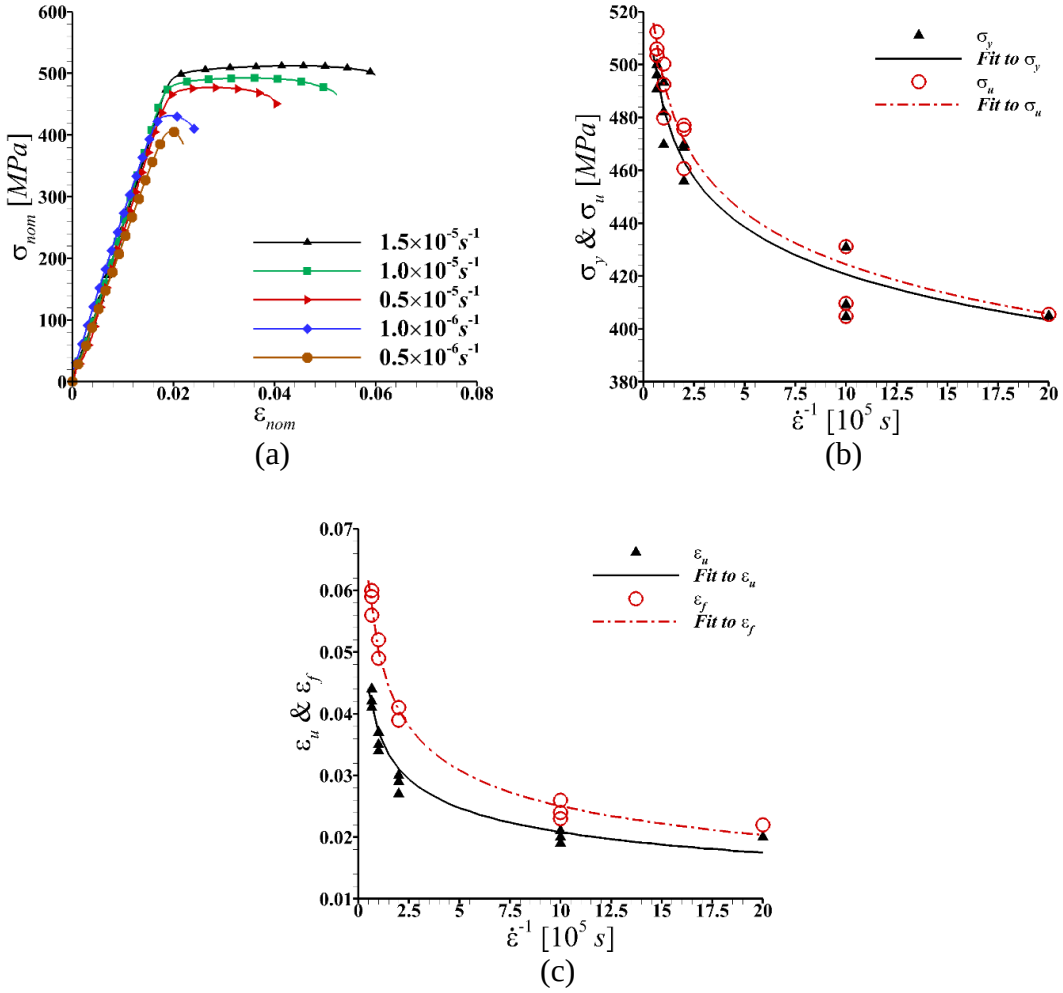

Figure 6.2. (a) The nominal stress-strain curves of the AA7075 specimens tested in EXCO solution under uniaxial tension at five imposed strain rates. The variation of mechanical properties, (b) yield strength (σ_y) and ultimate tensile strength (σ_u), and (c) total strain at σ_u (ε_u) and total strain at fracture (ε_f), as a function of the inverse of the imposed strain rate ($\dot{\varepsilon}^{-1}$).

6.3.3. Failure Analysis

All the specimens tested in air underwent slant fracture due to localized shear dominated deformation with fracture plane inclined at an angle of ~45° with respect to the initial cross-section. All the specimens tested in air also exhibited a slight amount of

necking before final fracture. The optical microscope image of the side view of a fractured cylindrical tensile specimen tested in air at an imposed nominal strain rate of $10^{-5}s^{-1}$ is shown in Fig. 6.3(a). This mode of fracture under uniaxial tension is typical of aluminum alloy 7075 [140]. However, for the specimens tested in the corrosive environment, the inclination of the overall fracture plane with respect to the cross-section was found to be less than 45°. For the same imposed nominal strain rate of $10^{-5}s^{-1}$, the inclination of the overall fracture plane with respect to the cross-section is ~32.5° for the specimen tested in the corrosive environment as shown in Fig. 6.3(b). The angle between the overall fracture plane and the cross-section was found to decrease with decreasing imposed strain rate for the specimens tested in the corrosive environment. As shown in Fig. 6.3(c) the angle between the fracture plane and the cross-section is ~28.8° for the specimen tested in the corrosive environment at an imposed nominal strain rate of $10^{-6}s^{-1}$.

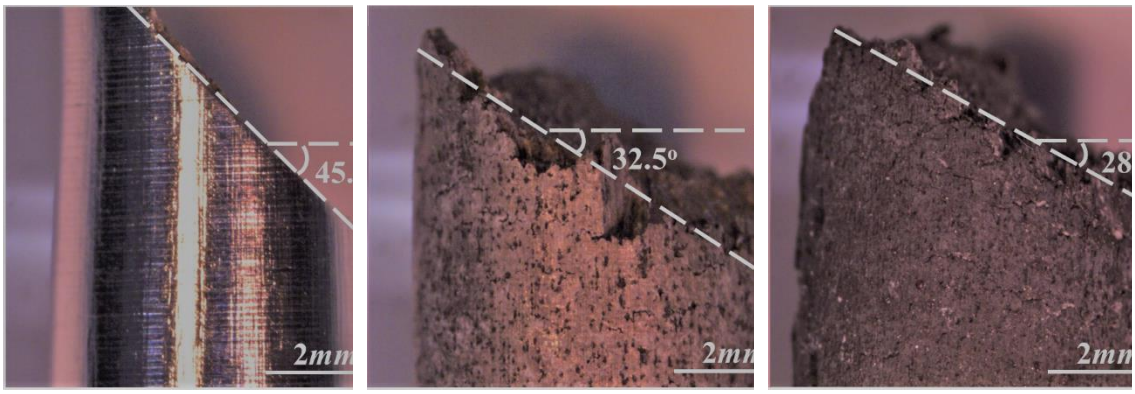

(a) (b) (c)

Figure 6.3. Optical microscope images of the side view of the specimens fractured under uniaxial tension: (a) in air at an imposed nominal strain rate of 10^{-5} s^{-1}, and in the EXCO solution at imposed nominal strain rates of (b) 10^{-5} s^{-1} and (c) 10^{-6} s^{-1}.

Next, the fracture surfaces of the specimens fractured under uniaxial tension in air and in corrosive environment is analyzed. The center of the fracture surface of the

specimens tested in air exhibit elongated shallow dimples characteristic of fracture process dominated by localized shear, Fig. 6.4(a). The center of the fracture surface to a greater extent exhibit similar features for all the specimens regardless of the imposed strain rate or the environment, Figs. 6.4(b) and (c). The center of the fracture surface of the specimens tested in corrosive environment, however, are slightly rougher than the fracture surface of the specimens tested in air, suggesting fast shear dominated fracture. For the specimens tested in air the fracture surface exhibit similar features throughout the fracture plane, Figs. 6.4(a) and (d). But for the specimens tested in the corrosive environment, the fracture surface in the center differ significantly from that near the edge of the specimen. The fracture surface near the edge of the specimens tested in corrosive environment exhibit facets arranged as curved stairway in an annular region, Figs. 6.4(e) and (f). The breadth of the annular region consisting of the faceted fracture surface increases with decreasing imposed strain rate. For the specimen tested in corrosive environment at a nominal strain rate of $10^{-5}s^{-1}$ the breadth of the faceted annular region is ~$750\mu m$ whereas at a nominal strain rate of $10^{-6}s^{-1}$ it is ~$1025\mu m$.

To understand the origin of the faceted fracture surfaces near the edge of the specimens exposed to corrosive environment, the longitudinal section of the fractured specimens is analyzed. The SEM images of the mechanically polished longitudinal sections of specimens fractured at imposed nominal strain rates of $10^{-5}s^{-1}$ and $10^{-6}s^{-1}$, while exposed to corrosive environment are shown in Figs. 6.5(a) and (d), respectively. The magnified view of the regions below the fracture surfaces marked as R1 and R2 in Fig. 6.5(a), and R1 and R2 in Fig. 6.5(d), are shown in Figs. 6.5(b) and (c), and in Figs.

6.5(e) and (f), respectively. The characteristics of intergranular corrosion cracking in these specimens can be clearly seen in Figs. 6.5(b), (c), (e) and (f). As also seen in these figures the intergranular corrosion cracks traverse in both the transverse (normal to the loading direction) and the longitudinal (parallel to the loading direction) directions. The extent to which intergranular cracks traverse in the longitudinal direction seems to be increasing with decreasing imposed strain rate. However, irrespective of the imposed strain rate, the extent to which intergranular cracks traverse in the longitudinal direction seems to decrease with increasing transverse crack growth.

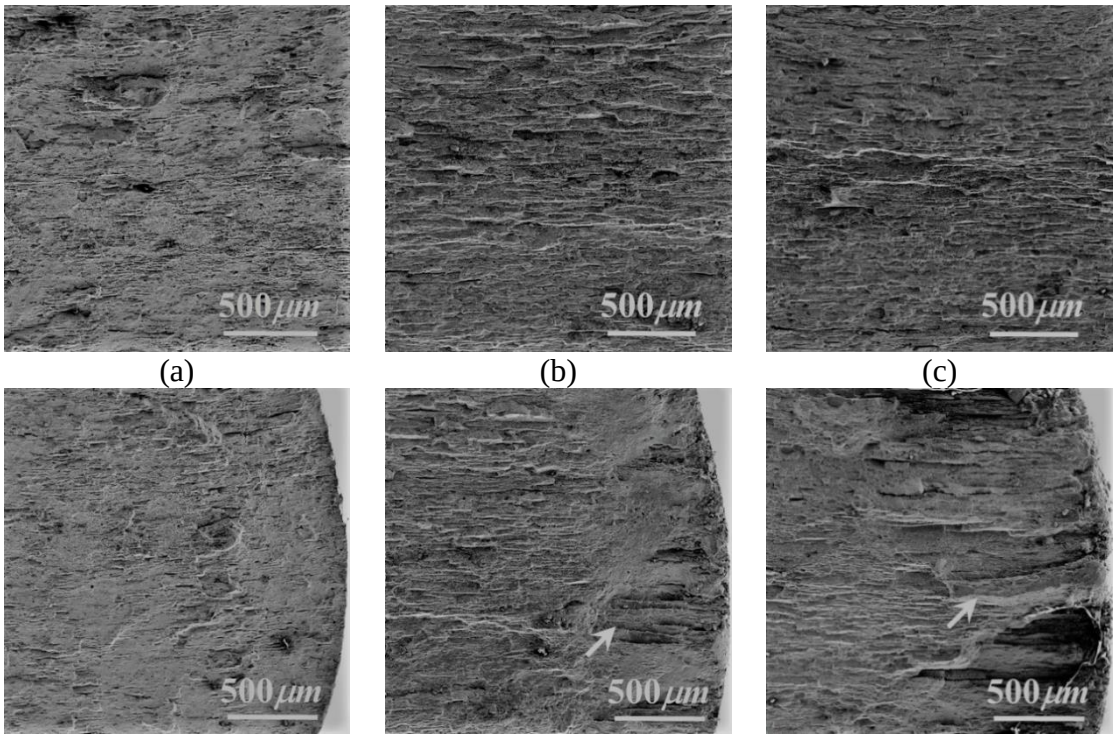

Figure 6.4. SEM images of the fracture surface of the specimens fractured under uniaxial tension. The fracture surface of the specimen tested under different conditions: (a, d) in air at an imposed nominal strain rate of $10^{-5}s^{-1}$, (b, e) in the EXCO solution at an imposed nominal strain rate of $10^{-5}s^{-1}$, (c, f) in the EXCO solution at an imposed nominal strain rate of $10^{-6}s^{-1}$. The SEM images (a)-(c) are taken from the center of the fracture surface whereas (d)-(f) are taken from the edge of the fracture surface.

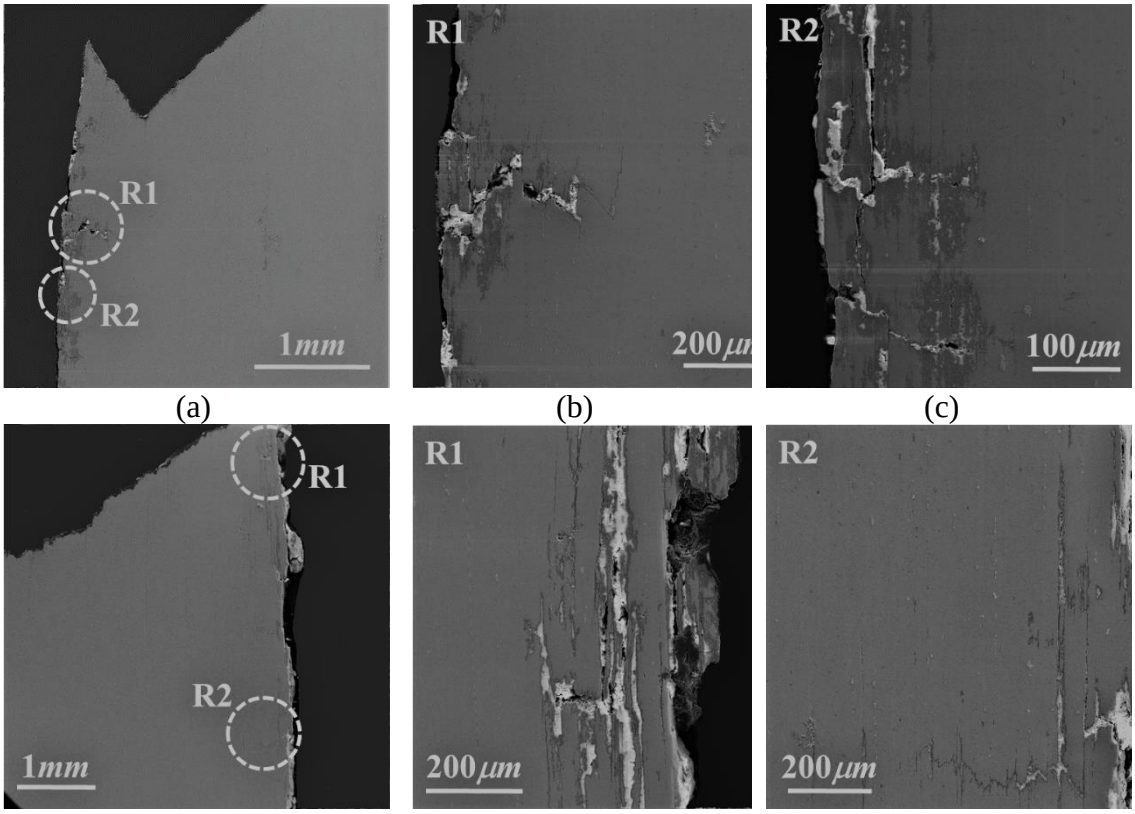

Figure 6.5. SEM images of the mechanically polished longitudinal section of the specimens fractured under uniaxial tension while immersed in the EXCO solution. (a) The specimen tested at an imposed nominal strain rate of $10^{-5}s^{-1}$. Magnified view of the regions R1 and R2 marked with dashed circles in (a) are shown in (b) and (c). (d) The specimen tested at an imposed nominal strain rate of $10^{-6}s^{-1}$. Magnified view of the regions R1 and R2 marked with dashed circles in (d) are shown in (e) and (f).

6.3.4. Electrochemical Impedance Spectroscopy

The emerging electrochemical characteristics of all the specimens exposed to corrosive environment (EXCO solution) and SSR tensile loading were characterized by electrochemical impedance spectroscopy (EIS). The steps involved with EIS measurement are as follows. First, the specimen was exposed to the corrosive environment. Second, after ~5min of exposure of the specimen to the corrosive environment, a 5min open-

circuit-potential (OCP) test was carried out that was followed by the first set (initial) of EIS measurements. Next, after a total of ~0.5*h* of exposure of the specimen to the corrosive environment, the slow strain rate (SSR) tensile loading was imposed on the specimen. This was then followed by a series of 2min OCP tests plus EIS measurements until the specimen fractured. Additionally, for the purpose of comparison the emerging electrochemical characteristics of few specimens that were only exposed to corrosive environment and no mechanical loading, for extended amount of time, were also characterized by EIS. For this, first a 5min open-circuit-potential (OCP) test was carried out after ~5min of exposure of the specimen to the corrosive environment. Following the OCP test, first EIS measurement was carried out, which was then followed by a series of 2min OCP tests plus EIS measurements. All the EIS were corrected for Ohmic resistance due to the electrolyte following Orazem et al. [141].

The Nyquist and the phase angle plots for a specimen exposed only to corrosive environment without any mechanical loading are shown in Figs. 6.6(a) and (b), respectively. The equivalent circuit (EC) shown in Fig. 6.6(c) is used to analyze the EIS measurements. In the EC, Re is the resistance of the electrolyte, Rct is the adsorption resistance due to charge transfer process at the substrate (specimen) – electrolyte interface, $Qc(j\omega)^{\alpha}$ is the constant phase element (CPE) due to double layer capacitance at the substrate – electrolyte interface, $Qi(j\omega)^{\alpha}$ is the CPE due to adsorption process (inductance) of intermediate species [142], and Rb is the faradaic resistance due to hydrogen evolution [143]. The magnitude of the CPE, $Qc(j\omega)^{\alpha}$, includes both the capacitance and the roughness of the interface [144].

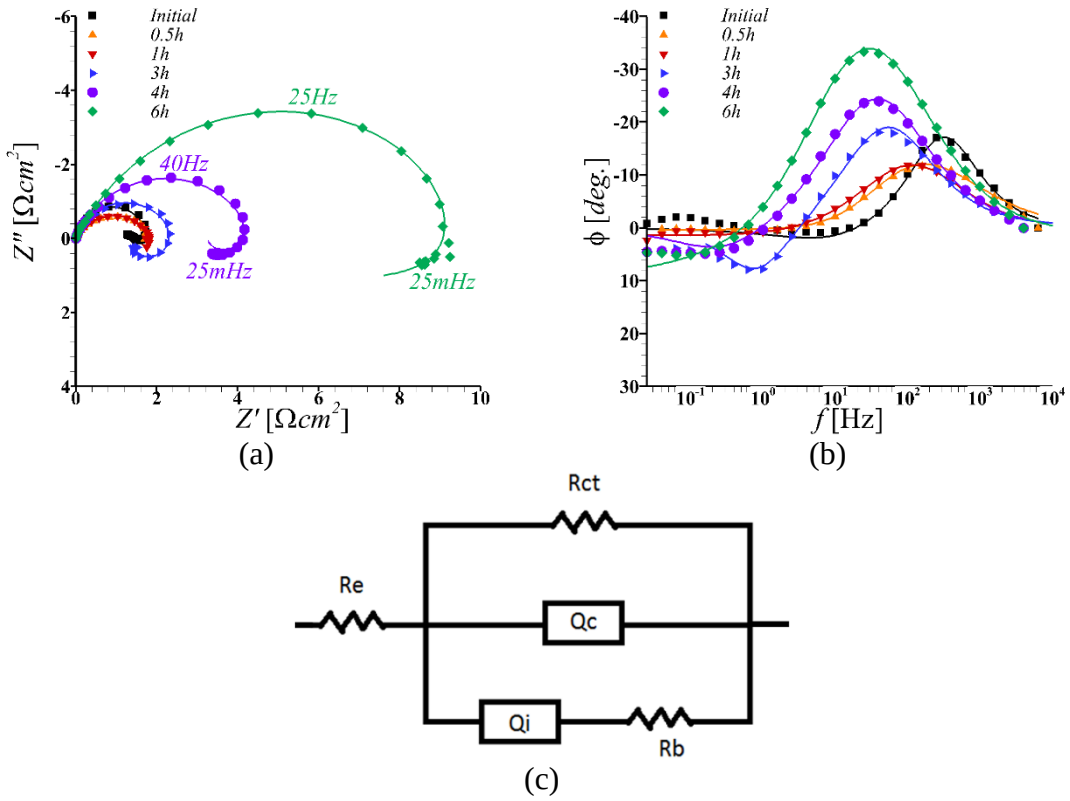

Figure 6.6. (a) The Nyquist and (b) the phase angle plots for the specimen subjected to no mechanical loading while immersed in the EXCO solution. (c) The equivalent circuit used to analyze the EIS measurements. The solid lines in (a) and (b) are the fitted curves using the equivalent circuit shown in (c).

The semicircle shape of the curve (at mid frequencies) in Fig. 6.6(a) shows an activation or charge transfer process. The increase in the diameter of the semicircle shape of the curve with increasing time shows that prolonged exposure of the specimen to the corrosive environment results in modifications to the specimen surface that influences the charge transfer magnitude, Rct. This is also apparent from Fig. 6.6(b), where the phase angle maxima at similar frequencies follows the same trend. By considering the EC shown in Fig. 6.6(c), the charge transfer magnitude (Rct) for the initial measurement (~10min after exposure) is found to be ~1.74Ωcm^2 and it roughly stays constant for the first 3 hours

of exposure to the corrosive environment. But with continued exposure, Rct tends to increase and is found to be ~$9.8\Omega cm^2$ after 6 hours of exposure. The increase in Rct indicates a decrease in the corrosion rate of the specimen. A visual inspection of the specimen surface indeed revealed the formation of a porous corrosion film. Note that the initial pH of the corrosive environment considered here, i.e. the EXCO solution, is roughly 0.4 and, in such an acidic environment, formation of oxide or hydroxide on the surface of aluminum alloys is not feasible as per the classical E-pH diagram. Thus, the evolution of the pH of the solution was monitored and it was found that the pH does increase slowly with time and reaches a maximum value of ~3 in 20 hours. But a pH of ~3 is still very acidic, and the curves shown in Fig. 6.6(a) correspond to measurement times where the solution is extremely acidic. Notably, the formation of an Al_xO_y porous film under highly acidic conditions has been reported previously [145].

The magnitude of Qc as estimated by fitting the EC shown in Fig. 6.6(c), initially increases rapidly with time from ~ $4.3\times10^{-4}\ Fs^{(\alpha-1)}cm^{-2}$ with $\alpha\approx1$ for the initial measurement to ~$3.7\times10^{-3}\ Fs^{(\alpha-1)}cm^{-2}$ with $\alpha\approx0.8$ for the measurement after 1 hour of exposure. Thereafter the value of Qc increases rather slowly and was found to be ~ $4.8\times10^{-3}\ Fs^{(\alpha-1)}cm^{-2}$ with $\alpha\approx0.8$ for the measurement taken after 6 hours of exposure. Based upon the definition of a capacitor, the increase in Qc indicates a decrease in the thickness (or compactness) of the growing porous corrosion film [142]. In Fig. 6.6(a), at low frequencies the curve is a small inverted semicircle. Also, in Fig. 6.6(b) at low frequencies the phase angle is positive corresponding to the presence of inductive

response. These slow rate processes represent hydrogen adsorption and reduction reaction at the substrate under acidic conditions [143].

The Nyquist and the phase angle plots for the specimen subjected to SSR tensile loading with a nominal uniaxial tensile strain rate of $10^{-5}s^{-1}$ while exposed to corrosive environment are shown in Fig. 6.7. The initial EIS measurement (~10min after exposure) in Fig. 6.7 correspond to no load condition. At this stage the EIS measurement, Fig. 6.7(a), shows an activation or charge transfer process (semicircle shape of the curve corresponding to mid frequencies) with an adsorption characteristic signal (inverted semicircle corresponding to low frequencies), similar to EIS measurements shown in Fig. 6.6(a) for the specimen exposed to corrosive environment without mechanical loading. But unlike the no load condition in Fig. 6.6(a), following the application of the tensile loading the diameter of the semicircle shape of the curve (at mid frequencies) decreases with increasing time showing a decrease in the charge transfer magnitude, Rct, with increasing time. The decrease in Rct marks the increase in the surface activity (or corrosion rate) of the specimen. This is also apparent from Fig. 6.7(b), where the phase angle maxima follows the same trend. In Fig. 6.7(a), the inverted semicircle at low frequencies that represents cathodic reaction vanishes following the application of the tensile loading. This is also seen in Fig. 6.7(b), where at low frequencies the phase angle magnitude is positive for the no load condition but becomes negative following the application of the tensile loading. Note that the specimens subjected to SSR tensile loading with a nominal uniaxial strain rate of $10^{-5}s^{-1}$ while exposed to corrosive environment fractured shortly after 1 hour from the onset of mechanical loading.

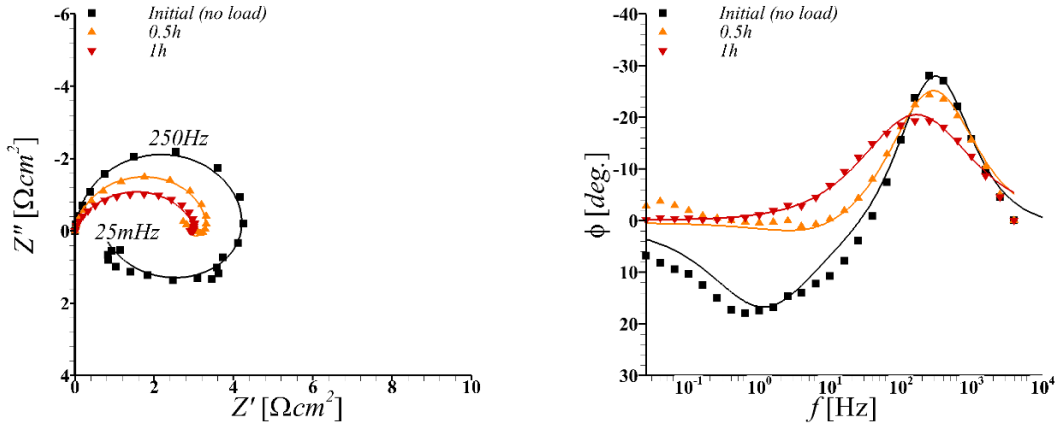

Figure 6.7. (a) The Nyquist and (b) the phase angle plots for the specimen subjected to a nominal uniaxial tensile strain rate of $10^{-5}s^{-1}$ while immersed in the EXCO solution. The mechanical loading on the specimen was imposed after ~0.5*h* of immersion of the specimen in the EXCO solution. The solid lines in (a) and (b) are the fitted curves using the equivalent circuit shown in Fig. 6(c).

Figure 6.8 shows the Nyquist and the phase angle plots for the specimen subjected to SSR tensile loading with a nominal uniaxial tensile strain rate of $10^{-6}s^{-1}$ while exposed to corrosive environment. The initial EIS measurement (~10min after exposure) in Fig. 6.8 correspond to no load condition. At this stage the EIS measurement shows an activation or charge transfer process with an adsorption characteristic signal, similar to the corresponding (Initial) EIS measurements shown in Figs. 6.6 and 6.7. Following the application of the tensile strain rate of $10^{-6}s^{-1}$, the EIS measurements (corresponding to 0.5*h* and 1*h*) first show a decrease in the charge transfer magnitude, Rct, with increasing time (marked by a decrease in the diameter of the semicircle in Fig. 6.8(a), also apparent from Fig. 6.8(b), where the phase angle maxima follows the same trend). This is similar to the EIS measurements shown in Fig. 6.7 for the imposed nominal strain rate of $10^{-5}\ s^{-1}$. The EIS measurements taken after more than 1*h* of exposure to the corrosive

environments shown in Fig. 6.8 are similar to those shown in Fig. 6.6 for the no load conditions. However, the charge transfer magnitude, Rct, for the specimen subjected to the nominal strain rate of $10^{-6}s^{-1}$ is less than the Rct for the specimen subjected to no load, Fig. 6.6. For example, for the specimen subjected to the tensile strain rate of $10^{-6}s^{-1}$ the Rct is ~$8.4\Omega cm^2$ whereas for the specimen subjected to no mechanical loading Rct is ~$9.8\Omega cm^2$ for the measurements after $6h$ of exposure. The value of Qc for the specimen subjected to the tensile strain rate of $10^{-6}s^{-1}$ is found to be $\sim 5.0\times10^{-3}\ Fs^{(\alpha-1)}cm^{-2}$ with $\alpha \approx 0.8$ for the measurement taken after 6 hours of exposure which is slightly greater than the value of Qc corresponding to no mechanical loading conditions shown in Fig. 6.6. For both, the specimen subjected to the nominal strain rate of $10^{-6}s^{-1}$, Fig. 6.8, and the specimen subjected to no mechanical loading, Fig. 6.6, the adsorption characteristics is consistently captured in the phase angle plot.

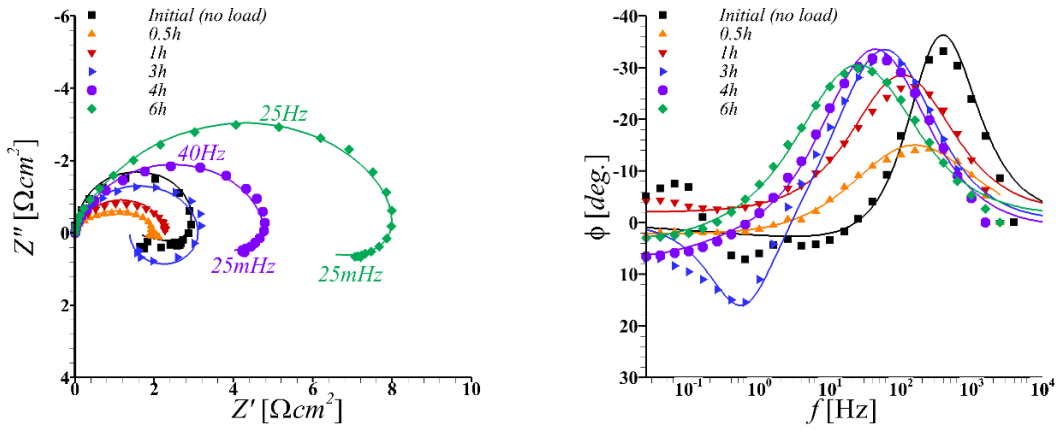

(a) **(b)**

Figure 6.8. (a) The Nyquist and (b) the phase angle plots for the specimen subjected to a nominal uniaxial tensile strain rate of $10^{-6}s^{-1}$ while immersed in the EXCO solution. The mechanical loading on the specimen was imposed after ~0.5*h* of immersion of the specimen in the EXCO solution. The solid lines in (a) and (b) are the fitted curves using the equivalent circuit shown in Fig. 6(c).

6.4. Discussion

The synergistic effects of exposure to highly corrosive environment and imposed SSR tensile loading on the overall mechanical and electrochemical response of a high strength aluminum alloy 7075-T651 have been analyzed. The mechanical properties of the material such as yield strength $\left(\sigma_y\right)$, ultimate tensile strength $\left(\sigma_u\right)$, total strain at σ_u $\left(\varepsilon_u\right)$ and total strain at fracture $\left(\varepsilon_f\right)$, in the corrosive environment all decrease with decreasing imposed strain rate. However, the degrading effect of the exposure to corrosive environment with decreasing imposed strain rate is more pronounced on ultimate tensile strength and strain to fracture, such that for slow enough imposed strain rate, $\sigma_u \approx \sigma_y$ and $\varepsilon_f \to \varepsilon_u$. This shows that in the corrosive environment the extent of (macroscopic) plastic deformation and (overall) damage tolerance of the material decreases with decreasing strain rate and for slow enough strain rate the material is essentially brittle.

The EIS measurements coupled with post-mortem characterization of the failed specimens provide an unprecedented view of the evolution of the specimen surface and the interfacial reactions affecting mechanical response of the material. The EIS measurements show an activation of charge transfer process soon after the specimen is exposed to the corrosive environment. The subsequent EIS measurements (during the early hours of the exposure of the specimen to the corrosive environment) reveal a transient state during which, in the absence of imposed tensile strain, the charge transfer magnitude either stays constant or increases slightly, denoting no appreciable change in the surface activity (or corrosion rate). However, in the presence of imposed tensile strain

the charge transfer magnitude decreases, marking an increase in the surface activity. All the mechanical properties, σ_y, σ_u, ε_u and ε_f, of the material were in fact found to decrease rapidly with increasing $\dot{\varepsilon}^{-1}$ (inverse of the imposed strain rate) for relatively large imposed strain rates for which the specimens fractured within this transient state. Note that the inverse of the imposed strain rate represents the time scale of the exposure of the specimens to the corrosive environment.

The EIS measurements taken after prolonged exposure of the specimen to the corrosive environment show significant increase in the charge transfer magnitude (corresponding to decreases in the corrosion rate). The adsorption characteristics are also captured in these EIS measurements. The increase in the charge transfer magnitude is associated with the formation of a porous black anodic oxide film. However, for the EIS measurements at similar times, the charge transfer magnitude for the specimens subjected to tensile straining is less than that for the specimens subjected to no tensile straining. This shows that the application of tensile loading results in the breakdown of the film, resulting in an increase in the area available for the dissolution reaction. But the continuous increase in the charge transfer magnitude with increasing time even in the presence of tensile loading suggests that the newly exposed area due to the breakdown of the film is soon covered with the film following the dissolution reaction. In line with this observation the degradation in all the mechanical properties of the material were found to tend towards saturation for relatively small, imposed strain rates or large $\dot{\varepsilon}^{-1}$. Also, for these strain rates the specimens fractured without appreciable (macroscopic) plastic deformation.

The overall failure mechanism that emerges is such that the exposure of the specimen to the corrosive environment results in both uniform and localized (inter granular) corrosion of the specimen. The imposed tensile strain on the specimen results in breakdown of the passivating film formed due to corrosion. The breakdown of the film preferentially occurs along the grain boundaries. Thereafter, within the substrate (specimen), corrosion proceeds preferentially along the grain boundaries in both the longitudinal and the transverse directions with respect to the tensile axis. The continued tensile straining of the specimen results in preferential cracking of the corroded transverse grain boundaries thus biasing the corrosion pathway in the transverse direction. The interplay of preferential corrosion and the tensile straining eventually results in the formation of a circumferential crack of critical crack length and final fracture of the specimen.

The proposed mechanism can also be justified by a qualitative fracture mechanics analysis. The fracture toughness $\left(K_{IC}\right)$ of the material is given as, $K_{IC} = Y\sigma_c\sqrt{a}$, where, Y is a constant related to the sample's geometry, σ_c is the critical stress at fracture and a is the crack length [146]. For simplicity it can be assumed that the fracture toughness of the intact material (interior of the specimen) remains unchanged so that $\sigma_c\sqrt{a} = K_{IC}/Y$ is a constant for a fixed sample geometry. The assumption that the fracture toughness of the intact material remains constant is a strong assumption but is based on the fact that the EIS measurements revealed rather weak adsorption characteristics. Following this the ratio of the ultimate tensile strength of the material for two imposed strain rates,

$(\sigma_u)_{\dot{\varepsilon}_1}/(\sigma_u)_{\dot{\varepsilon}_2}$, should be equal to the inverse of the square root of the ratio of the breadth of the faceted annular region, $\sqrt{(a)_{\dot{\varepsilon}_2}/(a)_{\dot{\varepsilon}_1}}$, observed on the fracture surfaces of the specimens for the two imposed strain rates. For two imposed strain rates, $\dot{\varepsilon}_1 = 10^{-5} s^{-1}$ and $\dot{\varepsilon}_2 = 10^{-6} s^{-1}$, on average $\sigma_u \approx 493 MPa$ and $424 MPa$, respectively, and the breadth of the faceted annular region is $\approx 750 \mu m$ and $1025 \mu m$, respectively. These parameters result in, $(\sigma_u)_{\dot{\varepsilon}_1}/(\sigma_u)_{\dot{\varepsilon}_2}$=1.16, and $\sqrt{(a)_{\dot{\varepsilon}_2}/(a)_{\dot{\varepsilon}_1}}$=1.17, in agreement with the expected fracture scaling. This approximate analysis also holds for all other imposed tensile strain rates.

6.5. Conclusions

The objective of this work was to characterize the synergistic effects of corrosion and imposed tensile strain rate on the overall mechanical and electrochemical response of the material. To this end, tensile specimens of aluminum alloy 7075 with grains aligned parallel to the tensile axis were subjected to a range of slow strain rate tensile loading while immersed in the EXCO solution. The degradation in the mechanical response of the material was measured and the emerging electrochemical characteristics of the electrolyte/specimen interface using electrochemical impedance spectroscopy (EIS) were characterized for a range of imposed strain rates. The EIS measurements coupled with the post-mortem microscopic characterization of the specimens rationalized the effects of corrosion and the imposed strain rate on the degradation in the mechanical response of the material. The principal conclusions of this work are:

1. The mechanical properties of the material exposed to the corrosive environment initially decrease rapidly with increasing inverse of the imposed tensile strain rate and then tend to saturate.

2. In the corrosive environment the extent of plastic deformation and damage tolerance of the material decreases with decreasing imposed strain rate and for slow enough strain rates the macroscopic mechanical response of the material is essentially brittle.

3. The intergranular corrosion cracks in the material traverse along both the longitudinal and the transverse directions with respect to the loading axis. The extent of the longitudinal crack growth is found to increase with decreasing imposed strain rate. But for a fixed imposed strain rate, the extent of the longitudinal crack growth decreases with increasing transverse crack growth.

4. The EIS measurements revealed a transient state during the initial exposure of the specimen to the corrosive environment. During this transient state the charge transfer magnitude roughly stays constant for no load conditions indicating no change in corrosion rate, whereas the charge transfer magnitude decreases in the presence of imposed tensile strain indicating increase in surface activity (or corrosion rate).

5. The EIS measurements taken after prolonged exposure of the specimen to the corrosive environment show significant increase in the charge transfer magnitude or decrease in surface activity. However, for the EIS measurements at similar times, the charge transfer magnitude (corrosion rate) for the specimens subjected to tensile straining is less (greater) than that for the specimens subjected to no load.

6. A qualitative fracture mechanics-based analysis suggests that the interplay of intergranular corrosion cracks and the tensile straining facilitates the nucleation of a circumferential crack of critical crack length resulting in final fracture of the specimen.

7. SUMMARY AND FUTURE WORK

7.1 Summary

In this dissertation an attempt has been made to understand the interactions of various spatiotemporal length-scales that dictate the final fracture of some of the most technologically sought after advanced high strength structural materials using state-of-the-art *in-situ* experiments and microstructure-based simulations. The results show that the characterization of the mechanical response of dual-phase materials and even some single-phase materials with hierarchical microstructure is fundamentally different in an imposed deformation field that is homogeneous versus in an imposed deformation field that is heterogeneous at the structural (specimen) length-scale. In the former, the characterization of the mechanical response can simply be based on an unstructured continuum description of the mechanical properties. However, the latter can lead to breakdown in structural-microstructural length-scale separation, which makes it extremely challenging to treat a dual-phase or hierarchical single-phase material microstructure as an effective homogenized material. This is in contrast with any classical analysis that only focuses on the structure-fracture correlation and not on the structure-microstructure-fracture correlation. Mechanistic analysis of complex hierarchical microstructures in an imposed heterogeneous deformation fields at the structural length-scale, such as those observed near a structural discontinuity or crack, therefore, must involve explicit consideration of the length-scales associated with the material microstructure.

Furthermore, the results pertaining to the effects of evolving microstructure due to deformation-induced twinning on the fracture response of a material show that the

heterogeneous deformation field induced by the presence of a structural discontinuity can produce substantial microstructural modifications that can provide both a pathway for crack growth as well as a mechanism for crack growth arrest. Finally, the results of the experiments focused on understanding the synergistic effects of mechanical loading and corrosive environment on tensile response of an aluminum alloy show that under these circumstances it is the interplay of the localized corrosion cracks and the tensile straining that facilitates nucleation of cracks with critical crack length resulting in pre-mature fracture.

The results presented in this dissertation will, hopefully, guide the development of new materials to meet the ever-growing industrial need of lightweight yet durable structures, and will pave the way to microstructure-informed mechanistic theories and models for structural design and analysis.

7.2 Future work

Considering the results presented in this dissertation, several research questions might be instigated in the future.

In this work, the focus was confined to elucidating the effect of the interlacing of the structural and the microstructural length-scales on the mechanical response of advanced high strength steels under quasi-static loading conditions. The interlacing of these two length-scales will likely also be affected by other loading conditions, such as dynamic and cyclic loading conditions. Hopefully, this work will instigate further research in this direction.

Next, in this work the focus was confined to a material that undergoes microstructure evolution due to deformation-induced twinning. In future, one should also investigate the interaction of a growing crack and the microstructural evolution due to deformation-induced phase transformation. Note that the temporal evolutions of the microstructure due to deformation-induced phase transformations not only involve introduction of new interphase boundaries, but also residual stresses, volume, and crystal structure changes. The effect of deformation-induced phase transformation on the fracture response of a material is, therefore, worth studying using the *in-situ* mechanical testing approach established in this dissertation.

In the future, the influence of mechanical loading on the local electrochemical response of the material can be analyzed using *in-situ* mechanical tests coupled with local electrochemical measurements. For the localized corrosion experiment, corrosive environment can be applied on a small area on the surface of the tensile specimen with a capillary tip [147]. It is expected that this will allow quantifying the correlation of imposed tensile stress, corrosive environment, and local material microstructure.

REFERENCES

[1] Chen P, Ghassemi-Armaki H, Kumar S, Bower A, Bhat S, Sadagopan S. Microscale-calibrated modeling of the deformation response of dual-phase steels. Acta Materialia 2014;65:133-49.

[2] Srivastava A, Bower AF, Hector LG, Carsley JE, Zhang L, Abu-Farha F. A multiscale approach to modeling formability of dual-phase steels. Modelling and Simulation in Materials Science and Engineering 2016;24:025011.

[3] Gerbig D, Srivastava A, Osovski S, Hector LG, Bower A. Analysis and design of dual-phase steel microstructure for enhanced ductile fracture resistance. International Journal of Fracture 2018;209:3-26.

[4] Wang J, Singh J, Ramisetti N. Process Influences on Press-Hardened Steel Microstructure and Impact Performance. Iron and Steel Technology 2016;13:124-32.

[5] Białobrzeska B, Konat Ł, Jasiński R. The influence of austenite grain size on the mechanical properties of low-alloy steel with boron. Metals 2017;7:26.

[6] Ghassemi-Armaki H, Chen P, Bhat S, Sadagopan S, Kumar S, Bower A. Microscale-calibrated modeling of the deformation response of low-carbon martensite. Acta Materialia 2013;61:3640-52.

[7] Hanamura T, Torizuka S, Tamura S, Enokida S, Takechi H. Effect of Austenite Grain Size on Transformation Behavior, Microstructure and Mechanical Properties of 0.1C–5Mn Martensitic Steel. ISIJ International 2013;53:2218-25.

[8] Karaman I, Sehitoglu H, Chumlyakov YI, Maier HJ, Kireeva IV. The effect of twinning and slip on the bauschinger effect of hadfield steel single crystals. Metallurgical and Materials Transactions A 2001;32:695-706.

[9] Karaman I, Sehitoglu H, Gall K, Chumlyakov YI, Maier HJ. Deformation of single crystal Hadfield steel by twinning and slip. Acta Materialia 2000;48:1345-59.

[10] Efstathiou C, Sehitoglu H. Strain hardening and heterogeneous deformation during twinning in Hadfield steel. Acta Materialia 2010;58:1479-88.

[11] Ji Z, Jing Z. 7075-T6 aluminium alloy exfoliation corrosion sensitivity and electrochemical impedance spectroscopy under stress. Materials Research Innovations 2015;19:S10-230-S10-4.

[12] Blaber J, Adair B, Antoniou A. Ncorr: open-source 2D digital image correlation matlab software. Experimental Mechanics 2015;55:1105-22.

[13] Pan B, Li K, Tong W. Fast, robust and accurate digital image correlation calculation without redundant computations. Experimental Mechanics 2013;53:1277-89.

[14] Standard Test Method for Exfoliation Corrosion Susceptibility in 2XXX and 7XXX Series Aluminum Alloys (EXCO Test). West Conshohocken, PA: ASTM G34 - 01; 2013.
[15] E8/E8M-16a Standard Test Methods for Tension Testing of Metallic Materials. West Conshohocken, PA: ASTM International; 2016.

[16] Bridgman P. The stress distribution at the neck of a tension specimen. Transactions of the ASM 1944;32:553-74.

[17] Rashid M. Dual phase steels. Annual Review of Materials Science 1981;11:245-66.
[18] Kuziak R, Kawalla R, Waengler S. Advanced high strength steels for automotive industry. Archives of civil and mechanical engineering 2008;8:103-17.

[19] Joost WJ. Reducing vehicle weight and improving US energy efficiency using integrated computational materials engineering. Jom 2012;64:1032-8.

[20] Davies R. Influence of martensite composition and content on the properties of dual phase steels. Metallurgical Transactions A 1978;9:671-9.

[21] Ramos LF, Matlock DK, Krauss G. On the deformation behavior of dual-phase steels. Metallurgical Transactions A 1979;10:259-61.

[22] Steinbrunner DL, Matlock DK, Krauss G. Void formation during tensile testing of dual phase steels. Metallurgical Transactions A 1988;19:579-89.

[23] Kang J, Ososkov Y, Embury JD, Wilkinson DS. Digital image correlation studies for microscopic strain distribution and damage in dual phase steels. Scripta Materialia 2007;56:999-1002.

[24] Ososkov Y, Wilkinson DS, Jain M, Simpson T. In-situ measurement of local strain partitioning in a commercial dual-phase steel. International Journal of Materials Research 2007;98:664-73.

[25] Avramovic-Cingara G, Ososkov Y, Jain M, Wilkinson D. Effect of martensite distribution on damage behaviour in DP600 dual phase steels. Materials Science and Engineering: A 2009;516:7-16.

[26] Avramovic-Cingara G, Saleh CA, Jain M, Wilkinson D. Void nucleation and growth in dual-phase steel 600 during uniaxial tensile testing. Metallurgical and materials transactions A 2009;40:3117.

[27] Choi KS, Liu WN, Sun X, Khaleel MA. Influence of martensite mechanical properties on failure mode and ductility of dual-phase steels. Metallurgical and Materials Transactions A 2009;40:796-809.

[28] Sun X, Choi KS, Liu WN, Khaleel MA. Predicting failure modes and ductility of dual phase steels using plastic strain localization. International Journal of Plasticity 2009;25:1888-909.

[29] Sun X, Choi KS, Soulami A, Liu WN, Khaleel MA. On key factors influencing ductile fractures of dual phase (DP) steels. Materials Science and Engineering: A 2009;526:140-9.

[30] Ghadbeigi H, Pinna C, Celotto S, Yates J. Local plastic strain evolution in a high strength dual-phase steel. Materials Science and Engineering: A 2010;527:5026-32.

[31] Kadkhodapour J, Butz A, Ziaei-Rad S, Schmauder S. A micro mechanical study on failure initiation of dual phase steels under tension using single crystal plasticity model. International Journal of Plasticity 2011;27:1103-25.

[32] Sodjit S, Uthaisangsuk V. Microstructure based prediction of strain hardening behavior of dual phase steels. Materials & Design 2012;41:370-9.

[33] Choi S-H, Kim E-Y, Woo W, Han S, Kwak J. The effect of crystallographic orientation on the micromechanical deformation and failure behaviors of DP980 steel during uniaxial tension. International Journal of Plasticity 2013;45:85-102.

[34] Jamwal RS, Gokhale AM, Bhat SP. Quantitative Fractographic Analysis of Variability in the Tensile Ductility of a High Strength Dual-Phase Steel. Metallography, Microstructure, and Analysis 2013;2:30-4.

[35] Han Q, Kang Y, Hodgson PD, Stanford N. Quantitative measurement of strain partitioning and slip systems in a dual-phase steel. Scripta Materialia 2013;69:13-6.

[36] Marteau J, Haddadi H, Bouvier S. Investigation of strain heterogeneities between grains in ferritic and ferritic-martensitic steels. Experimental Mechanics 2013;53:427-39.

[37] Roth CC, Mohr D. Effect of strain rate on ductile fracture initiation in advanced high strength steel sheets: Experiments and modeling. International Journal of Plasticity 2014;56:19-44.

[38] Tasan CC, Hoefnagels JPM, Diehl M, Yan D, Roters F, Raabe D. Strain localization and damage in dual phase steels investigated by coupled in-situ deformation experiments and crystal plasticity simulations. International Journal of Plasticity 2014;63:198-210.

[39] Ghassemi-Armaki H, Maaß R, Bhat SP, Sriram S, Greer JR, Kumar KS. Deformation response of ferrite and martensite in a dual-phase steel. Acta Materialia 2014;62:197-211.

[40] Alaie A, Kadkhodapour J, Ziaei Rad S, Asadi Asadabad M, Schmauder S. Formation and coalescence of strain localized regions in ferrite phase of DP600 steels under uniaxial tensile deformation. Materials Science and Engineering: A 2015;623:133-44.

[41] Marcadet SJ, Mohr D. Effect of compression–tension loading reversal on the strain to fracture of dual phase steel sheets. International Journal of Plasticity 2015;72:21-43.

[42] Yan D, Tasan CC, Raabe D. High resolution in situ mapping of microstrain and microstructure evolution reveals damage resistance criteria in dual phase steels. Acta Materialia 2015;96:399-409.

[43] Tasan CC, Diehl M, Yan D, Bechtold M, Roters F, Schemmann L, et al. An Overview of Dual-Phase Steels: Advances in Microstructure-Oriented Processing and Micromechanically Guided Design. Annual Review of Materials Research 2015;45:391-431.

[44] Matsuno T, Teodosiu C, Maeda D, Uenishi A. Mesoscale simulation of the early evolution of ductile fracture in dual-phase steels. International Journal of Plasticity 2015;74:17-34.

[45] Lai Q, Bouaziz O, Gouné M, Brassart L, Verdier M, Parry G, et al. Damage and fracture of dual-phase steels: Influence of martensite volume fraction. Materials Science and Engineering: A 2015;646:322-31.

[46] Zhou J, Gokhale AM, Gurumurthy A, Bhat SP. Realistic microstructural RVE-based simulations of stress–strain behavior of a dual-phase steel having high martensite volume fraction. Materials Science and Engineering: A 2015;630:107-15.

[47] Lai Q, Brassart L, Bouaziz O, Gouné M, Verdier M, Parry G, et al. Influence of martensite volume fraction and hardness on the plastic behavior of dual-phase steels: Experiments and micromechanical modeling. International Journal of Plasticity 2016;80:187-203.

[48] Huang S, He C, Zhao Y. Microstructure-based RVE approach for stretch-bending of dual-phase steels. Journal of Materials Engineering and Performance 2016;25:966-76.

[49] Aşık EE, Perdahcıoğlu ES, van den Boogaard AH. Microscopic investigation of damage mechanisms and anisotropic evolution of damage in DP600. Materials Science and Engineering: A 2019;739:348-56.

[50] Liu Y, Fan D, Bhat SP, Srivastava A. Ductile fracture of dual-phase steel sheets under bending. International Journal of Plasticity 2019.

[51] Chuang R, WenJiao D, WeiGang Z. Effects of ferrite grain characteristics on strain distribution of dual-phase steel. Materials Research Express 2019;6:016539.

[52] Abaqus user's manual version 6.10. Providence, RI2010.

[53] Davies G. Materials for automobile bodies: Butterworth-Heinemann; 2012.

[54] Bouaziz O, Zurob H, Huang M. Driving force and logic of development of advanced high strength steels for automotive applications. Steel research international 2013;84:937-47.

[55] SATO M, UTSUMI Y, WATANABE K. Ultra-High-Strength, Quench-type, Hot-Rolled Steel Sheets of 1,620 MPa Grade for Automobile Door Impact Beams. Kobelco Technology Review 2008;28:5.

[56] Bok H-H, Lee M-G, Pavlina EJ, Barlat F, Kim H-D. Comparative study of the prediction of microstructure and mechanical properties for a hot-stamped B-pillar reinforcing part. International journal of mechanical sciences 2011;53:744-52.

[57] Altan T, Tekkaya AE. Sheet Metal Forming - Processes and Applications. 1 ed. Materials Park, Ohio, USA: ASM International; 2012.

[58] Morito S, Tanaka H, Konishi R, Furuhara T, Maki T. The morphology and crystallography of lath martensite in Fe-C alloys. Acta Materialia 2003;51:1789-99.

[59] Morito S, Huang X, Furuhara T, Maki T, Hansen N. The morphology and crystallography of lath martensite in alloy steels. Acta Materialia 2006;54:5323-31.

[60] Kitahara H, Ueji R, Tsuji N, Minamino Y. Crystallographic features of lath martensite in low-carbon steel. Acta Materialia 2006;54:1279-88.

[61] Hata K, Fujiwara K, Wakita M, Kawano K. Development of a Reconstruction Method of Prior Austenite Microstructure Using EBSD Data of Martensite. Nippon Steel & Sumitomo Metal Corporation: Tokyo, Japan 2017.

[62] Krauss G, Matlock D. Effects of strain hardening and fine structure on strength and toughness of tempered martensite in carbon steels. Le Journal de Physique IV 1995;5:C8-51-C8-60.

[63] Krauss G. Martensite in steel: strength and structure. Materials Science and Engineering: A 1999;273-275:40-57.

[64] Krauss G. Deformation and fracture in martensitic carbon steels tempered at low temperatures. Metallurgical and Materials Transactions A 2001;32:861-77.

[65] Tkalcec I, Mari D, Benoit W. Correlation between internal friction background and the concentration of carbon in solid solution in a martensitic steel. Materials Science and Engineering: A 2006;442:471-5.

[66] Morito S, Yoshida H, Maki T, Huang X. Effect of block size on the strength of lath martensite in low carbon steels. Materials Science and Engineering: A 2006;438-440:237-40.

[67] Zhang C, Wang Q, Ren J, Li R, Wang M, Zhang F, et al. Effect of martensitic morphology on mechanical properties of an as-quenched and tempered 25CrMo48V steel. Materials Science and Engineering: A 2012;534:339-46.

[68] Prawoto Y, Jasmawati N, Sumeru K. Effect of Prior Austenite Grain Size on the Morphology and Mechanical Properties of Martensite in Medium Carbon Steel. Journal of Materials Science & Technology 2012;28:461-6.

[69] Kaijalainen AJ, Suikkanen PP, Limnell TJ, Karjalainen LP, Kömi JI, Porter DA. Effect of austenite grain structure on the strength and toughness of direct-quenched martensite. Journal of Alloys and Compounds 2013;577:S642-S8.

[70] Li X, Ma X, Subramanian SV, Shang C, Misra RDK. Influence of prior austenite grain size on martensite–austenite constituent and toughness in the heat affected zone of 700MPa high strength linepipe steel. Materials Science and Engineering: A 2014;616:141-7.

[71] Golem L, Cho L, Speer JG, Findley KO. Influence of austenitizing parameters on microstructure and mechanical properties of Al-Si coated press hardened steel. Materials & Design 2019:107707.

[72] Bachmann F, Hielscher R, Schaeben H. Grain detection from 2d and 3d EBSD data—Specification of the MTEX algorithm. Ultramicroscopy 2011;111:1720-33.

[73] Hielscher R, Silbermann CB, Schmidl E, Ihlemann J. Denoising of crystal orientation maps. Journal of Applied Crystallography 2019;52:984-96.

[74] Yardley V, Fahimi S, Payton E. Classification of creep crack and cavitation sites in tempered martensite ferritic steel microstructures using MTEX toolbox for EBSD. Materials Science and Technology 2015;31:547-53.

[75] Nyyssönen T, Isakov M, Peura P, Kuokkala V-T. Iterative determination of the orientation relationship between austenite and martensite from a large amount of grain pair misorientations. Metallurgical and Materials Transactions A 2016;47:2587-90.

[76] E112-13 Standard Test Methods for Determining Average Grain Size. West Conshohocken, PA: ASTM International; 2013.

[77] Van Minnebruggen K, Verstraete M, Hertelé S, De Waele W. Evaluation and Comparison of Double Clip Gauge Method and Delta 5 Method for CTOD Measurement in SE (T) Specimens. Journal of Testing and Evaluation 2015;44:2414-23.

[78] Zhu X-K. Advances in Fracture Toughness Test Methods for Ductile Materials in Low-Constraint Conditions. Procedia Engineering 2015;130:784-802.

[79] Huang Y, Zhou W. J-CTOD relationship for clamped SE(T) specimens based on three-dimensional finite element analyses. Engineering Fracture Mechanics 2014;131:643-55.

[80] ABAQUS User's Mannual. Dassault Systemes; 2018.

[81] Zheng X, Ghassemi-Armaki H, Srivastava A. Structural and microstructural influence on deformation and fracture of dual-phase steels. Materials Science and Engineering: A 2020;774:138924.

[82] Liu Y, Fan D, Bhat SP, Srivastava A. Ductile fracture of dual-phase steel sheets under bending. International Journal of Plasticity 2020;125:80-96.

[83] Liu Y, Fan D, Arróyave R, Srivastava A. Microstructure-Based Modeling of the Effect of Inclusion on the Bendability of Advanced High Strength Dual-Phase Steels. Metals 2021;11:431.

[84] Subramanyam DK, Swansiger AE, Avery HS, Committee AH. Austenitic Manganese Steels. Properties and Selection: Irons, Steels, and High-Performance Alloys: ASM International; 1990. p. 0.

[85] Havel D. Austenitic Manganese Steel: A Complete Overview. Technical Report. Columbia Steel Casting Co., Inc; 2017.

[86] Havlíček P, Bušová K. Experience with explosive hardening of railway frogs from Hadfield steel. METAL 2012-Conference Proceedings, 21st International Conference on Metallurgy and Materials: TANGER Ltd.; 2012.

[87] Okechukwu C, Dahunsi OA, Oke PK, Oladele IO, Dauda M. Development of hardfaced crusher jaws using ferro-alloy hardfacing inserts and low carbon steel substrate. J Tribol 2018;18:20-39.

[88] Raghavan K, Sastri A, Marcinkowski M. Nature of the Work-hardening Behavior in Hadfields Manganese steel. Trans Met Soc AIME 1969;245:1569-75.

[89] Owen W, Grujicic M. Strain aging of austenitic Hadfield manganese steel. Acta materialia 1998;47:111-26.

[90] Dastur Y, Leslie W. Mechanism of work hardening in Hadfield manganese steel. Metallurgical transactions A 1981;12:749-59.

[91] Adler P, Olson G, Owen W. Strain hardening of Hadfield manganese steel. Metallurgical and Materials Transactions A 1986;17:1725-37.

[92] Shtremel M. On the work hardening mechanism of Hadfield steel. Phys Met Metallogr(USSR) 1987;63:158-66.

[93] Hutchinson B, Ridley N. On dislocation accumulation and work hardening in Hadfield steel. Scripta Materialia 2006;55:299-302.

[94] Abbasi M, Kheirandish S, Kharrazi Y, Hejazi J. The fracture and plastic deformation of aluminum alloyed Hadfield steels. Materials Science and Engineering: A 2009;513:72-6.

[95] Bayraktar E, Khalid FA, Levaillant C. Deformation and fracture behaviour of high manganese austenitic steel. Journal of Materials Processing Technology 2004;147:145-54.

[96] Karaman I, Sehitoglu H, Beaudoin A, Chumlyakov YI, Maier H, Tome C. Modeling the deformation behavior of Hadfield steel single and polycrystals due to twinning and slip. Acta Materialia 2000;48:2031-47.

[97] Karaman I, Sehitoglu H, Chumlyakov YI, Maier H, Kireeva I. Extrinsic stacking faults and twinning in Hadfield manganese steel single crystals. Scripta Materialia 2001;44:337-43.

[98] Karaman I, Sehitoglu H, Gall K, Chumlyakov YI. On The Deformation Mechanisms in Single Crystal Hadfield Manganese Steels. Scripta Materialia 1998;38:1009-15.

[99] Canadinc D, Sehitoglu H, Maier H, Niklasch D, Chumlyakov Y. Orientation evolution in Hadfield steel single crystals under combined slip and twinning. International Journal of Solids and Structures 2007;44:34-50.

[100] Canadinc D, Sehitoglu H, Karaman I, Chumlyakov Y, Maier H. The role of nitrogen on the deformation response of hadfield steel single crystals. Metallurgical and Materials Transactions A 2003;34:1821-31.

[101] Canadinc D, Sehitoglu H, Maier H, Chumlyakov Y. Strain hardening behavior of aluminum alloyed Hadfield steel single crystals. Acta Materialia 2005;53:1831-42.

[102] Müllner P, Solenthaler C, Uggowitzer P, Speidel M. Brittle fracture in austenitic steel. Acta metallurgica et materialia 1994;42:2211-7.

[103] Koyama M, Akiyama E, Tsuzaki K. Hydrogen embrittlement in a Fe–Mn–C ternary twinning-induced plasticity steel. Corrosion Science 2012;54:1-4.

[104] Chumlyakov YI, Kireeva I, Sehitoglu H, Litvinova E, Zaharova E, Luzginova N. High-strength single crystals of austenitic stainless steels with nitrogen content: mechanisms of deformation and fracture. Materials science forum: Trans Tech Publ; 1999. p. 395-400.

[105] Koyama M, Sawaguchi T, Tsuzaki K. Quasi-cleavage fracture along annealing twin boundaries in a Fe–Mn–C austenitic steel. ISIJ international 2012;52:161-3.

[106] Michel D, Nahm H, Moteff J. deformation induced twin boundary crack formation in type 304 stainless steel. Materials Science and Engineering 1973;11:97-102.

[107] Wang W, Liu T, Cao X, Lu Y, Shoji T. In-situ observation on twin boundary evolution and crack initiation behavior during tensile test on 316L austenitic stainless steel. Materials Characterization 2017;132:169-74.

[108] Remy L. The interaction between slip and twinning systems and the influence of twinning on the mechanical behavior of fcc metals and alloys. Metallurgical Transactions A 1981;12:387-408.

[109] Guo X, Ouyang Q, Weng G, Zhu L. The direct and indirect effects of nanotwin volume fraction on the strength and ductility of coarse-grained metals. Materials Science and Engineering: A 2016;657:234-43.

[110] American Society for M, Committee ASMIH. ASM Handbook. Volume 12, Fractography. Metals Park, Ohio: American Society for Metals.; 1987.

[111] Bramfitt B, Marder A. A study of the delamination behavior of a very low-carbon steel. Metallurgical transactions A 1977;8:1263-73.

[112] Picak S, Liu J, Hayrettin C, Nasim W, Canadinc D, Xie K, et al. Anomalous work hardening behavior of Fe40Mn40Cr10Co10 high entropy alloy single crystals deformed by twinning and slip. Acta Materialia 2019;181:555-69.

[113] Kaushik V, Narasimhan R, Mishra R. Experimental study of fracture behavior of magnesium single crystals. Materials Science and Engineering: A 2014;590:174-85.

[114] Kaushik V, Narasimhan R, Mishra RK. Finite element simulations of notch tip fields in magnesium single crystals. International Journal of Fracture 2014;189:195-216.

[115] Bland LG, Locke JSW. Chemical and electrochemical conditions within stress corrosion and corrosion fatigue cracks. npj Materials Degradation 2017;1:12.

[116] Donahue JR, Lass AB, Burns JT. The interaction of corrosion fatigue and stress-corrosion cracking in a precipitation-hardened martensitic stainless steel. npj Materials Degradation 2017;1:11.

[117] Findlay S, Harrison N. Why aircraft fail. Materials today 2002;5:18-25.

[118] Davis JR. Corrosion of aluminum and aluminum alloys: Asm International; 1999.

[119] Ricker RE, Lee E, Taylor R, Lei C, Pregger B, Lipnickas E. Chloride ion activity and susceptibility of Al alloys 7075-T6 and 5083-H131 to stress corrosion cracking. Metallurgical and Materials Transactions A 2013;44:1353-64.

[120] Buchheit R. A compilation of corrosion potentials reported for intermetallic phases in aluminum alloys. Journal of the Electrochemical Society 1995;142:3994-6.

[121] Birbilis N, Buchheit R. Electrochemical characteristics of intermetallic phases in aluminum alloys an experimental survey and discussion. Journal of The Electrochemical Society 2005;152:B140-B51.

[122] Birbilis N, Cavanaugh M, Buchheit R. Electrochemical behavior and localized corrosion associated with Al7Cu2Fe particles in aluminum alloy 7075-T651. Corrosion Science 2006;48:4202-15.

[123] Cao FH, Zhang Z, Li JF, Cheng YL, Zhang JQ, Cao CN. Exfoliation corrosion of aluminum alloy AA7075 examined by electrochemical impedance spectroscopy. Materials and Corrosion 2004;55:18-23.

[124] Goldman M, Ünlü N, Shiflet G, Scully J. Selected corrosion properties of a novel amorphous Al-Co-Ce alloy system. Electrochemical and solid-state letters 2005;8:B1-B5.
[125] Jones RH. Stress-corrosion cracking: ASM international; 1992.

[126] Yue TM, Yan LJ, Dong CF, Chan CP. Stress corrosion cracking behaviour of laser treated aluminium alloy 7075 using a slow strain rate test. Materials Science and Technology 2005;21:961-6.

[127] Su J, Zhang Z, Shi Y, Yang Z, Zhang J, Cao C. The effect of applied tensile stress on the exfoliation corrosion of 7075-T6 alloy. Materials and Corrosion 2006;57:729-33.

[128] Askari-Paykani M, Meratian M, Shayan M, Raeissi K. Effects of heat treatment parameters on microstructural changes and corrosion behavior of Al 7075 Alclad alloy. Anti-Corrosion Methods and Materials 2012;59:231-8.

[129] Silva G, Rivolta B, Gerosa R, Derudi U. Study of the SCC Behavior of 7075 Aluminum Alloy After One-Step Aging at 163 °C. Journal of Materials Engineering and Performance 2013;22:210-4.

[130] Sunada S, Nunomura N. Electrochemical Impedance Characteristics of Sintered 7075 Aluminum Alloy under SSRT Test. Proceedings of the 8th Pacific Rim International Congress on Advanced Materials and Processing: Springer; 2013. p. 261-8.

[131] Parkins R. Development of strain-rate testing and its implications. Stress Corrosion Cracking—The Slow Strain-Rate Technique: ASTM International; 1979.

[132] Ugiansky G, Johnson C, Thompson D, Gillespie E. Slow strain-rate stress corrosion testing of aluminum alloys. Stress Corrosion Cracking—The Slow Strain-Rate Technique: ASTM International; 1979.

[133] Knight S, Birbilis N, Muddle B, Trueman A, Lynch S. Correlations between intergranular stress corrosion cracking, grain-boundary microchemistry, and grain-boundary electrochemistry for Al–Zn–Mg–Cu alloys. Corrosion Science 2010;52:4073-80.

[134] Kim C, Wilde B. A review of the constant strain-rate stress corrosion cracking test. Stress Corrosion Cracking—The Slow Strain-Rate Technique: ASTM International; 1979.

[135] Diegle R, Boyd W. The role of film rupture during slow strain-rate stress corrosion cracking testing. Stress Corrosion Cracking—The Slow Strain-Rate Technique: ASTM International; 1979.

[136] Pourbaix M. Atlas of Electrochemical Equilibria in Aqueous Solutions. Houston, TX: National Association of Corrosion Engineers; 1974.

[137] Macdonald DD. Reflections on the history of electrochemical impedance spectroscopy. Electrochimica Acta 2006;51:1376-88.

[138] Standard Test Methods for Tension Testing of Metallic Materials. West Conshohocken, PA: ASTM E8/E8M; 2016.

[139] Rometsch PA, Zhang Y, Knight S. Heat treatment of 7xxx series aluminium alloys—Some recent developments. Transactions of Nonferrous Metals Society of China 2014;24:2003-17.

[140] Chung N, Embury J, Evensen J, Hoagland R, Sargent C. Unstable shear failure in a 7075 aluminum alloy. Acta Metallurgica 1977;25:377-81.

[141] Orazem ME, Pébère N, Tribollet B. Enhanced graphical representation of electrochemical impedance data. Journal of The Electrochemical Society 2006;153:B129-B36.

[142] Yang D, Rosas O, Castaneda H. FeCO3 layer evolution for API 5L X52 steel in carbon dioxide-saturated NaCl brine in the presence of 1-decyl-3-methylimidazolium chloride. Corrosion Science 2014;87:40-50.

[143] Yoo HD, Jang JH, Ka BH, Rhee CK, Oh SM. Impedance analysis for hydrogen adsorption pseudocapacitance and electrochemically active surface area of Pt electrode. Langmuir 2009;25:11947-54.

[144] Hirschorn B, Orazem ME, Tribollet B, Vivier V, Frateur I, Musiani M. Determination of effective capacitance and film thickness from constant-phase-element parameters. Electrochimica Acta 2010;55:6218-27.

[145] Genel K. Environmental effect on the fatigue performance of bare and oxide coated 7075-T6 alloy. Engineering Failure Analysis 2013;32:248-60.

[146] Anderson TL. Fracture Mechanics: Fundamentals and Applications. Fourth ed. Boca Raton, FL: CRC press; 2017.

[147] Cubides Y, Karayan AI, Zhao D, Nash L, Xie K, Castaneda H. New insights on the corrosion mechanism of a peak-aged Mg–9Al–1Zn alloy in a chloride environment. Journal of Alloys and Compounds 2020;840:155786.